2005

# Numerical simulation of coastal mesoscale flows in Monterey Bay and Eritrea

Bereket Lebassi Habtezion
*San Jose State University*

# NUMERICAL SIMULATION OF COASTAL MESOSCALE FLOWS IN MONTEREY BAY AND ERITREA

A Thesis Presented to

The Faculty of the Department of Meteorology

San Jose State University

In Partial Fulfillment

Of the Requirements for the Degree

Master of Science

by

Bereket Lebassi Habtezion

December 2005

APPROVED FOR THE DEPARTMENT OF METEOROLOGY

Alison F. C. Bridger

Prof. Alison F. Bridger

Robert Van Buskirk

Dr. Robert Van Buskirk

Tom Rickenbach

Prof. Tom Rickenbach

APPROVED FOR THE UNIVERSITY

Rhea J. Williamson

## ABSTRACT

NUMERICAL SIMULATION OF COASTAL MESOSCALE FLOWS IN MONTEREY BAY AND ERITREA

by Bereket Lebassi Habtezion

This research has two parts: simulations of the Monterey Bay sea breeze, and simulations of the mesoscale flow along the Eritrean southern coast for wind resource assessment. The first study is motivated by doppler lidar observations near Monterey Bay, California during a two-week summer period that failed to show an expected return flow aloft. Simulations of the Monterey Bay sea breeze with the Regional Atmospheric Modeling System (RAMS) were conducted to analyze the characteristics of simulated return flows.

For the Eritrea part of the research, the pressing need for clean and environmentally-sustainable energy has motivated a wind resource assessment of the southern coast of Eritrea using mesoscale modeling techniques. In this thesis, simulation of the wind resources of the Eritrean southern coast was undertaken, with an emphasis on the Aseb area. Simulations of the Eritrean southern coast with the RAMS were conducted to analyze the characteristics of the region's wind resources.

**Acknowledgements**

A journey is easier when you travel together. Interdependence is certainly more valuable than independence. This thesis is the result of three and half years of work whereby I have been accompanied and supported by many people. It is a pleasant aspect for which I have now the opportunity to express my gratitude.

The first person I would like to thank is my direct adviser Dr. Robert Van Buskirk. I have been involved in meteorological projects since 1995 when I started as student research assistant at the University of Asmara, and continued till 2001, at the Department of Energy, ERTC, Asmara, Eritrea. His overt enthusiasm and comprehensive view of research and his mission for providing "only high-quality work and not less," has made a deep impression on me. I owe him much gratitude for having shown me this way of research. He could not even realize how much I have learned from him. Besides of being an excellent adviser, Dr. Robert was as close as a relative and a good friend to me. I am really glad that I have come to get know Dr. Robert Van Buskirk in my life.

I also would like to thank the Chairperson of my thesis committee, Prof. Alison F. Bridger, for supporting half of the work financially. She was a perfect professor for most of my dynamics classes and she was the

one who kept an eye on the progress of my work and always was available when I needed her advice. Many thanks go to her for chairing the committee and for reviewing the drafts and final version of this thesis. I would also like to thank the other members of my MS committee who monitored my work and took effort in reading and providing me with valuable comments on earlier versions of this thesis: Prof. Scot Rafkin, Prof. Robert D. Bornstein, and Prof. Rickenbach. I thank you all.

My Eritrean colleagues of the Eritrean Technical Exchange project all gave me the feeling of being at home at work. Mengsteab Habtegiorgis, Tesfamichael Berhane, Tefom Ghebregergis, and Yonas Samuel, many thanks for being my colleague. Especially, Tesfamichael Berhane who gave me his honest advices and for has been a good friend and brother during the past years of his stay at San Jose State University. The Department of Energy group, Tesfai Ghebreselasie (Minister of Energy and Mines), Samuel Baire (Director Department of Energy), and especially the ERTC staff, the late Minat Berhane (former Director ERTC) and his successor Debesai Ghebrehiwot, the late Haile Teclai (an engineer), Rico Tsegai, Sium Tesfay (physicists), and Dr. Semere Habtetsion (Director of Energy Planning). Thank you all for

inspiring me to do research at the ERTC and giving me the chance to come to the United States to pursue my higher education.

I am also grateful for the Meteorology Computer Section for providing me an excellent work environment during the past years and Mike Voss for his cheerful assistance. I am also grateful for Fred Snively, Graduate student from the Department of Meteorology for continually asking about the progress of my research.

This research has been supported and funded by Professor Alison F. Bridger of San Jose State University and Dr. Robert Van Buskirk of Lawrence Berkeley National Laboratory and the Eritrea Technical Exchange Project of the International Collaborative for Science Education and the Environment (ETEP/ICSEE). Prof. Bridger contributed for the Monterey Bay part of the research and Erirean Technical Exchange Project contributed to the Eritrea part of the research.

I feel a deep sense of gratitude for my father, Lebassi, and my mother, Lemlem, who formed part of my vision and taught me the good things that really matter in life. The happy memory of my father and mother provides a persistent inspiration for my journey in this life. I am grateful for my three brothers Lt. Col Musie, Eng. Solomon, Eng. Noah, and my three sisters Genet, Yodit, and Hirut, for rendering in me the

sense and the value of brotherhood and sisterhood. I am glad to be one of them. Last but not least, special thanks go to Angela Winn, for being a sister to me and providing me care and support since I came to the USA. Many thanks also to Philipos Hailemichael, whom I have known for more than 10 years now and who showed to be a kind, most helpful, and trustworthy friend.

## Table of Contents

## List of Tables

Page

## List of Figures

Page

## 1. Introduction

Mesoscale meteorologists have given much attention to mesoscale flows in regions of complex topography in coastal areas (for example, Pielke and Cotton 1977, Mahrer and Pielke 1977, Atkinson 1981, Steyn *et al.* 1988, Banta *et al.* 1993, Zhong and Takle 1993, Banta 1995, Cai *et al.* 1999, Darby *et al.* 2002). Complex topography and land-sea effects can produce a diversity of mesoscale phenomena, including: 1) A marine boundary layer with its associated inversion (Bridger *et al.* 1993); 2) Sea-land breezes with their associated return flows (Banta *et al.* 1993); 3) Low-level marine layer jets (McNider *et al.* 1982, Burk and Thompson 1996, Pallabazzer and Gabow 1991); 4) Upslope and downslope winds induced by heating and cooling of mountainous topography (Pielke 1974, Zhong *et al.* 1993); and 5) topographic channeling of planetary boundary layer (PBL) winds (Mahrer *et al.* 1977, Banta 1986).

Typical Mesoscale phenomena cannot be fully described by meteorological observations, due to the scarcity of observational sites, and to the complexity of the dynamics and structure of mesoscale flow phenolmenon. As a result, there is a need to use mesoscale numerical models in combination with meteorological observations to examine the meteorology of mesoscale phenomenon in these areas.

This research will use the versatile Regional Atmospheric Modeling System (RAMS), to temporally and spatially resolve flows in coastal areas with complex topography. Outstanding questions regarding sea breeze structure and marine planetary boundary layer (MPBL) and low-level jet (LLJ) dynamics will be presented and studied in two cases. We have investigated mesoscale flow phenomena for two distinct regions: California's Monterey Bay, and the southeast coast of Eritrea in eastern Africa. Similarities and differences between these two cases are shown in Table 1.

Our two case studies are designed to examine two relevant unsolved problems. For the Monterey case, previous observational research has not been able to detect a sea breeze return flow aloft in the case of a prevailing synoptic offshore flow (Banta *et al.* 1993). This bay has complex inland topography that can influence both the sea breeze and associated return flows (Fig. 1).

For the Eritrean case, a pressing need for the country is the development of new energy supplies. Therefore, we have examined wind distributions as simulated by RAMS over the complex topography of the Eritrean coast, with a view to determining favorable sites for the production of wind energy.

*A. Case 1*

The central California coastal region during spring and summer is characterized by northwesterly flow, which arises due to the high pressure system sitting over the northeastern Pacific about 1000 km northwest of the California coast, together with a thermal low pressure centered over the southwestern United States. Subsidence associated with the Pacific high, coupled with the turbulently mixed marine layer, results in a strong inversion at the top of the MPBL (Burk and Thompson 1996). The dynamics of this region is further complicated by the existence of a LLJ centered at 300-700m above the sea surface and roughly parallel to the coast. The core of the jet lies within the steeply sloped inversion at the top of the MPBL (Bridger *et al.* 1993).

*B. Case 2*

Like the California coast, the Eritrean coast is characterized by a MPBL over the sea, and a strong inversion at the top of this layer (Van Buskirk *et al.* 1997). The region (Fig. 2) is strongly influenced by high pressure systems over North Africa and Saudi Arabia, while a thermal low typically forms over eastern Sudan. The dynamics of this region are also complicated by the existence of a LLJ over the MPBL in the southern Red Sea. The narrow constriction of the Strait of Bab el Mandeb between

Djibouti and Yemen, connecting the Red Sea and the Indian Ocean, acts like a funnel to further accelerate the LLJ (Rosen *et al.* 1999).

*C. Comparison of Case 1 and Case 2*

Table 1 shows a comparison of the two cases. For the Monterey Bay case, the region is located in the mid-latitudes, about 14 degrees above the Tropic of Cancer. The orography of the region is characterized by coastal mountains and valleys. North of the bay are the Santa Cruz Mountains. Further to the south are the Santa Lucia Mountains, and to the southeast is the Sierra de Salina, which encloses the Salinas river valley. To the east are the Gabilan and Diablo ranges, which provide the topographic barrier between the coastal valleys and the San Joaquin valley (Fig. 1).

Case 2 is focused on the East African country of Eritrea, located about 11 degrees south of the Tropic of Cancer. Eritrea has a 1000 km long coastline, which like the California coast, is oriented from northwest to southeast. The sea is on the eastern side of the coastline—the opposite of the California case. Our study is carried out for the Bay of Aseb located along the southern coastal area of Eritrea. Similar to the California coast, the orography of the Eritrean coast is characterized by coastal mountains with elevations ranging from 400 to 700 m, and inland mountains as high as 4000 m. The Red Sea is sandwiched between the

Eritrean and Yemeni coastlines (Fig. 2). The sea surface temperatures (SSTs) of the Red Sea are substantially higher than those along the California Coast, with temperatures of 25-30$^0$C compared to the average of 15$^0$C for the California coast.

Both cases are characterized by a dry season LLJ, which flows from the northwest in Case 1, and from the southeast in case 2. The direction of the LLJ is determined by the anticyclonic circulation of the synoptic high pressure on the seaward side of the coastline. Previous studies have shown that high near-surface wind speeds of about 17 m s$^{-1}$ are observed along the northern California coast near Cape Mendocino when the LLJ accelerates over the coastal mountains and crosses the cape (Burk and Thompson 1996). Similar high winds can be seen at the Eritrean coast, at the coast near Aseb (Van Buskirk *et al.* 1997).

## 2. RAMS Overview

The mesoscale model we use is the RAMS model. This is a highly versatile non-hydrostatic numerical model developed at Colorado State University. It solves the Reynolds-averaged primitive equations, which are described by Tripoli and Cotton (1982). The model uses a quasi-Boussinesq approximation, and "time-split" time differencing (Pielke 2002). The three-dimensional (3D) vector compact form of the equations is presented in Appendix A. These are the compact form of the equations shown in the RAMS technical manual. All symbols are defined in Appendix C.

RAMS uses the Arakawa C staggered grid in which thermodynamic and moisture variables are defined at the grid volume center, and velocity components are defined at half grid points (Mesinger and Arakawa 1976). A polar stereographic map projection is used for the horizontal grid domain, and a terrain-following sigma coordinate system with variable grid spacing is used in the vertical in order to increase the resolution near the surface (Gal-Chen and Somerville 1975, Clark 1977, Tripoli and Cotton 1982). High spatial resolution is attained in the RAMS model by the use of multiple nested grids generated in the area of interest with a technique that allows two-way communication of all prognostic variables between any nested grid and the parent grid.

There are two advection schemes used in RAMS: the leapfrog-type, and the forward upstream scheme. The leapfrog scheme is used for all variables in the leapfrog time differencing, as well as the velocity components in the hybrid time differencing scheme. The forward advection upstream scheme is used on the thermodynamic component of the hybrid time differencing scheme (Tremback *et al.* 1987). For large horizontal grid spacing, vertical diffusion is evaluated from a prognostic turbulent kinetic energy (TKE) equation using a technique developed by Mellor and Yamada (1974), and modified to handle growing turbulence (Helfand and Labranga 1988). The Mellor and Yamada 2.5 order closure scheme is used in RAMS, where subgrid-scale turbulent eddies are parameterized by the prognostic TKE. The horizontal diffusion acts only as a filter for acoustic waves, and is carried out by the deformation-based Smagorinsky scheme (Smagorinsky 1963), which relates the mixing coefficients to the fluid strain or deformation rate, and includes corrections for the influence of the Brunt-Vaisala frequency (Hill 1974) and the Richardson number (Lilly 1962).

The RAMS model uses four-dimensional data assimilation (4DDA) by Newtonian relaxation (nudging) at the model's lateral boundary, top boundary, and interior gird points. Lateral boundary nudging is needed for the introduction of time-varying fields into the model as explained further below. Boundary nudging also helps damp information (waves)

that propagate from the model interior towards the lateral boundaries of the model domain. Boundary nudging is done only on the coarsest grid of a nested grid run. Nudging at the top of the model domain is not widely used. Instead, one can use a Rayleigh friction layer at the model top. This acts as an absorbing layer for vertically propagating topographically induced gravity waves.

There are two techniques in RAMS for nudging model results to atmospheric data sets: so-called analysis nudging and observational nudging. In the *analysis nudging* technique, observational data is first objectively analyzed to produce a gridded analysis, and then the simulated meteorological fields on the model grid are nudged toward the gridded analysis. The *observational nudging* technique nudges only the model fields that are near observational data locations to decrease differences between the model and observations near the observational points. Observational nudging in RAMS is performed with a modified analysis nudging. In this technique, the observations are used to modify the gridded analysis fields, and this produces a new set of analysis fields, which are then used in the nudging algorithm.

The RAMS model can be initialized in two ways: horizontally homogenous and variable initializations. For a variable field model initialization, the 4DDA uses time series of gridded variables of horizontal wind, potential temperature, and relative humidity values that are analyzed

from either observations or large-scale model forecasts (e.g., NCEP, ETA). Vertical velocity is not nudged due to the inadequacy of observations, and the fact that nudging might lead to errors that produce erroneous, divergent horizontal wind fields.

## 3. RAMS Simulation of Monterey Bay Sea Breeze

### *A. Background*

The sea breeze is a mesoscale phenomenon that has been intensively studied. The sea breeze plays a key role in controlling meteorological conditions along coastal areas. Previous investigators have discussed the importance of the sea breeze for problems such as air pollution and smog transport, location and initiation of convection, aviation safety, gliding, sailing and surfing, and forest fire forecasting (Simpson 1994). The sea breeze is driven by the temperature differences between the land and ocean, and consists of onshore flow during the day (sea breeze) and offshore flow during the night (land breeze). Figure 3 shows the diurnal cycle of the sea/land breeze (Pielke 1984). A sea breeze is initiated when air parcels over the land become more buoyant in the column of air over the heated land surface. Parcels expand and rise as the land is warmed by solar radiation (Pielke 1984). The air over the surface of the water is cooler during the daytime hours since the heat capacity of water is greater than that of the land. The vertical gradient of pressure is greater over this cool air than over the warmer landmass due to the greater density of the cool air. This difference between land and sea air columns produces horizontal pressure gradients that generate a sea breeze at low-levels, and a light flow from the land to the sea--a return flow--aloft. As the sea breeze begins and strengthens, strong winds at the land/sea

interface and weaker winds inland imply a low-level horizontal convergence over the land, which implies upward vertical winds and convection. Similarly, strong winds at the land/sea interface and weaker winds seaward imply a lower-level horizontal divergence over the sea, with associated subsidence.

At night, there is a reversal of the sea breeze pattern as radiative cooling makes the land cooler than the sea. This produces a late night and early morning land breeze.

1) FACTORS AFFECTING SEA BREEZE

There is a diversity of factors that can affect the existence, strength, form, and evolution of sea breeze flows. Coastline shape can either enhance or inhibit sea breeze development. For example, the merging of two sea breezes originating from both sides of a peninsula enhances convection (Pielke 1974). On the other hand, over land areas adjoining bays, the sea breeze tends to diverge, which enhances low-level sinking motion, thus reducing cloud cover. Time of the year, latitude, ocean temperature just offshore, depth and stability of the planetary boundary layer (PBL), and factors that alter the land surface energy balance (clouds, land use, albedo, ground wetness) all combine to modify the basic thermal forcing that causes the sea breeze.

Synoptic-scale background flow can enhance or diminish the sea breeze depending on the prevailing synoptic flow relative to the sea breeze forcing. Strong onshore flows may mask the sea breeze completely, while weak offshore background winds are most favorable for the development of a clearly defined sea breeze (Arritt 1993). Stratification and PBL depth determines the depth of the thermal forcing and vertical extent of the induced circulation, and can damp vertical motions and restrict the vertical extent of the sea breeze circulation when stratification is high.

Another factor that can greatly modify the sea breeze is topography. Coastal mountains result in earlier onset of the sea breeze due to additional thermal forcing caused by mountains. They can also have the effect of blocking and channeling sea breeze flows. Finally, clouds both modify and are modified by the sea breeze. They alter the time of onset and location of the thermal gradients, which are responsible for the development, and evolution of the sea breeze circulation.

2) MONTEREY BAY SEA BREEZE

The diurnal evolution of the Monterey Bay sea breeze has been classified by Round (1993) into six types, according to time series of data measured at Fort Ord. They are: gradual onset; clear onset; frontal; double surge; unclassified; and no sea breeze. The *gradual onset* is where

the prevailing gradient flow is enhanced by the sea breeze. The *clear onset* is distinguished by a pronounced increase in the onshore wind speeds. The *frontal onset* is characterized by wind shift, temperature decrease, moisture increase, and wind speed increase. The *double surge* includes all days in which two separate and distinct onshore events occur. The *unclassified* were events, which not fit into the above classifycations, and the days with no see breeze were classified as *no sea breeze.* This classification of the sea breeze resembles that of Wexler (1946).

Knapp (1994) associated the above characteristic patterns of sea breeze onset with different large-scale weather patterns along the west coast, namely: a ridge regime (occurring 13% of the time), a trough regime (occurring 52% of the time), a gradient regime, which is a westerly gradient flow (occurring 27% of the time), and unclassified. This classification was based on synoptic scale sea level pressure patterns from 01 May 1993 to 30 September 1993. The evolution of the sea breeze (according to Round (1993) classification above) is directly related to the above synoptic regimes. When the onshore synoptic flow was in the same direction as the sea breeze, there was a weak temperature perturbation and a weak sea breeze. When there are calm conditions or moderate opposing synoptic flow, the sea breeze is the strongest due to the strong positive thermal perturbation in a region of negative to near-neutral

static stability. When synoptic flow is strong to very strong opposing, the sea breeze is weak to non-existent. On the other hand, Foster (1996) provided a modification of Round's (1993) classification by creating the following categories based on the Fort Ord wind profiler data: frontal, gradual, rapid onset and unclassified.

Sea breeze flows in California are complicated by interactions with both complex coastal topography and the shape of the coastline. Near Monterey, the LLJ is from the northwest and passes substantially west of the mouth of Monterey Bay (Burk and Thomson 1996). When a sea breeze develops, air in the MPBL over the bay flows onshore. As this air is in turn replaced by air in the MPBL from farther offshore, a convergence forms at the mouth of Monterey Bay that produces northwesterly winds at Santa Cruz (at the northern side of the mouth of the bay), and southwesterly winds at Pt. Pinos (Fig. 1 at the southern side of the mouth of the bay) (Foster 1996). The offshore extent of the sea breeze is not well known for the Monterey Bay region, but extends at least 20 km out from the coast (Banta *et al.* 1993), and probably extends beyond the line connecting Pacific Grove to Santa Cruz where it produces the convergence described above.

In a two-dimensional study of the Monterey Bay sea breeze, Derby *et al.* (2002) showed that the complexity of the Monterey Bay region

causes the sea breeze to be more complex than predicted by theory. A conceptual model of the sea breeze was produced from knowledge of the evolution of the vertical structure. Sea breeze forcing occurs on two length scales, the first being the distance between the ocean and coastal mountains, and the second being the larger-scale distance between the ocean and higher inland mountains (Sierras). Their model results demonstrated that the slope flows produced by each mountain range impacted the structure of the sea breeze flow near the surface and the expected return flow aloft. They also showed that the coastal mountains of the Monterey Bay region and the land-water contrast were responsible for the shallow sea breeze. The presence of the inland mountains (the Sierra Nevada range) greatly influenced the coastal flow above 1500 m Above Sea Level (ASL). Since simulations with the inland mountains produced westerly flow above 1500 m, and simulations without it had easterly flow at these heights, this topographic feature clearly affects winds near the shore despite the fact that the mountains are hundreds of kilometers inland. Simulations showed that the interaction between the coastal and inland mountains enhance the onshore flow in the morning hours. The interaction between terrain and the land-water contrast has a strong impact in the afternoon, opposing the sea breeze flow. In the morning, the coastal mountain slope flow enhanced the sea breeze flow, but the mountains obstructed its progress in the afternoon. The interaction

between coastal and inland mountains and the land-water contrast enhanced onshore flow at the surface for the entire time period analyzed.

3) RETURN FLOW ISSUES

There is no consensus on the precise definition of the return flow in a sea breeze system. The sea breeze return flow is a fundamental part of the description of the sea breeze circulation because it is required for mass continuity of the circulation when the sea breeze has a limited spatial extent (Atkins *et al.* 1997). Complications arise when the sea breeze interacts with larger-scale synoptic flows, which can produce net mass flow through the domain of consideration.

Banta *et al.* (1993), in their study of the Monterey Bay sea breeze, pointed out that, although the sea breeze has been studied for quite a long time, there are still issues which are not well understood. These include: the structure and extent of the seaward part; the inland interaction with topography; and the return current. The cost and limitation of meteorological instruments on land and sea, especially measurements of the vertical profile of the atmosphere, means that many questions to remain unanswered. Other problems arise from constraints on the siting of the meteorological instruments, which are mostly installed at locations that are easily accessible. There is therefore a high probability that the detailed data needed for analyzing the more subtle or complex features of the sea breeze may not be available.

To understand some of the complexities of the sea breeze, the 1987 land sea breeze experiment (LASBEX) utilized a Doppler lidar with a scanning capability to measure the vertical wind profile and the horizontal wind fields around Monterey Bay with a measuring frequency of 2 min. The lidar data was transformed into Cartesian coordinates in two ways: first it was transformed to a 100 m horizontal by 25 m vertical grid up to 1.5 km AGL to study the details of the flow structure. Second, it was transformed to a 100 m by 100 m grid to 4 km ASL to look for flow layers at higher altitudes, especially return-flow layers. The lidar data above 4 km ASL was not available due to the low concentration of aerosols at such altitudes (Banta *et al.* 1993).

Examination of the LASBEX dataset, which was gathered during offshore synoptic conditions, found no evidence of compensatory return flow above the local sea breeze. Banta *et al.* (1993) suggested the possible reasons for the missing return flow as follows:

1) Weak return flow (too weak to be detected)
2) Return flow distributed in the vertical in an undetectable way
3) Return flow superimposed on strong large-scale flow
4) Return flow does not exist.

Banta *et al.* (1993) considered that the final reason was the most likely reason that the Monterey Bay sea breeze return flow was undetected. The first explanation was eliminated due to the fact that a 5 m $s^{-1}$

sea breeze must have a relatively strong return flow. They argued that the second explanation was unlikely to be true because strong stability of the atmosphere below 3 km should force any compensatory flow to be at low levels, and the third scenario was dismissed due to the fact that a superimposed return flow should have been detectable given the precision of the instruments.

One possibility that was not considered by Banta *et al.* (1993) is:

5) Return flow is horizontally displaced and may be found to the north or south at different locations along the coastline.

Burk and Thomson (1996), in a study of the structure and dynamics of the summer time LLJ along the California coast, noted that the interaction of the jet with the sea breeze mountain-valley circulation (SBMV) created adjacent (in the north-south sense) areas of convergence and divergence along the California coastline.

Several studies have helped clarify the dynamics of return flows. A number of laboratory observations and numerical simulations have identified and characterized return flows under controlled or idealized conditions (Atkins *et al.* 1997). For example, Tijm (1998) used a two dimensional (2D), dry hydrostatic model and observational data for the study of the sea breeze with its return flow along the coastline of Holland, which has a nearly flat topography and a comparatively straight coastline. The

study showed that there was a return flow layer of 0.5-1.5 km elevation to compensate the sea breeze. The study also showed that the mass flux of the return flow was greater than that of the mass flux of the sea breeze due to the downward vertical advection of warm air into the boundary layer.

In a study of an Oregon sea breeze event, the low-level land-sea breeze flow was entirely contained in the marine layer, and the return flow aloft above the inversion appeared as surges, which responded to the surges on the sea breeze flow (Johnson and O'Brien 1973). Finally, when helicopter observations were made of the sea breeze at Tosa Bay, Japan, the structure of the sea breeze over the sea had well-defined features. In particular, a turbulent wake was found behind the head of the sea breeze front, and a closed sea breeze circulation cell containing subsidence of the return flow was observed (Chiba 1998).

## 4) CASE SELECTION AND SYNOPTIC CONDITIONS

For Case 1 of this research study, we selected two simulation periods based on the ability of RAMS to simulate the cases, and based on the existence of clearly identifiable sea breeze flows. In preliminary simulations, we found that RAMS did not accurately simulate temperatures when low clouds and fog were prevalent in Monterey. We therefore set the following criteria for simulation case selection: a strong, stable stratification of the PBL; clear sky conditions around the Monterey Bay area;

and a clear sea breeze surface wind at Monterey (i.e., onshore during the day, and offshore at night). We picked two distinct sets of synoptic conditions for our simulation periods: the first (Case 1A) is a strong offshore case characterized by a prevailing offshore background wind at 700 mb pressure level; and the second (Case 1B) is a weak offshore case with a prevailing northerly wind. The two periods were selected based on careful examination of wind profiler data from Fort Ord (Figs. 4 and 5).

During the strong offshore period, which began at 0000 UTC 24 October, the 700 mb analysis (Fig. 6a) shows a broad Eastern Pacific high pressure ridge with a height of 3200m centered at (39N, 129W). Meanwhile a thermal low-pressure area was located over central California and Nevada, with a pressure height of 3140 m, and centered at ($37^0$N, $118^0$W). A synoptic high of 3160 m was also present at the tri-point border of California, Arizona, and Mexico. 700 mb wind flow was thus northeasterly at 15-20 m $s^{-1}$ over central California, with temperature ranges from $5^0$C at Reno to $9^0$C at Oakland and $10^0$C in the Monterey Bay region. At 0000 UTC 25 October (Fig. 6b), the eastern Pacific high pressure had intensified to 3200 m, and moved northwest to be centered at ($44^0$N, $132^0$W). There was a resultant change in the winds, which shifted to northerly over the coast of central California, and northeasterly inland. Temperatures had also increased by $2^0$C at the coast and $3^0$C inland. The synoptic high and the thermal low had moved

southeast towards Mexico. At 0000 UTC 26 October (Fig. 7a), the eastern Pacific high had further intensified (by 50 to 3250 m), and moved further towards the northwest with the ridge axis penetrating inland over the Pacific Northwest. Another low pressure had developed over the Monterey Bay region, with a height center of 3230 m located at (38$^{0}$N, 122$^{0}$W). Winds were thus blowing east northeasterly over the central coast of California, and there was a significant increase in temperature to 13$^{0}$C in Oakland and a decrease to 7$^{0}$C over Reno. At 0000 UTC 27 October (Fig. 7b), the eastern Pacific high had progressed south and east to (44$^{0}$N, 130$^{0}$W) and had weakened by 10 m, and the low over Monterey Bay had filled. There was an increase of wind speed of between 7.5 m s$^{-1}$ (15 knots) over the central coast and 5 m s$^{-1}$ inland. Temperatures remained unchanged over Oakland, and had increased by 2$^{0}$C over Reno. At 0000 UTC 28 October (not shown), the eastern Pacific high had migrated to the south and expanded to the east, forming a double ridge, with the eastward high having height 3270 m at (39$^{0}$N, 129$^{0}$W), the same location that the eastern Pacific high occupied at the beginning of our analysis period at 0000 UTC 24 October. No significant wind field change was observed over the central coast over this 24 hour-period, but wind speeds had slightly increased inland.

In response to the upper level flows, surface fields were also changing across the region. At 0000 UTC 24 October, the surface eastern Pacific high of 1032 mb was centered at (47$^{0}$N, 124$^{0}$W). To the east, a cold front had crossed Nevada, and a stationary front was indicated along the Sierras (Fig. 8a). An inverted thermal low was located over northern California, with the trough axis oriented N-S over San Francisco bay. A low-pressure system (1006 mb) centered at (34N, 115W) was also present associated with the upper level low at the southeastern California border with Arizona. Central California was dominated by northerly winds, which ranged from 7.5-10 m s$^{-1}$. Temperatures ranged from 13-17$^{0}$C over the coast, to 26-29$^{0}$C over the San Joaquin valley. At 0000 UTC 25 October (Fig. 8b), the surface eastern Pacific high had strengthened by 5 mb and penetrated far inland into south central British Columbia (centered at 52$^{0}$N, 120$^{0}$W). The cold front had decoupled from the warm front, and had been pushed south by the high-pressure ridge approaching from the north. The inverted thermal low strengthened, and the low associated with the cold front weakened by 2 mb. Wind speeds decreased to 2.5-5 m s$^{-1}$, coastal temperatures along central California remained unchanged, and inland temperatures increased by 3$^{0}$C. At 0000 UTC 26 October (Fig. 9a), the eastern Pacific surface high pressure had strengthened to 1040 mb, and had pushed south into the intermountain west. The cold front was

pushed far towards Mexico and the warm front was had dissipated. The thermal low had further intensified and expanded north with the trough axis aligned over the central California coast. Coastal winds were northerly and had increased in strength. Temperatures increased further by 5$^{0}$C over the central coast and by 2$^{0}$C inland. At 0000 UTC 27 October (Fig. 9b), the surface charts show that the center of the eastern Pacific high had retreated southwest to a center at 43$^{0}$N, and 137$^{0}$W, and slightly weakened (to 1031 mb). The thermal low along the central California coast had weakened and pushed slightly offshore towards northern Oregon. Another low pressure developed over the southern coast of California, with a pressure center of 1017 mb. Wind directions were still northerly and wind speeds decreased by 2.5-5 m s$^{-1}$. Inland temperatures further increased by 2$^{0}$C over central California, and decreased by 1$^{0}$C over the coast. At 0000 UTC 28 October (not shown), the high slightly weakened but maintained its position. The thermal low over Oregon strengthened and moved south to the California coast where it had slight inland penetration. The low pressure in southern California persisted in its position, and had intensified by 5 mb. Wind directions shifted to northwesterly, and no significant change was observed in temperatures.

The synoptic pattern changed very little over the Monterey Bay region during the weak offshore case (case 1b). The upper-level flow (700 mb) fields were characterized by southwesterly flow downstream from a

broad quasi-stationary upper-level trough over the eastern Pacific Ocean, and a jet stream of 20-25 m $s^{-1}$ extending from northern California to British Colombia. At 0000 UTC 15 March, (Fig. 10a), the eastern Pacific high pressure (3220 m) was located west of the Monterey Bay region, centered at ($34^0$N, $126^0$W), with its ridge axis pushing along the central coast. The central California coast was dominated by light and variable winds directed northeastward. Temperatures ranged from 5-$7^0$C along the coast to 1-$2^0$C inland. At 0000 UTC 16 March (Fig. 10b), the high pressure had moved slightly offshore with its trough axis pointing to Oregon. A synoptic high-pressure system had also developed over southern Nevada, parallel to the Pacific high. No significant change had been observed on the wind speeds and temperatures, but wind directions at the central coast had become more northeasterly. At 0000 UTC 17 March 2004 (Fig. 11a), the high pressure had moved back slightly onshore maintaining its strength. The inland synoptic high pressure had filled. There was no significant change in winds and temperatures over central California, but wind speeds had decreased over southern California. At 0000 UTC 18 March (Fig. 11b), a deep low centered over the west coast of northern Canada had pushed south and strengthened the jet by 5 m $s^{-1}$. The high pressure had moved offshore centered at ($33^0$N, $135^0$W) and had weakened by 4 m. During this period, winds had become calm but there was no significant change in temperatures. Generally, the 700

mb fields were stable and consistent during the weak offshore period of simulation.

Surface synoptic plots for the weak offshore case, (1b) were characterized by an eastern Pacific high pressure of 1030-1032 mb, centered west of Washington. This high-pressure system showed little movement during the period of 0000 UTC 15-17 March (Figs. 12a-13a). During this period, a trough was also present over central California. Temperatures ranged from 11-13$^{0}$C over the coast, to 26-29$^{0}$C inland. Wind speeds were light and variable, and were northerly to weak onshore. At 0000 UTC 18 March (Fig. 13b), the high-pressure system had moved south centering west of northern California. The trough had filled, and inland temperatures had increased by about 3$^{0}$C, ranging from 28-31$^{0}$C. Wind speeds were calm inland, but weak onshore over central and southern California.

*B. Methodology*

1) METHODOLOGY OVERVIEW

Simulations with RAMS (version 4.4) have been performed for the two cases discussed above. For both cases, a four day simulation period was chosen based on the Naval Postgraduate School (NPS) wind profiler data from Fort Ord. The first simulation period (strong offshore winds, Case 1a) covers the period 0000 UTC 24-28 October 2003, and the second (weak offshore, Case 1b) comprises the days from 0000 UTC 15-18

March 2004. These two cases were chosen so that the simulations would be comparable to the most detailed available observational study of the Monterey sea breeze return flow analyzed by Banta *et al.* (1993). In the Banta study, the highlighted sea breeze cases were those with an abrupt sea breeze transition that had easterly or northeasterly upper-level synoptic flows. To cover the range of offshore cases, this study selected both strong and weak offshore periods for simulation. RAMS simulations of the two cases were conducted, and model results were validated against and compare to observational data. The results were then examined for the existence of a sea breeze return flow aloft.

## 2) MODEL SETUP

The RAMS simulations focused on the analysis of the sea breeze and return flow dynamics in the Monterey Bay area. For this purpose, a nested-grid configuration was implemented. The outer model domain was extended eastward to include most of the western United States, and westward a considerable distance seaward (Fig. 14). Finer nested grids were applied over the area of interest in order to obtain meteorological fields at high resolution.

In order to select the most suitable nested grid configuration, several test simulations were performed. Three nested grids were chosen to select important physical features of the meteorology. The domain for the outer grid was set to be large enough to capture the synoptic high-

pressure systems important for our two simulation cases. The second grid was selected to capture the Sierra Nevada mountain range and its influence on the dynamics, and the third grid was chosen to resolve the details of the coastal mountains near Monterey. The detailed configuration that was selected and applied to both periods of simulation was:

- Grid 1: A coarse grid with a mesh of 80x80 points and 40 km horizontal grid increment.
- Grid 2: A medium grid with a mesh 82x82 points and 10 km horizontal grid increment.
- Grid 3: A fine grid with a mesh 62x62 points and 2.5 km horizontal grid increment.

All grids were centered at the domain coordinate of 36.80$^0$N and 120.78$^0$W (Moss Landing). Concerning the vertical structure, the grids were identical. In detail, 50 vertical layers with grids above the first level increase by a grid stretch ratio of 1.2 had been used. The vertical resolution was dense in the lower levels, and became increasingly coarse toward the top of the domain, which was set at 30 km.

3) INITIALIZATION AND INPUT DATA

Initialization of the RAMS simulations requires four types of input data: (1) topographic data that characterizes the elevation of the land surfaces; (2) sea surface temperature data that provides the temperature

of the sea surface over the Pacific Ocean; (3) vegetation data that characterizes land surface characteristics; and (4) meteorological data that characterizes meteorological fields at the initial time, at the boundaries, and at synoptic distance scales. We describe each of these inputs in turn.

- *Topography files:* The USGS topography data set of 30 arc-seconds (about 1 km) resolution was used. From the topography data set, the land-water percentage was extracted using RAMS.

- *SST files:* The SST data set from RAMS consists of mean climatological monthly values with a resolution of 1 degree (about 111 km).

- *Vegetation files:* The vegetation data set was in gridded form with a resolution of 30 arc-seconds (about 1 km) and global coverage. The vegetation data have been retrieved from the United States Geological Survey (USGS). The USGS dataset is based on 1 km Advanced Very High Resolution Radiometer (AVHRR) data spanning April 1992 through March 1993 (Walko and Tremback 2001).

- *Meteorological fields:* The model was initialized with gridded data sets prepared by the isentropic analysis package embedded in RAMS. They contain the following fields: horizontal velocity components, temperature, geopotential height, and relative humidity as a function of pressure. These initial fields are used in order to

generate a time series of observational data for the RAMS model to assimilate during execution. The lateral boundary region of the coarsest grid is nudged toward the initialization file values every 6 hours, while there is no relaxation time scale at the center of the domain.

The primary meteorological data was retrieved from the National Center for Environmental Prediction (NCEP). Their horizontal increment is 0.5 degree, and data are available every 6 hours (0000, 0600, 1200 and 1800 UTC). In addition, sounding and surface meteorological data from the University of Wyoming were used for model initialization and validation. The lateral boundary conditions on the outer grid followed the Klemp-Lilly condition, which is a variant of the Orlanski condition. Here, gravity wave propagation speeds computed for each model cell are averaged vertically, with the single average value being applied over the entire vertical column. The horizontal diffusion coefficients were computed as the product of the horizontal deformation rate and a length scale squared, based on the original Smagorinsky (1963) formulation. The vertical diffusion coefficients were computed according to the Mellor and Yamada (1974) parameterization scheme, which employs a prognostic turbulent kinetic energy variable. For both shortwave and long wave radiation parameterizations, the scheme described by Mahrer and Pielke (1977) has been used.

The roughness length is defined according to the vegetation cover. The simulation also allowed for the condensation of water vapor to cloud water, and the microphysical parameterization of any species of liquid or ice. The mean rain, snow, aggregate, graupel or hail droplet diameter was specified from the default value in the RAMS code. The number concentration is diagnosed automatically from this mean diameter and the forecast mixing ratio.

*C. Results*

1) MODEL VALIDATION

To have confidence in the simulations, validation of the model results against available observations was carried out. For both simulation periods, the model reproduced the synoptic scale forcing, namely the locations of the high and low-pressure systems very well (not shown). To gain insight into how well the model simulation depicted the thermal forcing of the low-level flow, the model surface temperature fields were compared to observations. Time series of surface temperature (hereafter temperature) at different stations around the Monterey Bay area were examined. The station at Monterey was taken as a representative station for the immediate coast, Salinas and San Jose for the coastal terrain, and Fresno and Modesto for the inland valley.

*(i). Strong Offshore*

During the strong offshore case, model temperature comparisons with observations showed reasonable agreement in general. For the Monterey station (Fig. 15), day and night model temperatures were in a good agreement with observations except that the sharp morning peak in temperature is not fully resolved in the simulation. The Salinas station also shows reasonably good agreement between model and observation, agreeing to within $2^0$C (Fig. 16). Comparison at the station in San Jose (Fig. 17) shows excellent agreement between the model and observations throughout the simulation period. For the inland valley stations, temperature plots show that model overestimated nighttime temperatures, were too warm, whereas daytime temperatures agreed well, especially in the morning when the winds were calm (Figs. 18-21). At this time, there was a substantial snow pack in the Sierras that was not included in our simulations. As a result, cold air coming down slope from the Sierras could have cooling effect at these stations.

*(ii). Weak Offshore*

For the weak offshore case, model and observed surface temperatures also showed good agreement. Surface temperature comparisons for Monterey showed a reasonably good agreement (Fig. 22). Due to the proximity of the station to the ocean, a cold low-level sea breeze front from the MPBL moderates the temperature at the station, and thus the

plot of temperature vs. time is not a smooth sinusoidal curve. The model captured the day and night temperatures very well with the exception of the morning daytime spikes observed on the second and third days. At the Salinas station (Fig. 23), both the daytime and nighttime model temperatures were in good agreement with observations except for small deviations just before sunrise on the third and fourth nights of the simulation. San Jose daytime temperature fit matched very well; nighttime observation temperatures were missing data records at the station (Fig. 24). At the inland valley stations of Sacramento (Fig. 25) and Modesto (Fig. 26), the model showed good agreement with observations, but overestimated surface temperatures during the night, especially before dawn on the third and fourth days of the simulation period. This could be attributed to the proximity of the stations to the Carquinez Strait, which allows cool, foggy air from the Pacific to create a strong nighttime inversion near the ground in the Central Valley near the California Bay-Delta. This was not seen at the Fresno station (Fig. 27), which is further from the Bay-Delta and where the model captured nighttime and daytime temperatures very well.

Finally, to develop confidence in the SST data used in the model, a time series comparison plot of model (climatology SST data that was used to initialize the model) vs. observed SSTs at a buoy 49 km from

Monterey is shown in Fig. 28. This plot shows that there were no significant errors in the climatology SST data used to initialize the model.

2) ANALYSIS

In order to separate mesoscale sea breeze and mountain/valley effects from the synoptic wind fields, we developed a method of separating wind fields into a background component, and a daily perturbation. We selected as our background flow the relatively calm wind field that exists early in the morning before solar heating effects have had time to induce mesoscale winds. We therefore defined the background wind field for a particular time to be the weighed average of 0700 LST wind fields immediately before and after that particular time. The weighted average for these two consecutive days provides an estimate of the effect of the background flow between the consecutive 0700 LST wind fields. For example if A is the 0700 LST wind field on the first day and B is the 0700 LST wind field on the next day, the background wind at time t UTC in that day would be {A*t/24 + B*(24-t)/24}. Finally, the weighted average background wind field for each time was then subtracted from each total wind field from the model to produce the daily perturbation wind fields caused by solar heating, sea breeze, and mountain/valley effects during the 24-hour cycle.

This method of subtracting the background wind from the total wind fields was very helpful in analyzing the three dimensional structure

of the Monterey Bay sea breeze. The development and inland penetration of the sea breeze, and upslope-downslope winds over the coastal mountains and Sierras were clearly identified via these difference fields. The technique also aided in the identification of locations of convergence and divergence in the perturbation wind fields.

*(i). Overview*

The first step in the analysis of the RAMS model results was taken by examining the perturbation wind fields every hour for the two simulation periods. The three dimensional evolution of the sea breeze over the Monterey Bay region was determined by examining two-dimensional perturbation wind fields at various levels above the surface. Horizontal distributions of winds were plotted at four levels, namely: 1000, 925, 850, and 700 mb. For grid two, the analysis was done in order to understand the dynamics of the region extending to the Sierra Nevada Mountains. For grid three the analysis examined the dynamics of the local effects, and was focussed over the Monterey Bay region. As mentioned above, the 0700 LST wind fields were considered as the background wind fields, and weighted averages of these fields were subtracted from all fields to study the mesoscale dynamics of the perturbation fields. In addition, vertical velocity fields were plotted for grid three to see the upward and downward motions induced by the coastal mountains as well as the sea breeze. Vertical cross sections of the wind fields at the latitude of Moss

Landing were also produced to analyze the vertical structure of the sea breeze. These plots assisted in analyzing the local circulations near the coastal mountains.

*(ii). Strong Offshore*

We illustrate the results for the strong offshore simulation period with perturbation wind fields focusing on the two days from 1600 UTC 25 to 1600 UTC 27 October. This period is after model spin up, and synoptic conditions at the time were fairly stable.

For the strong offshore simulation period, the grid two analysis at the surface shows some interaction among the coastal sea breeze, up-slope winds in the Sierra Nevada Mountains, and a complex 2D structure that can possibly complicate the return flow dynamics for Monterey. Figure 29 illustrates the evolution of the mesoscale perturbation flow at the 1000 mb level at 2000 UTC 25 October. The sea breeze is observed at the coast of California, and the upslope winds over the Sierras are also evident. Perturbation winds in the Monterey Bay were flowing perpendicular to the coast, and the sea breeze winds over the Monterey Bay region were approximately 3-4 m $s^{-1}$. The sea breeze in the San Francisco Bay was stronger and had penetrated far inland, being channeled through the Carquinez Strait, where the flow then joined the upslope winds on the eastern slopes of the Sierra Nevada. As the day progressed, the sea breeze and the upslope winds peaked at 0000 UTC

(Fig. 30), with a strong sea breeze along the coast of 6-8 m $s^{-1}$ and upslope winds of 4-6 m $s^{-1}$. The sea breeze is strongly channeled at gaps or passes in the coastal range near San Francisco Bay, at Monterey, and near San Luis Obispo. The sea breeze at the Monterey Bay has not penetrated to the San Joaquin valley at the surface due to blockage provided by the mountains to the east. By 0400 UTC 26 October (Fig. 31), the sea breeze and upslope winds had started to weaken and rotate counter clockwise and winds were from northwest at the base of the Sierras over the San Joaquin valley.

At the 925 mb level, a very strong interaction is seen between the sea breeze and the upslope Sierra Nevada winds. At 2000 UTC 25 October, the 925 mb wind field (Fig. 32), shows little evidence of the sea breeze at this level along the central California coast, but 4-10 m $s^{-1}$ upslope winds over the eastern Sierra Nevada mountains can be seen. The perturbation winds were blowing from the south over Monterey Bay as well as over San Francisco Bay. By 0000 UTC 26 October (Fig. 33), the sea breeze at Monterey Bay had speeds of 3-6 m $s^{-1}$ and had started to penetrate further inland into the southern San Joaquin valley, where it merged with the Sierra upslope winds. Coastal mountain winds in northern California appear to be separated from the Sierra Nevada upslope winds by calm conditions in the Central Valley. The San Francisco Bay sea breeze was weaker (1-4 m $s^{-1}$) and had not connected

with the Sierra up-slope flow. By 0400 UTC 26 October (Fig. 34), the sea breeze along the California coast started to weaken. Downslope winds (2-4 m $s^{-1}$) started to develop over the northern San Joaquin valley at the base of the Sierra Nevada Mountains. These winds merged with the residual sea breeze, producing and were flowing northwesterly in the central San Joaquin valley. In summary, during the early part of the day, the sea breeze appears to be shallow under these conditions (and not seen at the 925 mb level along the coast), but as the day progresses, the sea breeze deepens, and flow passes over the coastal mountains to merge with upslope winds in the southern San Joaquin Valley.

In the 700 mb perturbation wind fields, we can see features of what appears to the sea breeze return flow dynamics. At 2000 UTC 25 October (Fig. 35), the 700 mb wind fields show divergence at the crest of the central and southern Sierra Nevada Mountains. An upper-level return flow has started to develop from these Sierra peaks relative to the mean flow. These return flow winds (1-4 m $s^{-1}$) are flowing over the central and southern California coastal mountains. However, perturbation winds were calm over the San Francisco Bay region at 700 mb. During 0000 UTC 26 October (Fig. 36), there was a broad area of divergence over the higher mountains in the Sierras extending the central California all the way to the southern Sierra Nevada Mountains. This divergence was associated with a return flow (1-4 m $s^{-1}$) all along the central California

coast including over the Monterey Bay region. Analysis of the higher resolution grid (grid 3) of the Monterey Bay region for this time shows a clear offshore flow (Fig. 37) of 2-4 m $s^{-1}$ at 700 mb.

Higher resolution perturbation wind fields were also analyzed during this simulation period to examine the complex 3D structures of the sea breeze and mountain-valley winds in this area. Analysis of the horizontal wind was carried out at the above-mentioned levels: 1000, 925, and 700 mb. Surface evolution of the sea breeze for this case showed similar flow to the observed wind profiler sea breeze. Surface perturbation winds showed that there were light and variable winds in the Salinas valley through 1800 UTC 25 October (not shown), but a well-developed onshore flow had developed at 2000 UTC, with flow through the Pacheco Pass and the 101 Corridor and across the Monterey Bay (Fig. 38). The sea breeze started to develop around the Monterey Bay region, with southerly flow in the upper portion of the Bay towards Santa Cruz and northerly on the lower part. Westerly flow started to develop over Moss Landing towards the Pacheco Pass. Upslope winds were developing over the coastal mountains with convergence over the mountaintops. By 0000 UTC 26 October (Fig. 39), the sea breeze had strengthened to 5-10 m $s^{-1}$ and had filled the Pacheco Pass and Salinas valley. By 0400 UTC 26 October (Fig. 40), the sea breeze had diminished.

The 925 mb perturbation winds were also analyzed for the third grid. These wind fields show that at this higher level, the development of the sea breeze is not confined to the Monterey Bay area, but instead the sea breeze passes over the coastal mountains into the San Joaquin valley (Fig. 41). The 700 mb perturbation wind fields also show the weak off-shore flow in the Monterey Bay region that arises from the divergence of the horizontal perturbation wind fields over the Sierra Nevada Mountains (Fig. 42).

To analyze the vertical structure of the Monterey Bay sea breeze and its return flow, the x-z wind fields and vertical velocity contours were plotted for grid 2. The grid extends 400 km seaward and inland, and includes the Sierra Nevada Mountains. The vertical slice was located 5 km south of Moss Landing, which was the center of the grid domain. In the vertical, the plot extends above 6 km. At 2000 UTC 25 October 2003 (Fig. 43) the vertical structure was characterized by strong offshore winds generated by the synoptic flow that accelerated air descending down the western side of the Sierra Nevada mountains. The offshore flow also accelerated as it passed over the coastal range, so that strongest winds occurred at an elevation of 1 km as air flowed out into the Pacific.

Four hours later (Fig. 44) the offshore flow in the lower 3 km over the ocean had diminished in magnitude; there was a weak onshore sea

breeze at Monterey, and upslope flow at the base of the Sierra Nevada mountains in the lowest 200 m of atmosphere. In contrast, the flow above 4 km appears to be slightly stronger offshore than at 2000 UTC. The vertical velocities associated with the Sierra Nevada Mountains are much stronger than those associated with the Monterey sea breeze.

By 0400 UTC 26 October (Fig. 45) the vertical profile appears to show a deep synoptic offshore flow with little sign of sea breeze. The upward vertical flows are on the eastern sides of mountains, while the downward vertical velocities are along the western slopes of the mountain ranges.

(iii). *Weak Offshore*

Similar analyses of the weak offshore simulation period were conducted using with perturbation wind fields for two days. After model spin up, and with fairly stable synoptic conditions, the results for the two days from 1600 UTC 16 March 2004 to 1600 18 March 2004, were analyzed and found to be approximately the same as each other. For the weak offshore case, the grid 2 analysis of the surface flow shows a strong interaction between the coastal sea breeze and upslope winds in the Sierra Nevada Mountains, and a resulting complex 2D structure similar to the strong offshore case. At 2000 UTC 16 March at 1000 mb (Fig. 46), the sea breeze had started to develop all along the California coast, with perturbation winds perpendicular to the coast. Perturbation winds at

Monterey Bay were 3-5 m $s^{-1}$, and had started to interact with the coastal mountains. The sea breeze (4-5 m $s^{-1}$) over the San Francisco Bay was being channeled through the Carquinez Strait. Upslope perturbation winds of 2-8 m $s^{-1}$ had started to develop all along the Sierra Nevada Mountains. At 0000 UTC 17 March (Fig. 47), the sea breeze winds had strengthened all along the California coast, with the strongest sea breeze winds (8-11 m $s^{-1}$) in the Monterey Bay region. Flow through the San Francisco Bay region had already merged with the upslope winds along the Sierras. As was also seen in the strong offshore case, the sea breeze in the Monterey Bay region did not merge with the upslope winds at the Sierras due to the blockage of the coastal mountains. By 0400 UTC 17 March (Fig. 48), the sea breeze along the coast and the upslope perturbations winds over the Sierras had started to weaken. As a result, northeasterly winds were blowing over the central San Joaquin valley.

Perturbation winds at 925 mb were also analyzed for the weak offshore case. At 2000 UTC 16 March (Fig. 49), the sea breeze was already deep enough to be seen at this level along the central California coast. The perturbation winds over the Monterey Bay were 1-4 m $s^{-1}$, and flow had already started to cross into the San Joaquin valley, while the sea breeze at the San Francisco Bay was weaker (1-2 m $s^{-1}$). Strong upslope perturbation winds of 6-15 m $s^{-1}$ had also developed over the Sierra Nevada Mountains. By 0000 UTC 17 March (Fig. 50), the sea breeze had

developed to full strength (6-9 m $s^{-1}$) with flow through the southern San Joaquin valley. Flow had merged with upslope winds along the southern Sierra Nevada Mountains. At 0400 UTC 17 March (Fig. 51), the sea breeze had started to retreat, and downslope winds had started to develop in the northern Sierra Nevada Mountains. There was a convergence zone between downslope perturbation winds and the sea breeze flow over the Carquinez Strait.

Analysis of the 700 mb perturbation wind field was also carried out to detect the return flow. At 2000 UTC 16 March (Fig. 52), the 700 mb wind fields show divergence at the central and southern peak of Sierras. Similar to the strong offshore case, an upper-level return flow associated with the mountain breeze had started to develop from the Sierras. These return flow winds (1-5 m $s^{-1}$) flowed over the central and southern California coastal mountains. At 0000 UTC 17 March (Fig. 53), there was a broad area of divergence over the higher mountains in the Sierras extending from central California all the way to southern Sierra Nevada Mountains. This divergence strengthened and had created southeasterly perturbation winds over the San Joaquin valley and Monterey Bay regions. By 0400 UTC 17 March (Fig. 54), the return flow had propagated out from the Sierra Nevada Mountains and covered all of the San Joaquin valley and the central California coast. Over the

Monterey Bay region and San Francisco Bay, offshore flows of 2 m $s^{-1}$ from the southeast can be seen.

For the weak offshore case, a vertical slice of the velocity field shows much more clearly the sea breeze and upslope wind circulations. For 2000 UTC 16 March 2004 (Fig. 55), the sea breeze and upslope low-level circulations can be seen clearly at the base of the coastal mountains and the Sierra Nevada mountains, respectively. What is particularly interesting about the figure is that the vertical velocities associated with the Sierra Nevada mountain upslope flows are an order of magnitude larger than those associated with the sea breeze and coastal mountain/valley winds. In addition, the upslope winds at the Sierra Nevada Mountains are producing very large horizontal divergences at an elevation of 4-6 km, above the mountaintops.

At 0000 UTC 17 March 2004 (Fig. 56) the vertical slice shows several important features of the combined sea breeze/upslope wind flow structure. The sea breeze circulation is now clearly linked with the circulation induced by the Sierra Nevada upslope flow. While some of the onshore sea breeze rises above the coastal mountains, some also flows over the coastal hills and into the central valley, then flowing up the Sierra Nevada Mountains. The largest vertical flows are again above the Sierra Nevada Mountains, and produce a large area of horizontal divergence above the mountaintops. The combined sea breeze/upslope circula-

tion appears to produce a deep, weak return flow at an elevation ranging from 1 to 4 km above the ocean west of Monterey. One can also see a large area of weak downward motion in the return flow at distances of 50 to 300 km offshore. The very large scale of this combined sea breeze/-upslope flow circulation provides one explanation of why Banta *et al.* (1993) did not find a clear return flow in an observational study that focused on the Monterey Bay area.

In our simulations, the best time to see return flows appears to be early in the evening. At 0400 UTC 17 March 2004 (Fig. 57), the upslope flows over the Sierra Nevada Mountains have diminished, and the main vertical velocities are those induced by the synoptic-scale offshore flow. Hence, they are upslope on the eastern side of the mountains, and down-slope on the western side. At this hour, there is still an onshore sea breeze below 1 km elevation, and a broad area of return flow between 1 and 4 km altitude. The return flow air has two sources of supply: the first is the ascending upslope winds that rise from of the tops of the coastal hills; the second is the upslope winds rising from the western slope of the Sierra Nevada Mountains.

In summary, the Monterey Bay sea breeze circulation consisted of a weak thick return flow of 1-3 m $s^{-1}$ in a layer from 1 to 4 km elevation, would have been extremely difficult to detect when there is a 5-10 m $s^{-1}$ synoptic background flow at that level. In addition, the Banta study was

able to take measurements only over a limited area near Monterey, when the return flow structure is dispersed over a wide geographic area extending to the Sierra foothills. A conceptual model of our result is shown in Fig. 58 to help us visualize the sea breeze dynamics of the Monterey Bay region.

## 4. RAMS Simulation of Southeastern Eritrea Coastal Winds

### *A. Background and Motivation*

Eritrea, an African country along the Red Sea coast, needs a rapidly growing supply of energy in order to satisfy the increasing needs of its people. In providing for the rapidly expanding electricity needs of its population, Eritrea faces two major constraints: environmental impacts and cost. Wind energy holds the potential of providing a significant contribution to Eritrea's electricity needs using a means that is both environmentally friendly and low cost (Garbesi *et al.* 1996). Another major benefit of wind energy for Eritrea is that it can help decrease the national reliance on the expensive, imported diesel fuel and fuel oil that is currently used for electricity production.

An essential component of wind energy development is determining the geographic distribution of wind energy resources. This involves determining wind speeds to a high degree of accuracy. The power density of the wind determines the amount of power that can be produced by a given wind generator, and the power density is proportional to the third power of the wind speed. Therefore, a 10% increase in wind speed produces a 33% increase in wind power.

Eritrea is a country located in the eastern part of Africa, with one thousand kilometers of coastline along the Red Sea. Our research is

focused on the southern part of the Eritrean coast, which has been identified as the country's best wind energy resource region (EDOE report 2000). We show the southern extreme of the Red Sea in Fig. 2 (presented in the case comparison section). At the southwestern boundary of the Red Sea is Southeastern Eritrea. Adjacent to the coast is a flat coastal plain, while parallel to the coast and 5-50 km inland is a range of coastal hills that vary from 1000 to 2000 m in elevation. West of the meridian at $40^0$E, we have the 2000 m Eritrean highland plateau, which extends from the north to the south of the country. In the southeast, at the extreme southern end of the Red Sea lies the straight of Bab el Mandeb, which is a constriction of about 35 km between Aden and Djibouti that connects the Red Sea and the Indian Ocean (Fig. 2). The locations of the meteorological stations in the southern coast are also shown in Fig. 2.

The goal of this investigation is to increase knowledge of the distribution of wind energy resources of Southeastern Eritrea by understanding the mesoscale meteorology of the region. Some key questions regarding the Southeastern Eritrea wind energy resource include:

- **Hills or Coastline:** Are the wind resources greater on the hills or over the sea?

- **Extent of Resources:** How far along the NW-SE coastline do excellent wind resources extend?
- **Vertical Wind Shear:** How does wind power depend on altitude? Is it very beneficial to have extremely tall wind turbines?
- **Best Wind Resources Location:** Where are the highest performance wind energy generation sites?

In the following sections, we review previous studies, describe the particular case that we simulate, describe the simulation set-up and methodology, present simulation results, and conclude with implications for further wind energy resource studies.

## 1) PREVIOUS STUDIES

Previous research on wind energy resources in Eritrea and the surrounding area has relied primarily on collecting and analyzing ground station data on wind speeds, with some preliminary efforts at performing mesoscale simulations for the southeastern coast. Some of the earliest studies (Mulugeta and Drake 1996) identified the Aseb area of Eritrea as an area of high wind potential. Further general assessment studies (Garbesi *et al.* 1996; Van Buskirk *et al.* 1998; Rosen *et al.* 1999) provided more detail on the potential of the southeastern coast and central highland passes. In addition to meteorological data, these studies examined

ship-based meteorological measurements (Rosen 1998), and satellite scatterometry data (Van Buskirk *et al.* 1998). More recent investigations (Habtetsion *et al.* 2002) have analyzed data from 25 recently installed meteorological stations. Consultant studies (Lehremeyer 2000) have conducted simulations using the German mesoscale atmospheric model KLIma Model Mainz (KLIMM) in an effort to extrapolate meteorological station data to a wider geographic area, but did not capture well-known wind dynamics of the southern Red Sea area. Other consultant studies (SWECO 2002) attempted to geographically extrapolate station data using the Wind Atlas Analysis and Application Program (WAsP), but extrapolations based on land-based station data did not accurately forecast the wind speeds over the Red Sea that are indicated by ship-based measurements, and overestimated mountaintop wind speeds.

The current investigation is needed because the studies that have been performed to date have not provided consistent answers regarding the extent and features of the Southeastern Eritrea wind energy resources that are important for an accurate and well-resolved resource assessment. With respect to whether or not the best wind resources are in coastal waters or at the tops of coastal mountains, different studies and investigations have provides varying results. Scatterometry and ship-based measurements (Rosen 1998, Van Buskirk *et. al.* 1999) indicate the existence of a LLJ that appears to be centered in the middle of southern

portion of the Red Sea. Meanwhile WAsP calculations (SWECO 2002) indicate very high wind resources on the tops of hills and mountains. Furthermore, unpublished investigations indicate that low hills in the Aseb area can have wind speeds that are higher than the wind speeds in the nearby coastal plains (Eritrean Department Of Energy (EDOE) 1997)

With regards to the extent of the high resource areas, simulations, ship-based meteorological measurements, station measurements and scaterometry data have provided different answers. The KLIMM meso-scale simulations forecast a very limited area of high wind resources centered around Aseb Airport that did not extend into the Red Sea, and which covered an area of less than 50 km radius. The ship-based measurements were largely limited to the main shipping lanes in the Red Sea, and did not resolve the details of the wind speeds near the Eritrean coast. But these measurements did indicate 10 m annual average wind speeds of up to 8 m $s^{-1}$ extending from 12.7 to 14$^0$N in the Red Sea (Rosen *et al.* 1999). Scatterometry measurements appear to indicate annual average wind speeds of slightly more than 6 m $s^{-1}$ from about 13 to 14$^0$N, but such measurements are known to be inaccurate near coastlines. Mean-while more recent meteorological ground station measurements have indicated 10 m annual average wind speeds of approximately 7 m $s^{-1}$ at 10 m along the coast at Gahro (12.8$^0$N) and Aseb Airport (13.064$^0$N), but an annual average wind speed of only 4.7 m

$s^{-1}$ at Idi (13.93$^0$N) and 4.5 m $s^{-1}$ at Tio (14.68$^0$N). It is currently unknown how much variability there might be in the wind speeds between the existing stations, or if there are some particular spots along the coast that have wind speeds higher than any of these stations. And finally, because there is no vertical profile measurements of wind speeds in the high wind portion of the Southern Red Sea, very little is known regarding the three dimensional structure of the LLJ and its dynamics with local sea breezes and coastal topography.

In this study, we use the RAMS in order to map specific wind energy resources in Southeastern Eritrea during a typical 4-day period during the high wind season. We find that RAMS reproduces well-know distinct features of the Eritrean wind meteorology much better than previous modeling efforts. We compare the results from RAMS with available surface data on winds and wind climatology. Given a good match between the model and available ground data, we use RAMS to produce wind speed maps for a typical high wind season day. Because annual wind power estimates are dominated by winds during the high wind season and because the winds during this period follow a consistent monsoonal pattern, we assume that the wind speed maps produced for a typical high wind period will correlate with annual wind power resources for the area.

With respect to our four Southeastern Eritrea wind resource questions: (1) Are the wind resources better on the hills or in the sea?; (2) How far do excellent wind resources extend?; (3) How does wind power depend on altitude?; And (4) Where are the highest performance wind energy generation sites? We propose the following hypotheses: (1) Because the source of the high wind is a LLJ over the Red Sea, the highest wind locations will be coastal protrusions or hills that are closest to the center of the LLJ. (2) Approximately 200 km of coastline from the Djibouti border north to Tio has very good wind resources except for bays and protected areas. (3) Vertical wind shear will be strongest near the coastline whereas further inland there will be a great variability of vertical wind shear due to topographic effects, and (4) the highest performance wind energy generation sites will be coastal hills near Aseb Airport and Gahro stations.

## 2) CASE SELECTION AND SYNOPTIC CONDITIONS

In performing the synoptic analysis, we use RAMS output because of the lack of official published maps of sufficient resolution for this area. The model is initialized and nudged with data from the NCEP large-scale model, and the illustrated maps should be largely consistent with the synoptic features of the NCEP data.

The simulation period for this study 8-12 February 2002 when the dynamics of the region are typically stable and consistent. The synoptic

patterns change very little during the four day period, and are characterized by the south-east monsoon at the surface and a stable high pressure system over the South Red Sea during much of the period at the 700 mb level (Flohn 1965). There is a steady southwesterly LLJ that is channeled and accelerated through the strait of Bab el Mendeb. The stable, stationary high pressure produces a strongly stratified marine layer over the Gulf of Aden and the Red Sea and a heat low over Western Eritrea and Eastern Sudan. The strongly stratified, relatively cool marine layer becomes a mass of air that is channeled and constrained as it travels from the Gulf of Aden to the Red Sea.

We illustrate synoptic conditions in Figs. 59 to 61. The synoptic pattern changed very little over the Aseb bay region during this simulation period. The upper-level flow (700 mb) fields were characterized by a steady, stable high pressure ridge which lingered over the Red Sea, Eritrea, and the Gulf of Aden, and then drifted to the southeast over Somalia and the Indian Ocean. Westerly flow persisted over the northern Red Sea and easterly flow was dominant over Ethiopia and Somalia. Mid-latitude westerlies of 5-25 m $s^{-1}$ extended from Sudan to Saudi Arabia to the north; while from Ethiopia to the Indian Ocean the equatorial easterlies can be seen in the southern part of the domain. The high-pressure ridge produced a very stable marine layer and a heat low over Eastern Eritrea

and Sudan. These features drove the planetary boundary layer mesoscale flows that created the Southern Red Sea LLJ.

At 0000 UTC 8 February 2002 (Fig. 59a), 700 mb, the winds were characterized by an anticyclonic flow centered at the southern Red Sea and covering north western Sudan, the northern Red Sea and South-western Arabia Peninsula. Winds over the Southern Red Sea and Eritrean landmass were weak and variable since the area was under the influence of an anticyclonic circulation bounded by the mid-latitude westerlies to the north and the equatorial easterlies to the south. The peak of the synoptic high pressure (5880 m) was located over the Yemeni plateau and Northeastern Sudan.

Two days later at 0000 UTC 10 February (Fig. 60a), almost the exact same synoptic pattern was seen; The high-pressure system had further strengthened to 5900 m, covering most part of the Red Sea and Gulf of Aden. The 700 mb winds showed a distinct anticyclone centered over the Southern Red Sea. The westerly winds had weakened to 5-15 m $s^{-1}$, and winds were northwesterly over Saudi Arabia, south to south-westerly over eastern Sudan, and easterly over Somalia and Ethiopia. Winds over the region south of $12^0$N did not change much in speed and direction.

Surface (1000 mb) maps were also examined for this period of simulation. At 0000 UTC 8 February 2002 (Fig. 61b), a synoptic high-

pressure system of 1018 mb developed over Saudi Arabia. There was also a heat low of 1005 mb over western Eritrea. This anticyclonic circulation of the Saudi Arabian high pushed marine air through the strait of Bab el Mandeb. At 0000 UTC 10 February 2002 (Fig. 62b), winds were generally flowing from the southeast all the Southern Red Sea with speeds ranging from 5-12.5 m $s^{-1}$, the maximum being at the exit of Bab el Mandeb. Western Eritrea was characterized by calm winds (1-2.5 m $s^{-1}$). The anticyclonic circulation around the eastern Sahara high (to the northwest of the illustrated domain) pushed Northern Red Sea winds from the north and produced a low-level convergence along the Northern Eritrean coast. From here, air is pulled inland through a break in the mountains at Port Sudan to Western Eritrea by the heat low in that region. (This flow pattern is analogous to the marine air that flows through the Carquinez Straight to the heat low in the San Joaquin Valley in California during stable synoptic high pressure conditions). This creates a pattern that is characteristic of the wintertime steady monsoon circulation pattern in the region (Flohn 1965).

*B. Methodology*

1). METHODOLOGY OVERVIEW

The RAMS model (version 4.4) has been used to perform a simulation of the wind patterns over a four-day period in February 2002 along the Southeastern Eritrean coast. The specific days were 8-12 February.

This period was chosen because February is within the high wind season of the Southern Red Sea region based on observational studies. The particular period was selected because it showed steady, consistent strong winds from the southeast that are typical for this period. The simulated winds and temperatures were validated by comparing with the observed values as reported above. The automatic stations at Aseb Airport and Gahro were used for the model validation. Finally, the simulation results were analyzed to find the best sites for producing clean and sustainable energy via wind production. Hypotheses regarding the potentially most productive wind energy sites are refined by examining the 3D structure of the wind fields, in addition to producing average wind speed maps for the period.

2). MODEL SETUP

Our RAMS simulations focused on an analysis of the coastal wind dynamics in order to locate the best sites for wind power generation along the southern coast of Eritrea. For this purpose, a nested-grid configuration of four grids was used in RAMS. The outer model domain was extended westward to include Eritrea, parts of Sudan, and Ethiopia. Meanwhile, on the eastern side of the domain, the Red Sea, parts of Saudi Arabia and Yemen were included (Fig. 63a). Finer nested grids were used to the area of interest in order to obtain meteorological fields of high resolution (Fig. 63b).

In order to select the most suitable nested grid configuration, several test simulations were performed. The configuration that has finally been selected and applied for the selected period of simulation is the following:

- Grid 1: A coarse grid with a mesh of 50x60 points and 40 km horizontal grid increment.
- Grid 2: A medium grid with a mesh 42x42 points and 10 km horizontal grid increment.
- Grid 3: A small grid with a mesh 62x50 points and 2.5 km horizontal grid increment.
- Grid 4: A fine grid with a mesh 42x42 points and 0.7 km horizontal grid increment

Grids one, two, and three were centred at the domain coordinate of 12.791$^0$N and 43.071$^0$E (Aseb city), while the centre of grid four was adjusted to Aseb Airport to include the hills near Aseb Airport. Concerning the vertical structure, the grids were identical. In detail, 50 vertical layers with a first grid spacing of 40 m and a grid stretch ratio of 1.12 have been used. The vertical structure was dense in the lower levels, and became increasingly coarse toward the top of the domain, which was at 30 km.

## 3). INITIALIZATION AND INPUT DATA

The data available for validating and calibrating meteorological simulations in Eritrea consist of ground station data, historical and current radiosonde data, satellite-based scatterometry data, and historical ship-based measurements in the Red Sea. Station data exists for 25 first and second-class stations recently installed by the Eritrean Department of Energy (Habtetsion *et al.* 2002). The best equipped of these stations measure temperature, wind, humidity, pressure, and solar radiation. Historical radiosonde data measurements exist for Asmara, Eritrea, and for nearby stations at Addis Abeba, Ethiopia and Khamis, Saudi Arabia. Recent radiosonde data exists for Abha and Jedda, Saudi Arabia (University of Wyoming web site). Historical ship-based measurements from the Red Sea are available from the Comprehensive Oceanographic and Atmospheric Data Set (COADS). In addition, satellite-based measurements of wind using radar scatterometry exist for the Red Sea and Gulf of Aden areas.

The NCEP data available at a frequency of once every six hours includes: temperature, pressure, wind speed, wind direction, and relative humidity data with a resolution of 2.5 x 2.5 degrees. The model was initialized at 0000 UTC 8 February 2002 with NCEP data and was allowed

to spin up for 12 hours to initialize the meteorological fields at smaller scales.

*C. Results*

1). MODEL VALIDATION

To have confidence in the model results, validation of model results against observations was carried out. To gain insight into how well the model simulation depicted the thermal forcing of the low-level flow, the model surface temperature and wind speed fields were compared to surface observations. For the time period simulated, there are detailed meteorological measurements for only two stations located in the higher resolutions grids three and four: Aseb and Gahro. Time series plots of surface temperature and wind speed for stations at Aseb Airport and Gahro were compared to model results and observations.

Differences between model results and observations can largely be explained by possible errors in near-surface extrapolation of model parameters due to local, subgrid characteristics of surface roughness. In our comparisons, we compared the time series model results of the 10 m wind speed at Aseb and Gahro, and 2 m temperature at the Aseb Airport station.

Figure 64 shows the comparison of the model and observational wind speed at Aseb Airport station. Without any surface roughness

adjustments to the extrapolation calculation, the model underestimated the daytime and nighttime wind speeds for almost all times of the simulation period. However, the daily pattern of wind speed variations matched observations quite well.

Given the systematic underestimation of wind speed, the surface roughness assumptions of the 10 m wind speed estimate were reexamined. The model used a total roughness length of 0.05 m in the Aseb area, which is a level desert (Fig. 65). A review of typical roughness lengths for level desert indicated that a roughness parameter adjustment for the 10 m estimate was needed given the local roughness characteristics of the meteorological station site. To make this adjustment, the log law was used and the roughness-length was set 0.0003 m for level desert (Jacobson 1999). The adjusted estimate of the 10 m wind speed vs. time was recalculated for Aseb Airport from the surface grid cell average wind speed and plotted in Fig. 66. The roughness-adjusted estimate of 10 m wind speed with the roughness adjustment of the extrapolation equation now shows a very good match with the observational data (Fig. 66).

For the Gahro station, similar discrepancies were observed between model results and the observations, but the adjustment in the 10 m wind speed estimate was made in a slightly different manner (Fig. 67). The meteorological station at Gahro is located less than 10 m from the water's edge at a location where the winds are onshore during the entire

simulation period. The model grid did not resolve these subgrid characteristics of the meteorological station site well. Thus the appropriate surface for the Gahro station is water, but at the model resolutions, RAMS shows Gahro to be on land. Thus, the model wind speeds used to compare with observations are those at the next grid cell east of Gahro, which has water surface characteristics in the model. The comparisons with the 10 m wind speed over water is shown in Fig. 68. The results now show a good agreement between the model and observational wind speeds.

Surface temperature comparisons of model and observations at Aseb Airport station were also carried out. The model calculates the average temperature of the surface grid cell, and uses a surface boundary layer equation to calculate the estimate of the 2 m temperature. Before any roughness adjustment was done to the equation that estimates 2 m temperatures from the grid cell average temperature, the model underestimated the surface temperature by an average of 2.5$^{o}$C (Fig. 69), during the daytime. After a roughness adjustment was made to the equation for estimating 2 m temperatures using the value of 0.0003 m appropriate for the level desert at Aseb Airport, the surface temperature matched very well with the observations at the Aseb Airport station (Fig. 70). Under conditions of lower surface roughness, there is lower vertical turbulent mixing at the surface layer, and thus a larger temperature

difference between near-surface temperatures and temperatures at higher altitudes. Therefore, given a lower surface roughness, and a fixed grid cell average temperature, a lower surface roughness will lead to a higher near-surface temperature estimate during the daytime. This is what is seen in our temperature adjustment.

2). ANALYSIS

Given the fact that the model reliably reproduces daily wind patterns and temperatures with appropriate computational adjustments, we are confident that the model also reproduces many of the physical and geographic features of the winds in the area.

Figure 71 shows a 10 m average wind speed map for the south coast of Eritrea for the simulation period generated from the RAMS model results. This map shows a zone of average wind speeds greater than 9 m $s^{-1}$ stretching from approximately 12.8 to 14.6$^0$N over the Red Sea. Coastal wind speeds reached 7-10 m $s^{-1}$ and inland wind speeds were 4-7 m $s^{-1}$. The 10 m average maximum wind speeds were observed to be 10 m $s^{-1}$ at the interior of the Red Sea; Aseb Airport and Gahro experienced 8-9 m $s^{-1}$ average, which is quite good wind speed for power generation. Figure 72 shows at a larger scale a similar wind speed map (covering 10 to 20$^0$N) based on scatterometry data for the peak wind-season month of February (http://www.punchdown.org/rvb/). Both

maps (Figs. 71 and 72) show a wind jet in the southern Red Sea between 12.5 and 15$^0$N, with peak 10 m winds of slightly over 10 m s$^{-1}$ at the latitude of 13.5$^0$N. Model results show more detail than can be resolved with the scatterometry data, but both are in good agreement with the main features of the wind speed distribution over the southern Red Sea. Assuming that the RAMS model provides a reasonably accurate physical description of the wind distribution, we now analyze the results in more detail below.

Higher resolution maps of the average wind speed distribution of the area (3 and 4) were analyzed to show more detailed wind speed structure of the region. Figures 73 and 74 show at higher resolution the wind speed distribution around Aseb and Gahro. There are stronger wind speeds (8-9 m s$^{-1}$) over the coast in general and weaker wind speeds inland, with the exception of the hills behind Aseb Airport. Here we see an interesting situation of increases in the average wind speed by 0.5-1 m s$^{-1}$ making the average wind speed on the hills to be 9.5-10 m s$^{-1}$. This is due to the elevation of the hills (about 300 m) matching to the level of the LLJ. It is believed that the wind speed on these hills could have been stronger, if the actual height of the hills had not been underestimated by the smoothed topography data set used by RMAS. The 20 m average wind speed plots for grids 2, 3 and 4 are shown in Figs. 75, 76 and 77, respectively. These plots show that the winds had

increased by 2-3 m $s^{-1}$ at the coast as well as inland regions compared to the 10 m wind speeds. The hills behind Aseb Airport also experienced a stronger wind speed of magnitude 11 m $s^{-1}$. The average wind speed plots for the above mentioned grids at 61 m, which could be the hub height of a wind turbine, are shown in Figs. 78, 79, and 80. As we compare the 20 m and the 61 m results we find that the locations with the greatest vertical shear are those near the edges or boundaries of the LLJ.

The "Eritrean Low-Level Jet" is a relatively narrow wind stream along the East African Red Sea Coast and is part of the larger Southeast Monsoon circulation pattern of the Southern Red Sea. A conceptual model of the LLJ that shows a horizontal slice across southern Red Sea is shown on Fig. 81. The LLJ is one of the strongest and most sustained low-level wind systems on the Red Sea coast. It is normally strongest in the period between November and March when core maximum speeds reach up to 20-30 m $s^{-1}$. The LLJ is modified by the diurnal sea/land breeze dynamics of the region. The core is usually centered at an elevation of about 400-600 m. This semi-permanent low-level wind, which is particularly strong during the Southeast Monsoon, is the key for the high wind speeds of the Eritrean southern coast.

To examine the structure of this LLJ over the Southern Red Sea, we examine wind speed cross-sections at Aseb Airport from the simulation. We select cross sections for midnight and noon UTC on the third

day of the simulation to illustrate the LLJ structure. During 0000 UTC 11 February 2002 (Fig. 82), the x-z cross-section of the velocity vectors and the vertical velocity contours are shown. The jet is centered at about 600 m with its core speed reaching 26 m $s^{-1}$. Down-slope winds from the Saudi Arabian side of the coast are flowing towards the jet. It has also closer proximity to the Eritrean coast and high wind speeds at upper levels are flowing as upslope winds along the Eritrean coastal mountain tops. During 0700 UTC 11 February 2002, (Fig. 83), the sea breeze had fully developed on both sides of the coast, resulting in subsidence of the marine layer air mass in the middle of the Red Sea. As a result, the jet has lowered to about 400 m, strengthening the Eritrean coastal wind speeds. The wind speeds ranged from 10-16 m $s^{-1}$ at the Eritrean side of the coast and more than 22 m $s^{-1}$ at the core of the LLJ.

In summary we have showed the Eritrean Southeastern coast has locations of very high wind speeds that indicate a feasible wind energy resource potential. Since our simulation was conducted over a relative short time span, it cannot provide a definitive answer to these questions. However, the simulation had revealed the three dimensional structure of the Southern Red Sea southeast monsoon low-level jet. These results imply a set of provisional answers to our four wind resource questions that are explained in detail in the summary and conclusion of this thesis.

## 5. Summary and Conclusion

*A. Monterey*

In this research, we investigated the structure of the Monterey Bay sea breeze and its corresponding return flow. Specifically we sought an answer as to why a return flow was not detected in the LASBEX 1987 Doppler LIDAR study (Banta *et. al.* 1993).

To answer this question, we simulated the Monterey Bay sea breeze using RAMS and analyzed the structure of the wind fields. We subtracted out the background synoptic flows and examined the residual wind fields that were induced by land/sea and topographic effects. Examination of these wind fields indicated where the return flows for the sea breeze existed.

The Monterey Bay sea breeze has return flows that are diverted to two major areas. The first set of return flows come from the Sierra Nevada Mountains. A portion of the Monterey Bay sea breeze flows over and through the coastal hills, across the San Joaquin valley and up the western slopes of the Sierra Nevada Mountains. As the air ascends off the western slopes of the Sierra Nevada's, it produces a deep, weak sea breeze return flow of 1-3 m $s^{-1}$ from 1 to 4 km in elevation.

The second set of flows are of diverted return flows come from the complex mountain/valley circulations in the coastal range. As the sea breeze flows inland, it is diverted up and down coastal valleys north and

south of Monterey, flows up coastal mountain slopes, and ascends off the top of the coastal hills producing weak, complex return flows above the coastal mountain range.

Thus in summary, Banta *et al.* (1993) did not see the Monterey Bay sea breeze circulation because it consisted of a weak, deep return flow of 1-3 m $s^{-1}$ in a layer from 1 to 4 km in elevation, that would have been extremely difficult to detect when there is a 5-10 m $s^{-1}$ synoptic background flow at that level. In addition, the Banta study was able to take measurements only over a limited area near Monterey, when the return flow structure is dispersed over a wide geographic area extending to the Sierra foothills.

*B. Eritrea*

In this study, we posed four questions regarding the wind energy resources of Southeastern Eritrea that we attempted to answer through the simulation of a typical high wind period during the Southern Red Sea southeastern monsoon season:

(1) Are the wind resources better on the hills right on the coast?

(2) How far inland do excellent wind resources extend?

(3) How does wind power depend on altitude?

(4) Where are the highest performance wind energy generation sites?

Since our simulation was conducted over a relative short time span, it cannot provide a definitive answer to these questions. But the

simulation has revealed the three dimensional structure of the Southern Red Sea southeast monsoon low-level jet. These results imply a set of provisional answers to our four wind resource questions:

• **Hills or Coastline**: The best wind resources are in the center of the Southern Red Sea (SSR) LLJ at an elevation of 300 to 600 m above the eastern side of the Southern Red Sea along the Eritrean coastline. Those topographic features that can potrude closest to the center of this LLJ will be the locations with the best wind energy resources

• **Extent of Resources**: The SRS LLJ extends more than 200 km from Bab el Mandeb (at 12.5$^0$N) to 14.5 $^0$N in the Southern Red Sea.

• **Vertical Wind Shear**: Vertical wind shear is strongest near the coast in the afternoon, and also over coastal hills and mountains when the core of the SRS LLJ is closest to the land or sea surface.

• **Best Wind Resources Location**: There appear to be two maxima in the wind speeds in the SRS LLJ during the southeastern monsoon. One peak is near the Bay of Beylul and extends southwest toward a group of hills west of Aseb that rise to 900 m in elevation. The second peak in coastal wind speeds appear to be along an area of coastline approximately 30-50 km ESE of the Eritrean town of Idi. Both of these locations have not yet had their wind speeds measured with a meteorological station.

RAMS appears to have successfully simulated the main characteristics of the distribution of wind energy resources for Southeastern Eritrea. Further research will test these simulation results against new meteorological measurements to determine if the characteristics and distribution of wind speeds and wind energy resources have been accurately forecast by this study.

In this research paper, it was shown that the regional mesoscale model RAMS had proven useful to model the important dynamics of the complex coastal environment of the Southern coast of Eritrea. This region is capable of harvesting clean and environmentally sustainable wind energy. Specially, the hills behind Aseb Airport could be good candidates for a wind turbine project because of their location and proximity to the LLJ. This research has contributed directly to an on going $4 million wind energy project development being undertaken by the Eritrean Government in partnership with the UNDP/GEF.

Future research should also model the wind resources in the highlands of Eritrea. The complexity of the topography and solar heating dynamics of the highlands will make the modeling study difficult. There could be a number of good wind energy potential sites in these highlands. Due to the proximity to electrical grids, these sites can help supply the main national grid, along with helping in implementation of small-scale village electrification projects.

## REFERENCES


Arritt, R. W., 1993: Effects of the large-scale flow on characteristics features of the sea breeze. *J. Appl. Meteor.*, **32**, 116-125.

Atkinson, B. W., 1981: *Mesoscale Atmospheric Circulations.* Academic Press, New York City, 495 pp.

Banta, R. M., 1995: Sea breezes shallow and deep on the California coast. *Mon. Wea. Rev.*, 3, 3614-3622.

Banta, R. M., L. D. Olivier, and D. H. Levinson, 1993: Evolution of the Monterey Bay sea-breeze layer as observed by pulsed Doppler lidar. *J. Atmos. Sci.*, **50**, 3959–3982.

Banta, R. M., 1986: Daytime Boundary Layer Evolution over Mountainous Terrain. Part II: Numerical Studies of Upslope Flow Duration. *Mon. Wea. Rev.*, **114**, 1112–1130.

Bridger, A. F. C., W. C. Brick, and P. F. Lester, 1993: The structure of the marine inversion layer of the central California coast: Mesoscale conditions. *Mon. Wea. Rev.*, **121**, 335-351.

Burk, S. and W. Thompson, 1996: The summertime low-level jet and marine boundary layer structure along the California coast. *J. Atmos. Sci.*, **50**, 3959-3982.

Cai, X.M., and Steyn, D.G., 1999: Modeling study of sea breezes in a complex coastal environment. *Atmos. Environ.*, **34**, 2873-2885.

Chiba, O., F. Kobayashi, G. N. Schroder, and K. Sassa, 1998: Helicopter Observations of the Sea Breeze over a Coastal Area. *J. Appl. Meteor*, **38**, 573-587.

Clark, T. L. 1977: A small-scale dynamic model using a terrain-following coordinate transformation. *J. comput. Phys.*, 24, 186-215.

Darby, L. S. R. M. Banta and R. A. Pielke, 2002: Comparisons between mesoscale model terrain sensitivity studies and doppler lidar measurements of the sea breeze at Monterey Bay. *Mon. Wea. Rev.*, **130**, 2814-2836.

EDOE, 2000: Eritrean Department of Energy Report, Ministry of Energy and Mines, 200 pp.

EDOE, 1997: Eritrean Department of Energy Report, Ministry of Energy and Mines, 200 pp.

Flohn, H., 1965: Studies on the Meteorology of the tropical Africa. *Bonner meteorol. Abhandlugen.*, **5**, 2-35.

Foster, M. D., 1996: California sea breeze structure and its relation to the synoptic scale, Ph.D. dissertation, Meteorology Department, Naval postgraduate school, Monterey, California.

Gal-Chen, T., and R. C. J. Somerville, 1975: On the use of a coordinate transformation for the solution of the Navier-Stokes equations. *J. Comput, Phys.*, **17**, 209-228.

Garbesi, K., Kello, K. Rosen, and R. Van Buskirk, 1996: Preliminary wind energy resources assement for Eritrea. DOE (Department of Energy), Asmara, Eritrea *Phys.*, **17**, 209-228.

Habtetsion, S., D. Ghebrehiwot, R. Van Buskirk, and B. Lebassi, 2002: The potential of wind energy applications in Eritrea. *World Renewable Energy Congress VII*, Cologne, Germany.

Helfand, H.M., and J.C. Labraga, 1988: Design of a nonsingular level 2.5 closure model for the prediction of atmospheric turbulence. *J. Atmos. Sci.*, **45**, 113-132.

Hill, G.E., 1974: Factors controlling the size and spacing of cumulus clouds and revealed by numerical experiments. *J. Atmos. Sci.*, **31**, 646.

Jacobson, M. Z., 1999: *Fundamentals of Atmospheric Modeling.* Cambridge University Press, 672 pp.

Johnson, A. Jr., and J. J. O'Brien, 1973: A study of an Oregon sea breeze event. *J. Appl. Meteor.*, **12**, 1267-1283.

Knapp, M. C., 1994: Synoptic-scale influence of the Monterey Bay sea breeze, Master's thesis, Meteorology Department, Naval post graduate school, Monterey, California.

Lehremeyer, 2000: Lehremeyer international report, EDOE copy.

Lilly, D.K., 1962: On the numerical simulation of buoyant convection. *Tellus*, **2**, 148-172.

Mahrer, Y., and R. A. Pielke, 1977: The effect of topography on sea and land breezes in a two dimensional numerical model. *Mon. Wea. Rev.*, **105**, 115–1162.

McNider, R. T., A. P. Mizzi, and R. A. Pielke, 1982: Numerical investigation of low-level jets in coastal zones, Preprints, *First Int. Conf. on Meteorology and Air-Sea Interaction of the Coastal Zone.* The Hague, the Netherlands, *Amer. Meteor. Soc.*, 190-195.

Mesinger, F., and A. Arakawa, 1976: Numerical methods used in atmospheric models. GARP Publication Series, No. 14, WMO/ICSU Joint Organizing committee, 64 pp.

Mellor, G., and T. Yamada, 1974: A hierarchy of turbulence closure models for planetary boundary layer. *J. Atmos. Sci.*, **31**, 1791-1808.

Mulugetta, Y., and F. Drake, 1996: Assessment of the solar and wind energy resources in Ethiopia. Journal of Wind Energy, *Solar Energy* **57**, 323-44.

Pallabazzer, R., and A. Gabow, 1991: Wind resources in Somalia. *Solar Energy*, **46**, 313-32.

Pielke, R. A., 1984: *Mesoscale Meteorological Modeling.* Academic Press, San Diego, California, 612 pp.

Pielke, R. A., 2002: *Mesoscale Meteorological Modeling.* Academic Press, San Diego, California, 676 pp.

Pielke, R. A., and W. R. Cotton, 1977: A Mesoscale Analysis over South Florida for a High Rainfall Event. *Mon. Wea. Rev.*, **105**, 343–362.

Pielke, R. A., 1974: A three-dimensional numerical model of the sea breeze over south Florida. *Mon. Wea. Rev.*, **102**, 115–139.

Rosen, K., R. Van Buskirk, and K. Garbesi, 1999: Wind energy potential of coastal Eritrea, Analysis of sparse wind data. *Solar energy*, **66**, 201-214.

Rosen, Karen, (1998), An Assessment of the Potential for Utility-Scale Wind Power Generation in Eritrea, Master's Thesis, Environmental Studies, San Jose State University, California.

Round, R. D., 1993: Climatology and Analysis of the Monterey Bay sea breeze. Master's thesis, Meteorology Department, Naval postgraduate school, Monterey, Califonia.

Simpson, J. E., 1994: *Sea Breeze and Local Winds*. Cambridge University Press, 243 pp.

Smagorinsky, J., 1963: General circulation experiment with the primitive equations. Part I, The basic experiment. *Mon. Wea. Rev.*, **91**, 99-164.

Steyn, D. G., and I. G. Mckendry, 1988: Qualitative and quantitative evaluation of a three-dimensional mesoscale numerical model simulation of a sea breeze in complex terrain. *Mon. Wea. Rev.*, **16**, 1914–1926.

SWECO, 2002: Swidish Consultant Company Inc. report EDOE copy.

Tijm, A. B. C., A. A. M. Holtslag, and A. J. Van Delden, 1998: Observations and Modeling of the sea breeze with the return current. *Wea. Rev.*, **127**, 625–640.

Tremback, C. J., J. Powell, W. R. Cotton, and R. A. Pielke, 1987: The forward in time upstream advection scheme: Extension to higher orders. *Mon. Wea. Rev.*, **115**, 540-555.

Tripoli, G. J., and W. R. Cotton, 1982: The Colorado State University three-dimentional cloud/mesoscale model – 1982. Part I: General theoretical framework and sensitivity experiments. *J. de Rech. Atmos.*, **16**, 185-220.

University of Wyoming web site: http://weather.uwyo.edu/

Van Buskirk, R., web site: http://www.punchdown.org/rvb/

Van Buskirk, R., K. Garbesi, and K. Rosen, 1997: Wind resource assessment of Eritrea, Africa.

Van Buskirk, R., Garbesi, K., and Rosen, K., 1998: Wind Resource Assessment of Eritrea, Africa: Preliminary Results and Status, Journal of Wind Energineering and Industrial Aerodynamics, Vol. 74-76, P. 365.

Walko, R. L., and C.J Tremback, 2001: RAMS technical description. http://www.atmet.com/html/docs/rams/rams_techman.pdf.

Wexler, R., 1946: Theory and observations of the land sea breezes. *Bull. Amer. Meteor. Soc.*, **27**, 272-286

Zhong, S., and E. S. Takle, 1993: The Effects of Large-Scale Winds on the Sea/Land Breeze Circulations in an Area of Complex Coastal Heating. *J. Appl. Meteor.*, **32**, 1181-1195.

# Appendix A. RAMS primitive equations

a) Motion

$$\frac{\partial u}{\partial t} = -u\frac{\partial u}{\partial x} - v\frac{\partial u}{\partial y} - w\frac{\partial u}{\partial z} - \theta\frac{\partial \pi'}{\partial x} - fv + \frac{\partial}{\partial x}\left(K_m\frac{\partial u}{\partial x}\right) + \frac{\partial}{\partial y}\left(K_m\frac{\partial u}{\partial y}\right) + \frac{\partial}{\partial z}\left(K_m\frac{\partial u}{\partial z}\right) \quad (1)$$

$$\frac{\partial v}{\partial t} = -u\frac{\partial v}{\partial x} - v\frac{\partial v}{\partial y} - w\frac{\partial v}{\partial z} - \theta\frac{\partial \pi'}{\partial y} - fu + \frac{\partial}{\partial x}\left(K_m\frac{\partial v}{\partial x}\right) + \frac{\partial}{\partial y}\left(K_m\frac{\partial v}{\partial y}\right) + \frac{\partial}{\partial z}\left(K_m\frac{\partial v}{\partial z}\right) \quad (2)$$

$$\frac{\partial w}{\partial t} = -u\frac{\partial w}{\partial x} - v\frac{\partial w}{\partial y} - w\frac{\partial w}{\partial z} - \theta\frac{\partial \pi'}{\partial z} - \frac{\theta'_v g}{\theta_0} + \frac{\partial}{\partial x}\left(K_m\frac{\partial w}{\partial x}\right) + \frac{\partial}{\partial y}\left(K_m\frac{\partial w}{\partial y}\right) + \frac{\partial}{\partial z}\left(K_m\frac{\partial w}{\partial z}\right) \quad (3)$$

b) Thermodynamics

$$\frac{\partial \theta_{il}}{\partial t} = -u\frac{\partial \theta_{il}}{\partial x} - v\frac{\partial \theta_{il}}{\partial y} - w\frac{\partial \theta_{il}}{\partial z} + \frac{\partial}{\partial x}\left(K_h\frac{\partial \theta_{il}}{\partial x}\right) + \frac{\partial}{\partial y}\left(K_h\frac{\partial \theta_{il}}{\partial y}\right) + \frac{\partial}{\partial z}\left(K_h\frac{\partial \theta_{il}}{\partial z}\right) + \left(\frac{\partial \theta_{il}}{\partial t}\right)_R \quad (4)$$

c) Water species

$$\frac{\partial r_n}{\partial t} = -u\frac{\partial r_n}{\partial x} - v\frac{\partial r_n}{\partial y} - w\frac{\partial r_n}{\partial z} + \frac{\partial}{\partial x}\left(K_h\frac{\partial r_n}{\partial x}\right) + \frac{\partial}{\partial y}\left(K_h\frac{\partial r_n}{\partial y}\right) + \frac{\partial}{\partial z}\left(K_h\frac{\partial r_n}{\partial z}\right) + \left(\frac{\partial r_n}{\partial t}\right)_{SS} \quad (5)$$

d) Mass continuity

$$\frac{\partial \pi'}{\partial t} = -\frac{R\pi_0}{c_v\rho_0\theta_0}\left(\frac{\partial \rho_0\theta_0 u}{\partial x} - v\frac{\partial \rho_0\theta_0 v}{\partial y} - w\frac{\partial \rho_0\theta_0 w}{\partial z}\right) \quad (6)$$

e) Ideal Gas

$$\overline{p} = \overline{\rho}\, R_d\, \overline{T}_v \quad (7)$$

f) Poisson

$$\overline{\theta} = \overline{T}_v\,(1000/p)^{R_d/c_p} \quad (8)$$

## Appendix B. Acronyms

| | |
|---|---|
| 2D | Two Dimensional coordinates |
| 3D | Three dimensional coordinates |
| 4DDA | Four Dimensional Data Assimilation |
| AGL | Above ground level |
| ASL | Above sea level |
| AVHRR | Advanced Very High Resolution Radiometer |
| COADS | Comprehensive Oceanographic and Atmospheric Data Set |
| DEM | Digital elevation model |
| DOE | Department of Energy |
| ERTC | Energy research and training center |
| ETA | Eta ($\eta$) model |
| GEF | Global Environment Facility |
| KLIMM | KLIma Model Mainz (Climatic model Mainz) |
| LASBEX | Land Sea Breeze Experiment |
| LLJ | Low-Level Jet |
| LST | Local Standard Time |
| MPBL | Marine Planetary Boundary Layer |
| NCEP | National center for environmental program |
| NOCD | Oceanography Command Detachment |
| PBL | Planetary Boundary Layer |

| | |
|---|---|
| RAMS | Regional atmospheric simulation system |
| RMS | Root mean Square |
| SBMV | Sea breeze mountain-valley circulation |
| SMHI | Swedish Meteorological hydrological institute |
| SST | Sea Surface Temperature |
| SWECO | Swedish Consulting company Inc. |
| TKE | Turbulent Kinetic Energy |
| UNDP | United Nations Development Program |
| USGS | United States Geological Survey |
| WAsP | Wind atlas analysis and application program |

## Appendix C. List of symbols

| | |
|---|---|
| $\theta_{il}$ | Ice-liquid water potential temperature (k) |
| $\theta_v$ | Virtual temperature (k) |
| $\pi$ | Total Exner function (mb) |
| $\pi'$ | Perturbation Exner function (m) |
| $\rho$ | Density (kg $m^{-3}$) |
| $c_p$ | Specific heat capacity at constant pressure (1004 cal/g k) |
| f | Coriolis parameter |
| g | Gravity (m $s^{-2}$) |
| $K_{e, h, m}$ | Eddy diffusivity for turbulent kinetic energy, heat and momentum ($m^2$ $s^{-2}$) |
| P | Pressure (mb) |
| $r_n$ | Water mixing ratio species of total water, rain, pristine, crystals, Aggregates, and snow. |
| u | East -west wind component (m $s^{-1}$) |
| v | North -South wind component (m $s^{-1}$) |
| w | vertical wind component (m $s^{-1}$) |
| $( )_0$ | Basic state quantity |
| $( )_R$ | Diabatic heating |
| $( )_S$ | Micro-physics source/sink |
| $( )'$ | Perturbation from basic state |
| $( )''$ | Sub-grid scale perturbation |
| $(\tilde{})$ | Transformed coordinates |
| $(\bar{})$ | Mean quantities |

Appendix D. Comparison table

**Table 1.** Comparison of the two research cases at the Coast of California and Southern coast of Eritrea

| No. | Case Feature | Case 1 | Case 2 |
|---|---|---|---|
| 1 | Study Location | Monterey, California | Southeast Eritrea |
| 2 | Study Question: Where is ___? | Return Flow | High wind resource |
| 3 | Which coast | West | East |
| 4 | Coastal orientation | NW/SE | NW/SE |
| 5 | Direction of marine layer jet | NW | SE |
| 6 | Height of coastal hills | 500-1500 m | 700-2000 m |
| 7 | Latitude | $36^0$ N | $13^0$ N |
| 8 | Other mountain ranges | Sierras, 4000m | Ethiopian highlands 4000 m, Yemeni Highlands 3000 m |
| 9 | Season Studied | Dry season | Dry season |
| 10 | SST | $15^0$C | $25^0$C |
| 11 | Study Site Exposure | Protected bay | Exposed hills |

# Appendix E. Figures

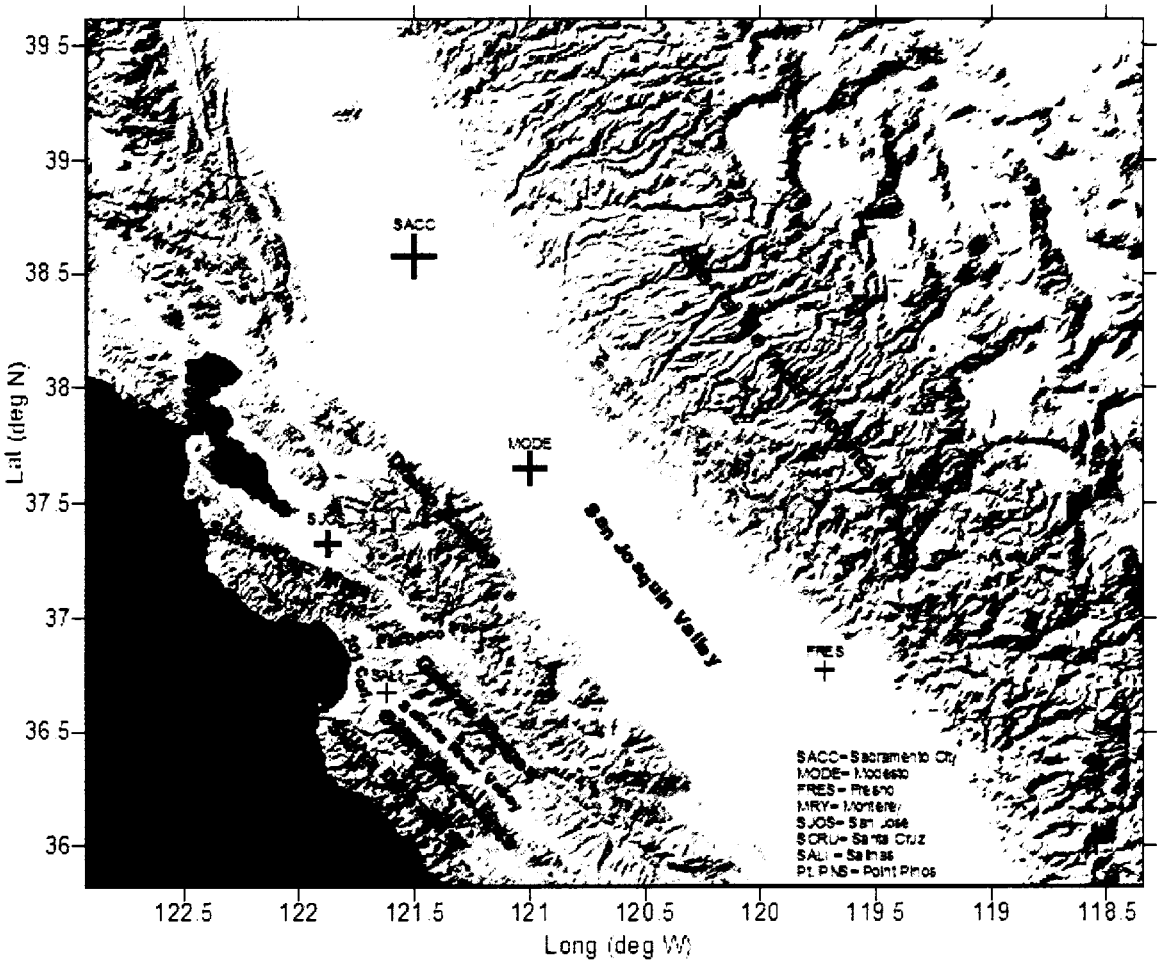


**Fig. 1.** Topographic map of central California (+ station locations).

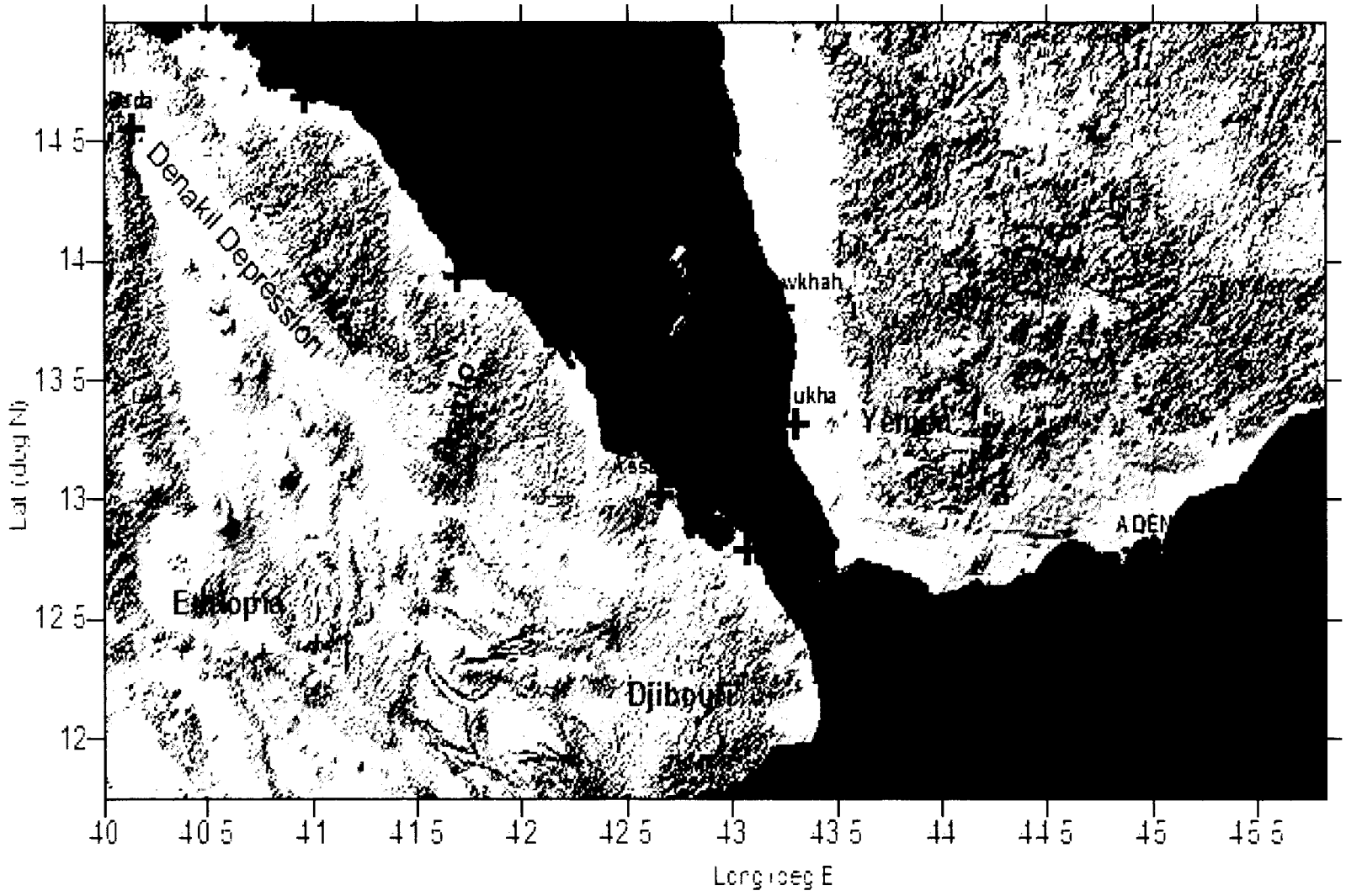


**Fig. 2.** Topographic map of the Eritrean southern Red Sea coast (+ is station location).

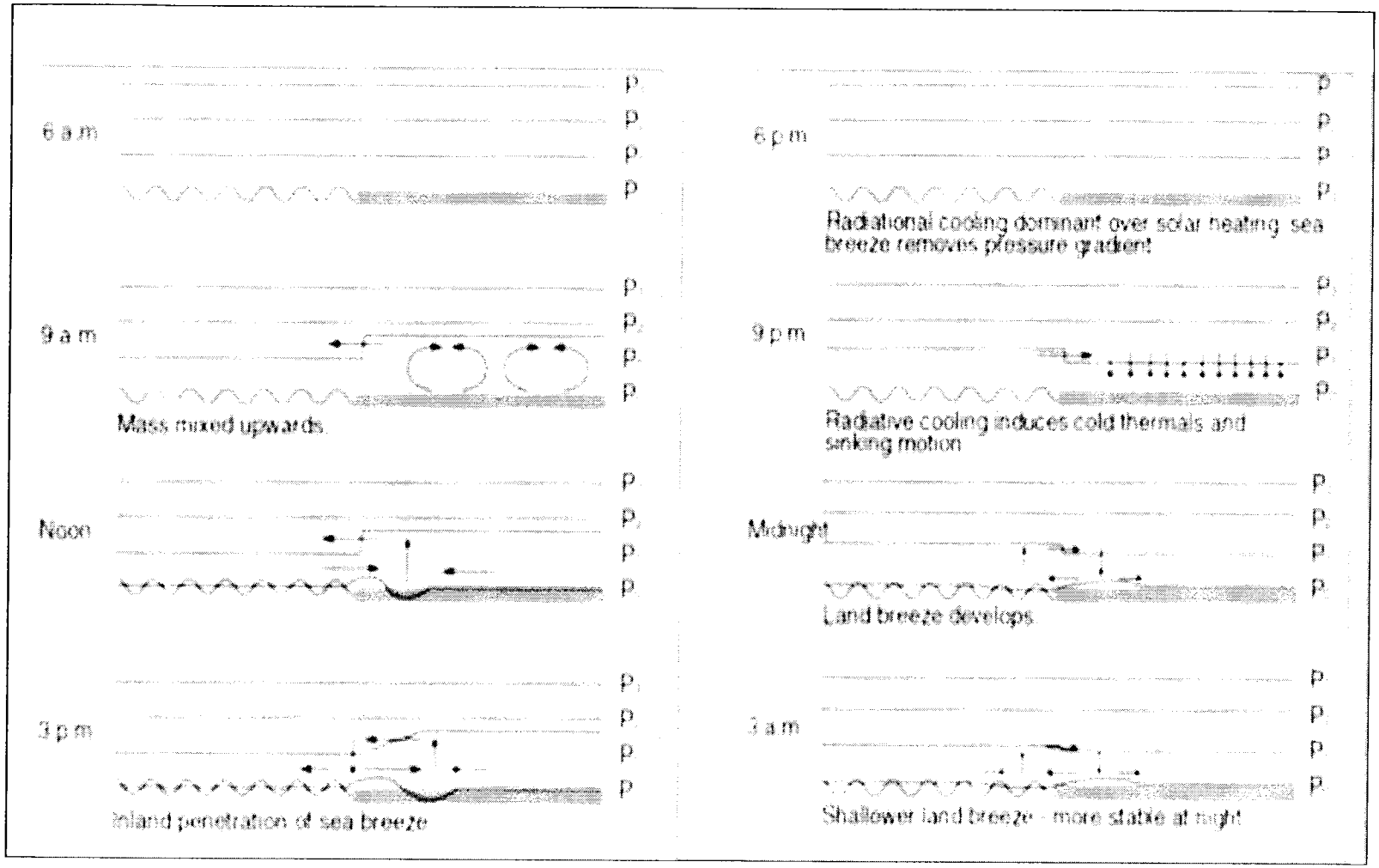


**Fig. 3.** Schematic of the diurnal evolution of the sea and land breeze in the absence of synoptic-flow (From Pielke1981).

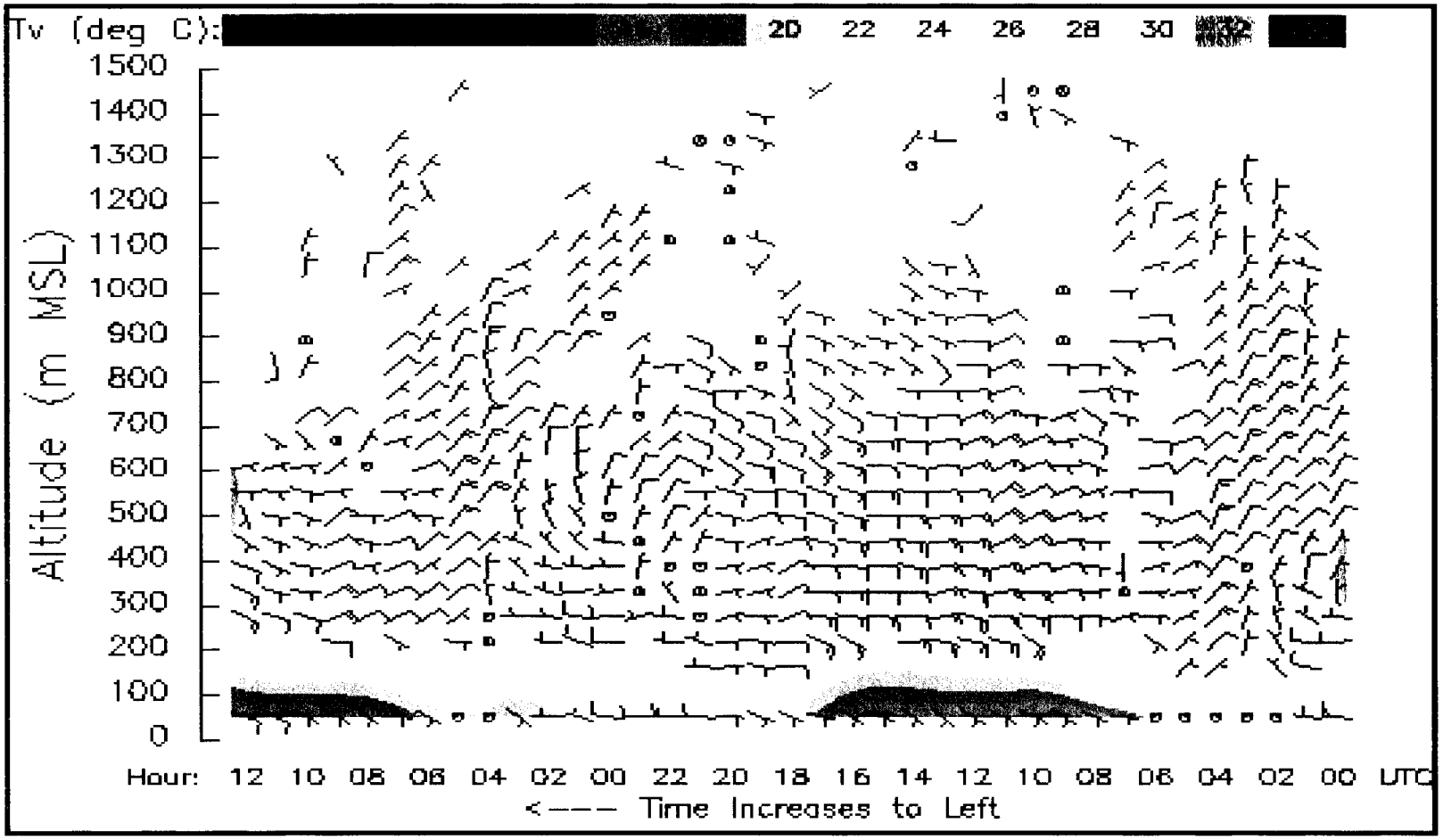


**Fig. 4.** Vertical wind profile ($ms^{-1}$) and virtual temperature ($T_v$ in $^0C$) at Moterey bay, Fort Ord profiler station for 26 October 2003.

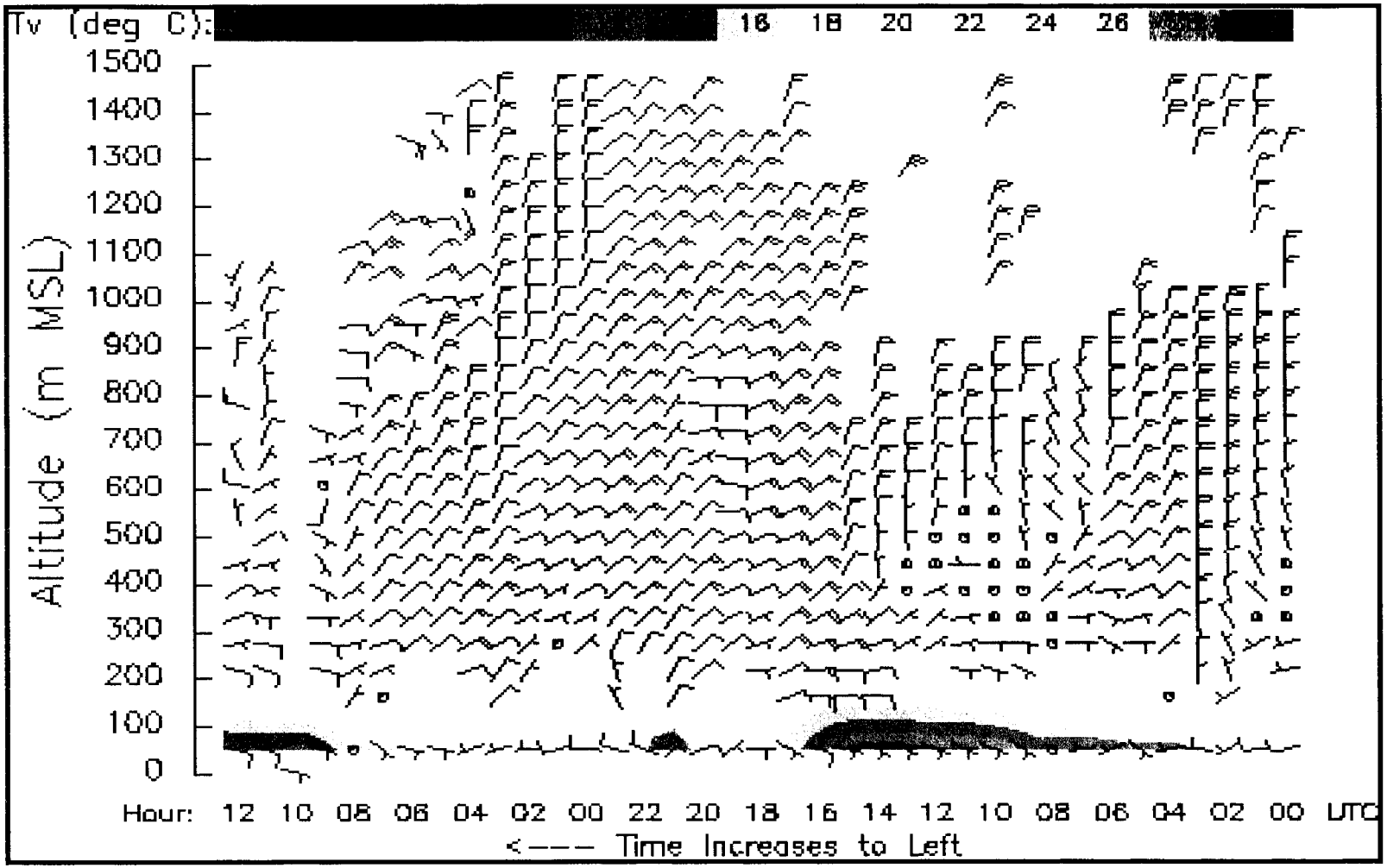


**Fig. 5.** Vertical wind profile ($ms^{-1}$) and virtual temperature ($T_v$ in $^0C$) at Moterey bay, Fort Ord profiler station for 16 March 2004.

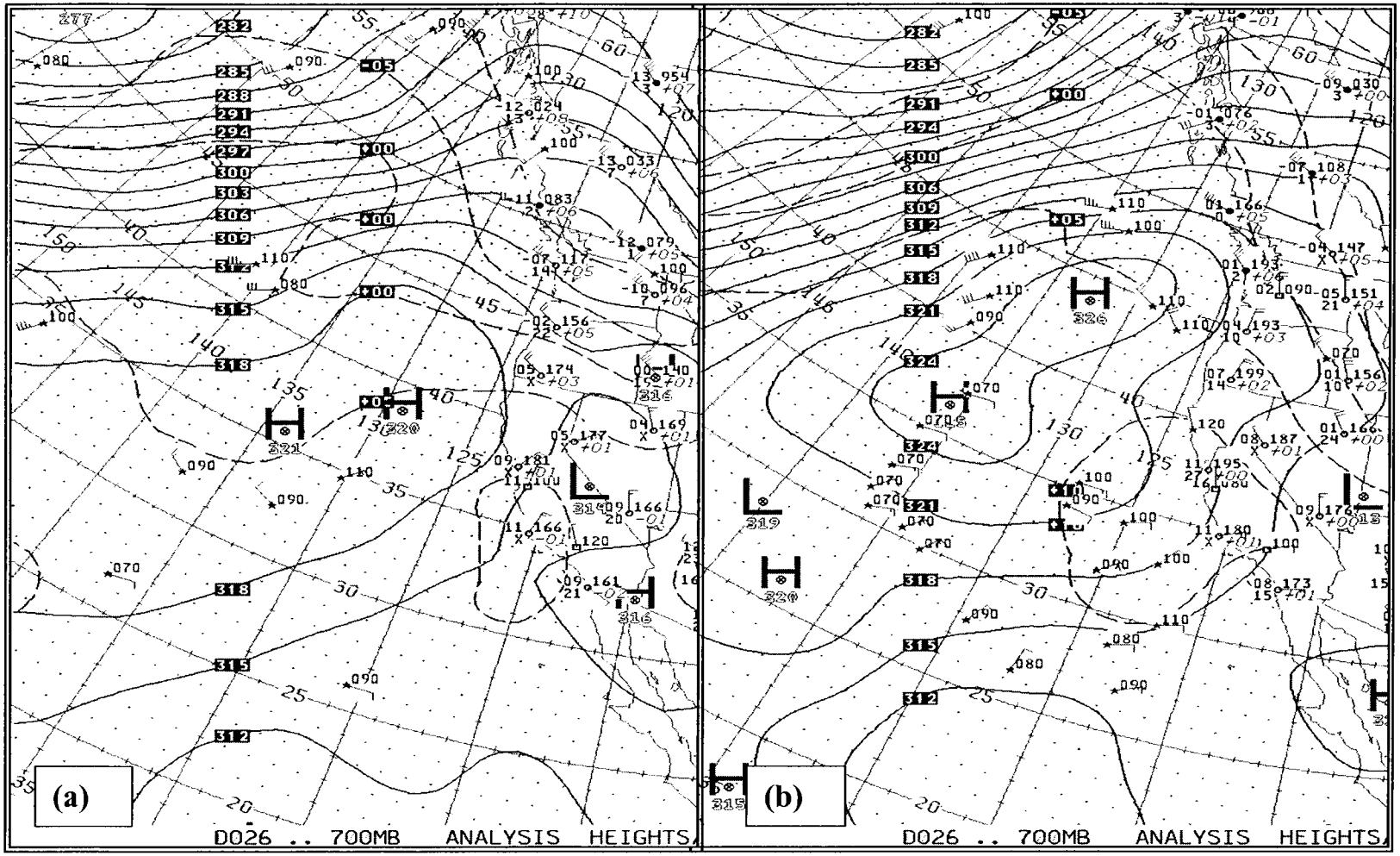


**Fig. 6.** 700 mb analysis heights/temperature valid 0000 UTC for strong offshore case (a) 24 October 2003 and (b) 25 October 2003 (wind speed in knots and temperature in $^{o}$C).

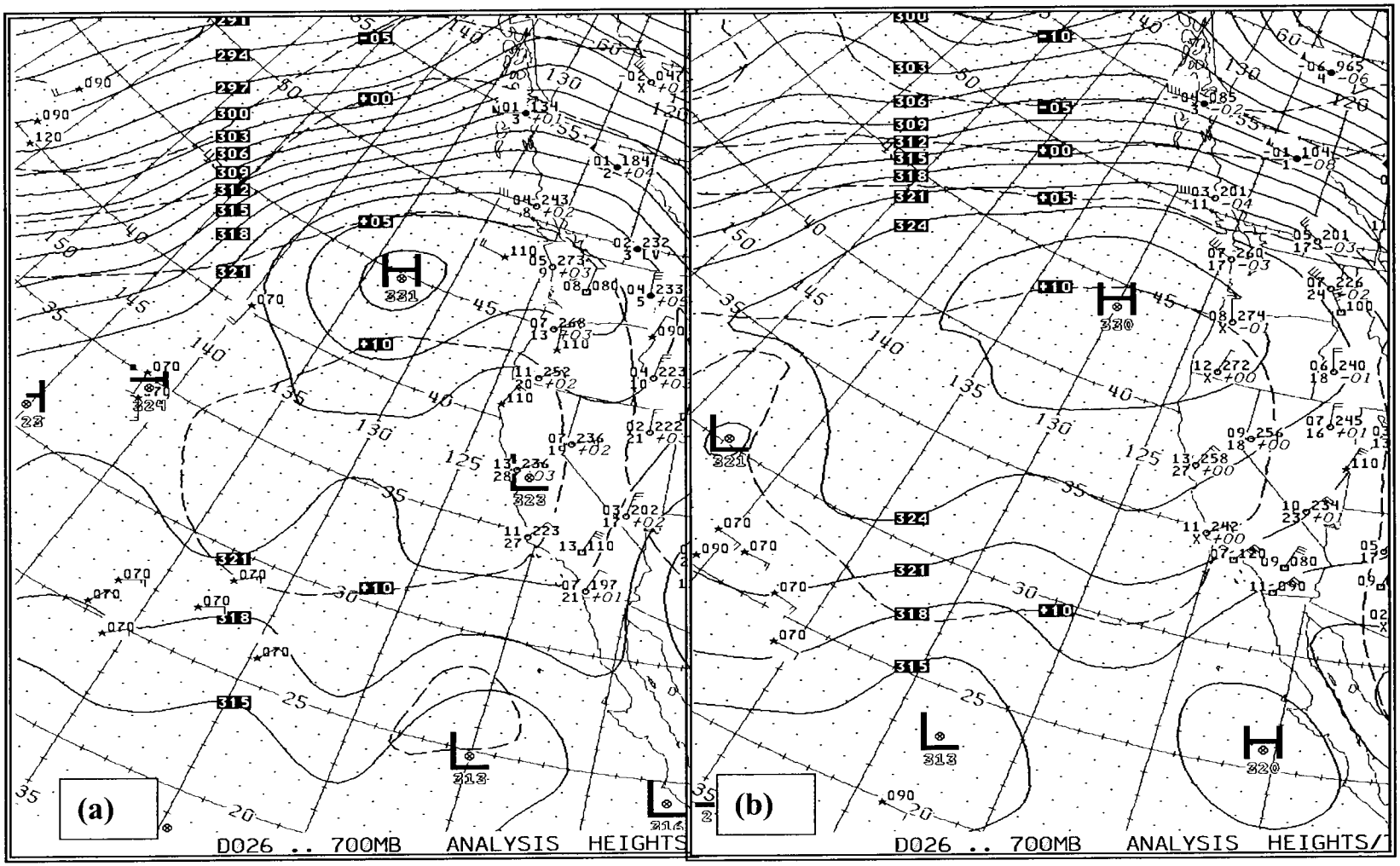


**Fig. 7.** 700 mb analysis heights/temperature valid 0000 UTC for strong offshore case (a) 26 October 2003 and (b) 27 October 2003 (wind speed in knots and temperature in ºC).

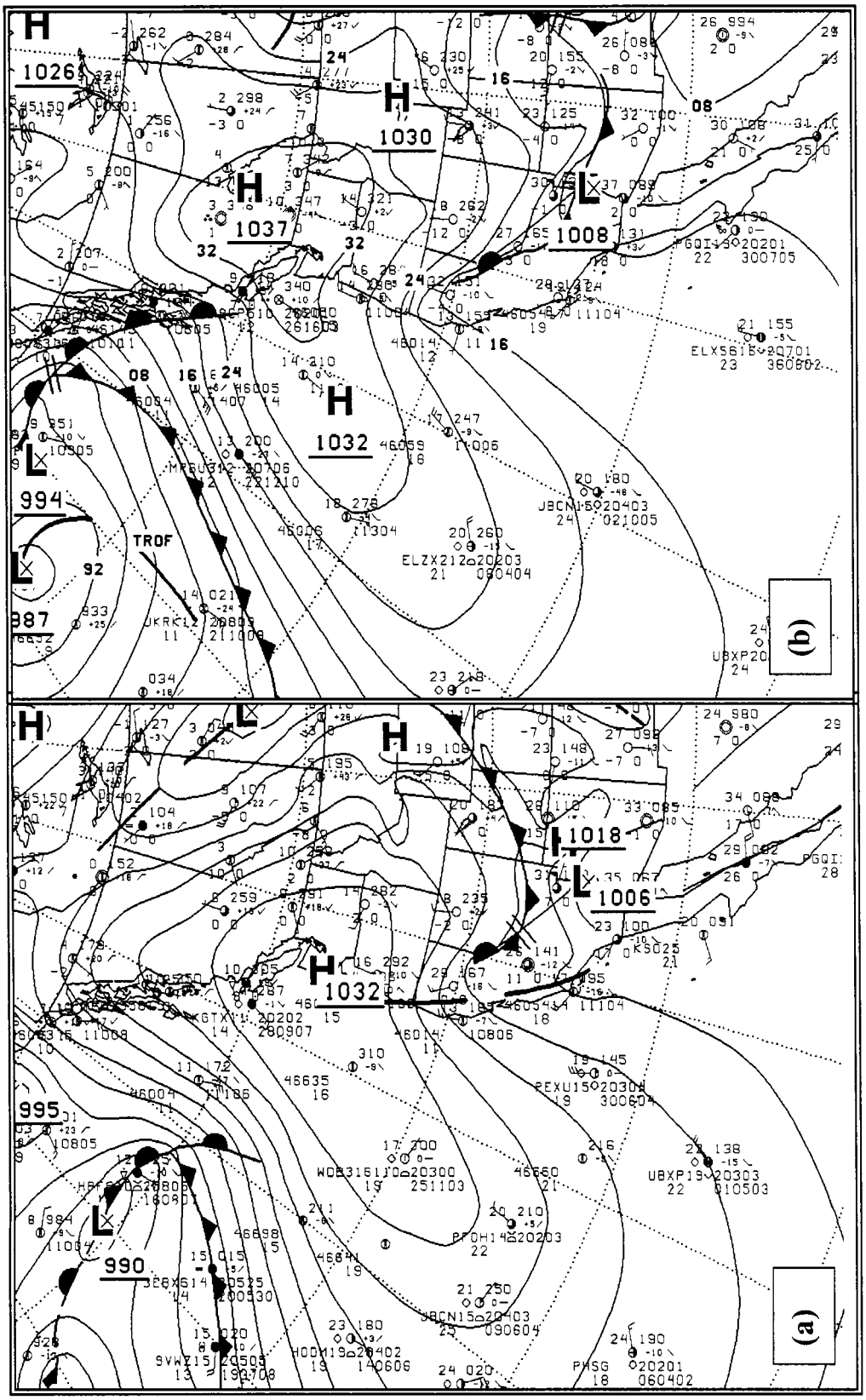


**Fig. 8.** Surface analysis heights/temperature valid 0000 UTC for strong offshore case (a) 24 October 2003 and (b) 25 October 2003 (wind speed in knots and temperature in ºC).

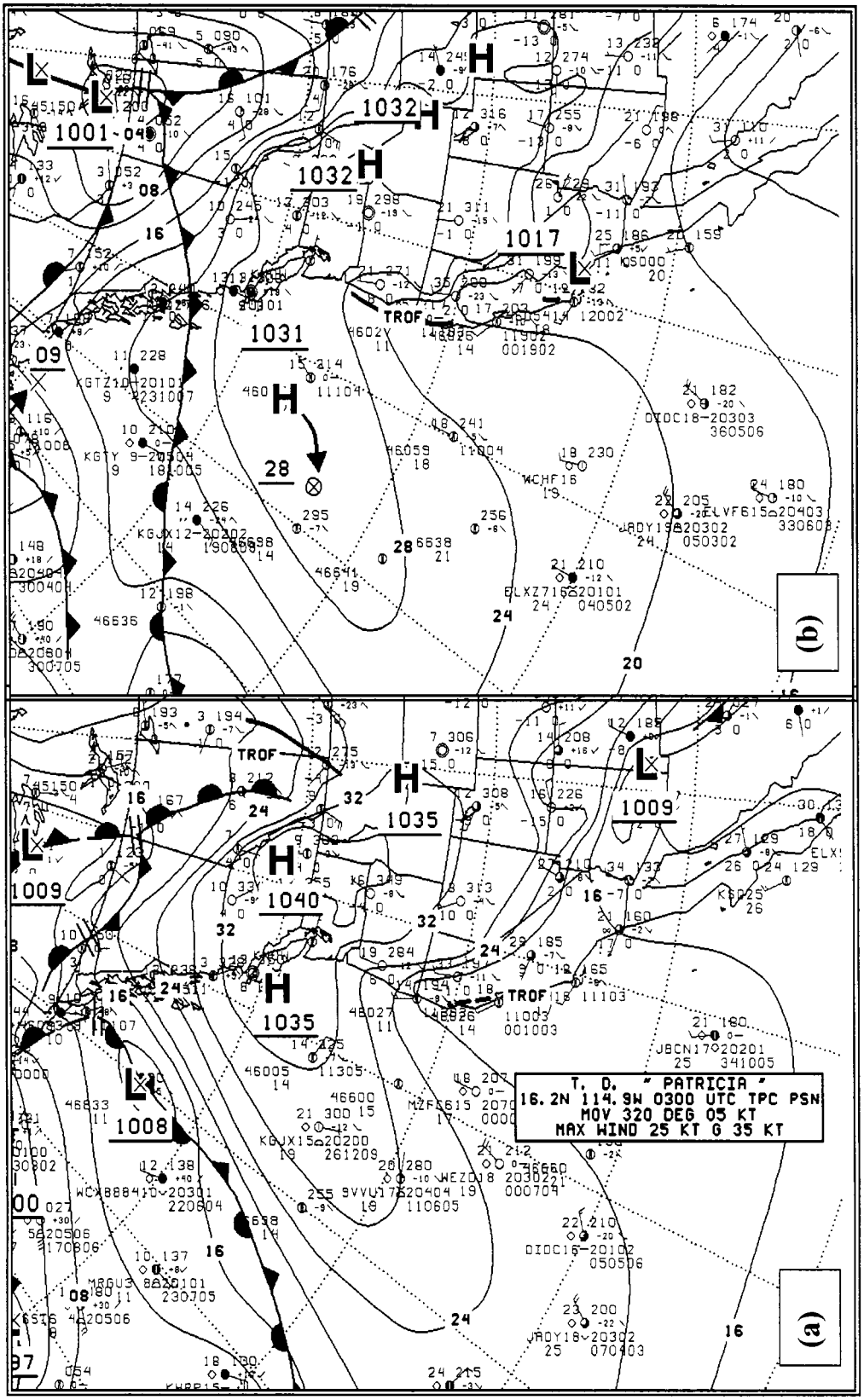


**Fig. 9.** Surface analysis heights/temperature valid 0000 UTC for strong offshore case (a) 26 October 2003 and (b) 27 October 2003 (wind speed in knots and temperature in ºC).

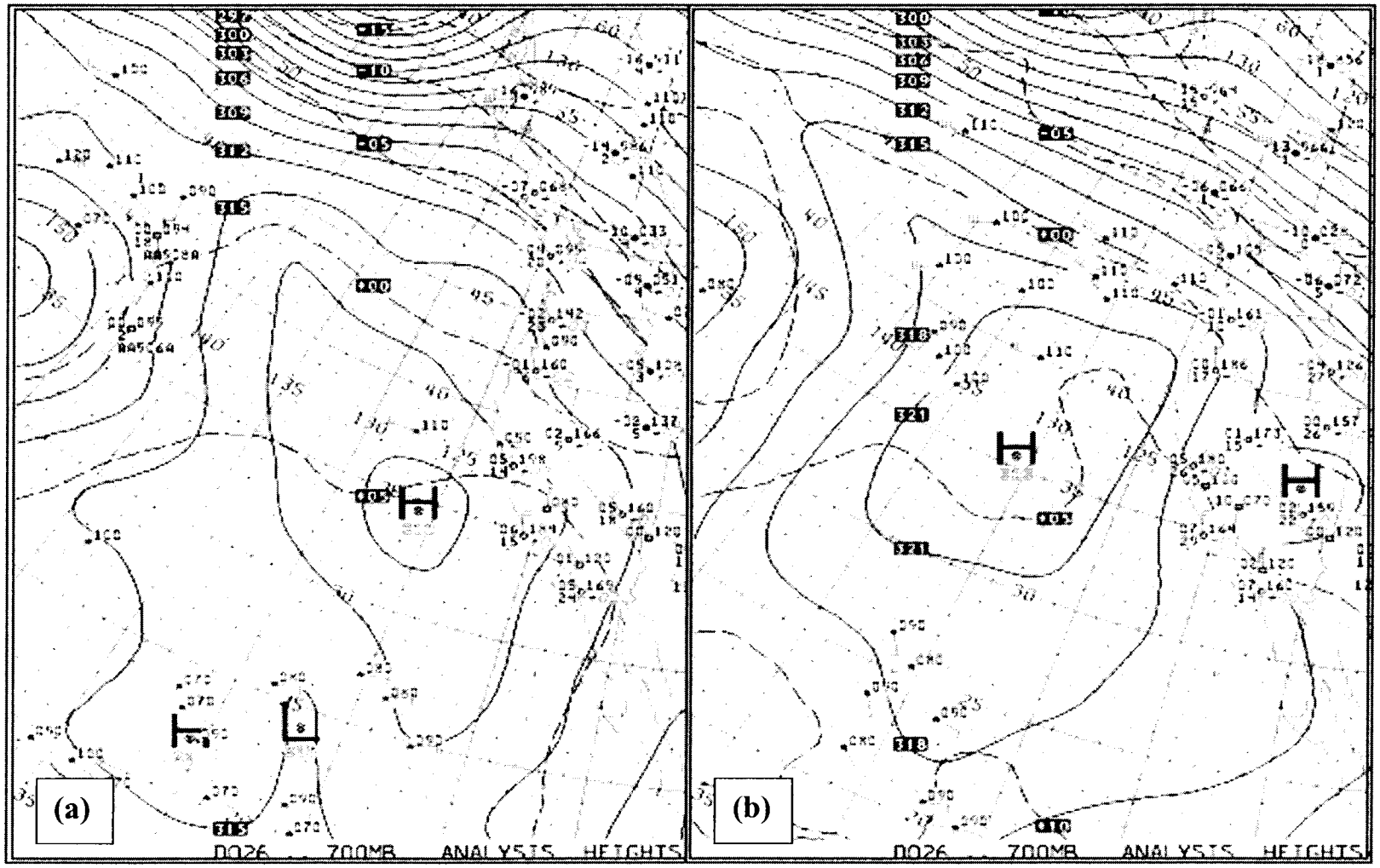


**Fig. 10.** 700 mb analysis heights/temperature valid 0000 UTC for weak offshore case (a) 15 March 2004 and (b) 16 March 2004 (wind speed in knots and temperature in $^{o}$C).

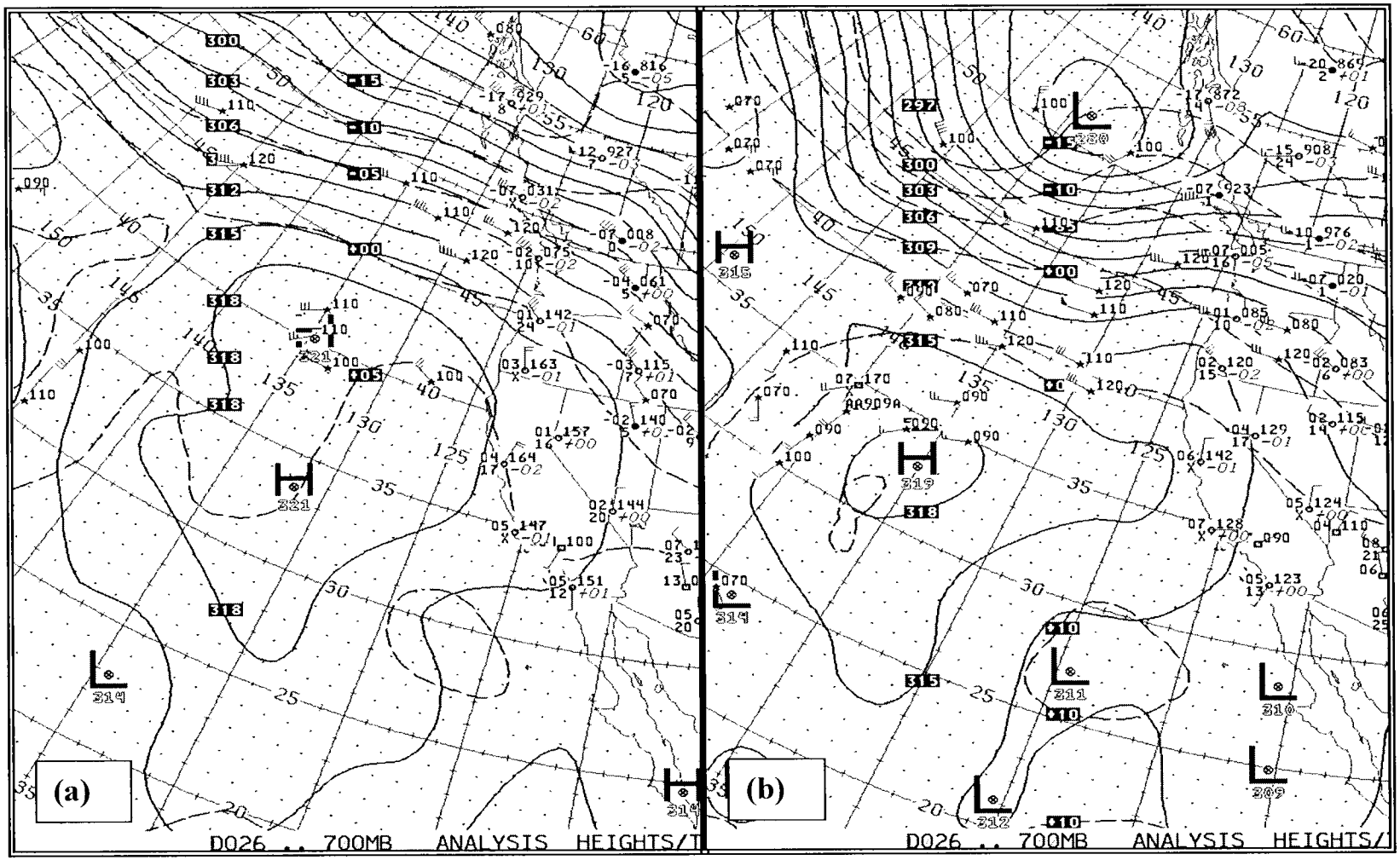


**Fig. 11.** 700 mb analysis heights/temperature valid 0000 UTC for weak offshore case (a) 17 March 2004 and (b) 18 March 2004 (wind speed in knots and temperature in $^{o}$C).

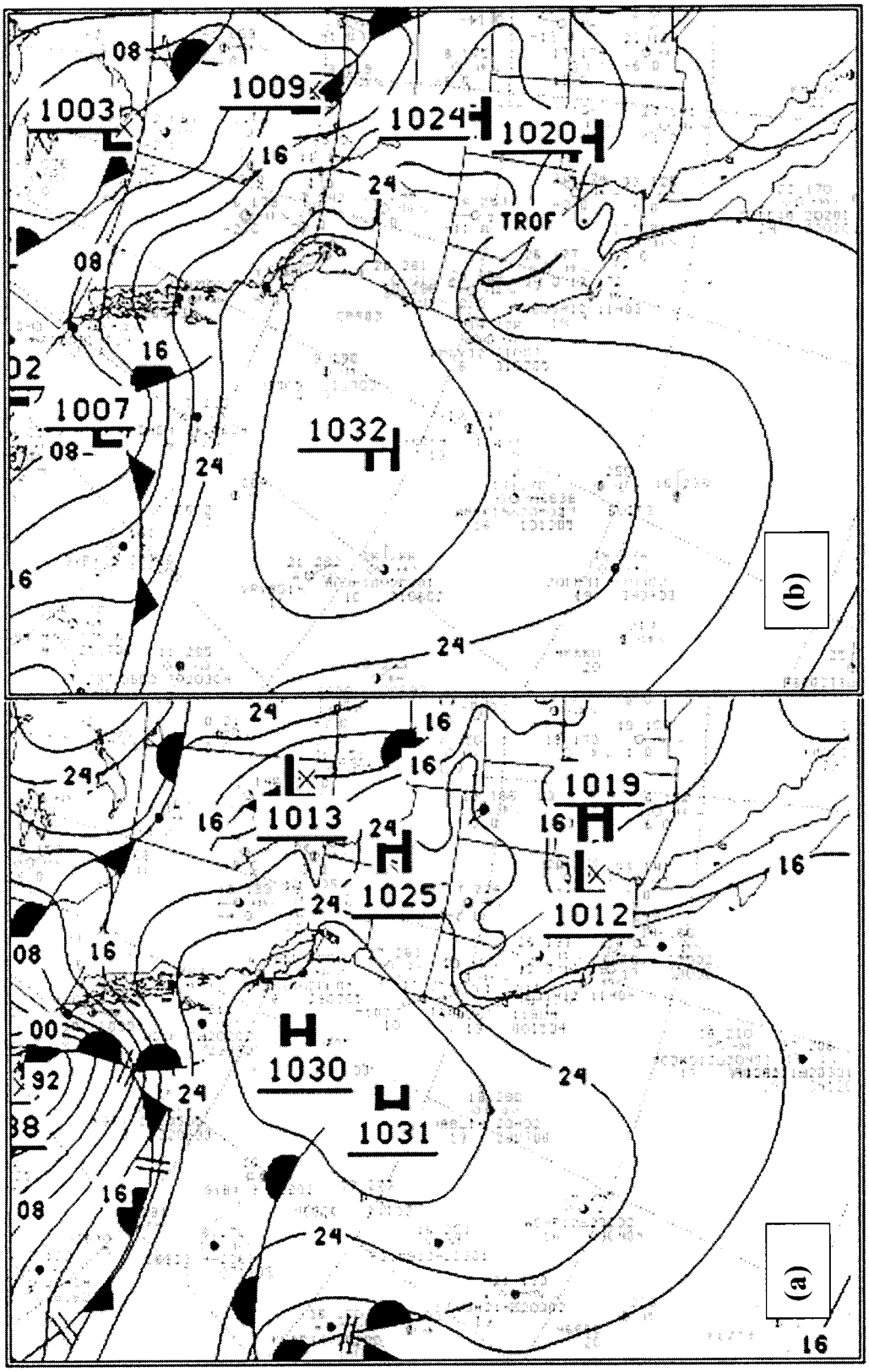


**Fig. 12.** Surface, analysis heights/temperature valid 0000 UTC for weak offshore case (a) 15 March 2004 and (b) 16 March 2004. (wind speed in knots and temperature in °C).

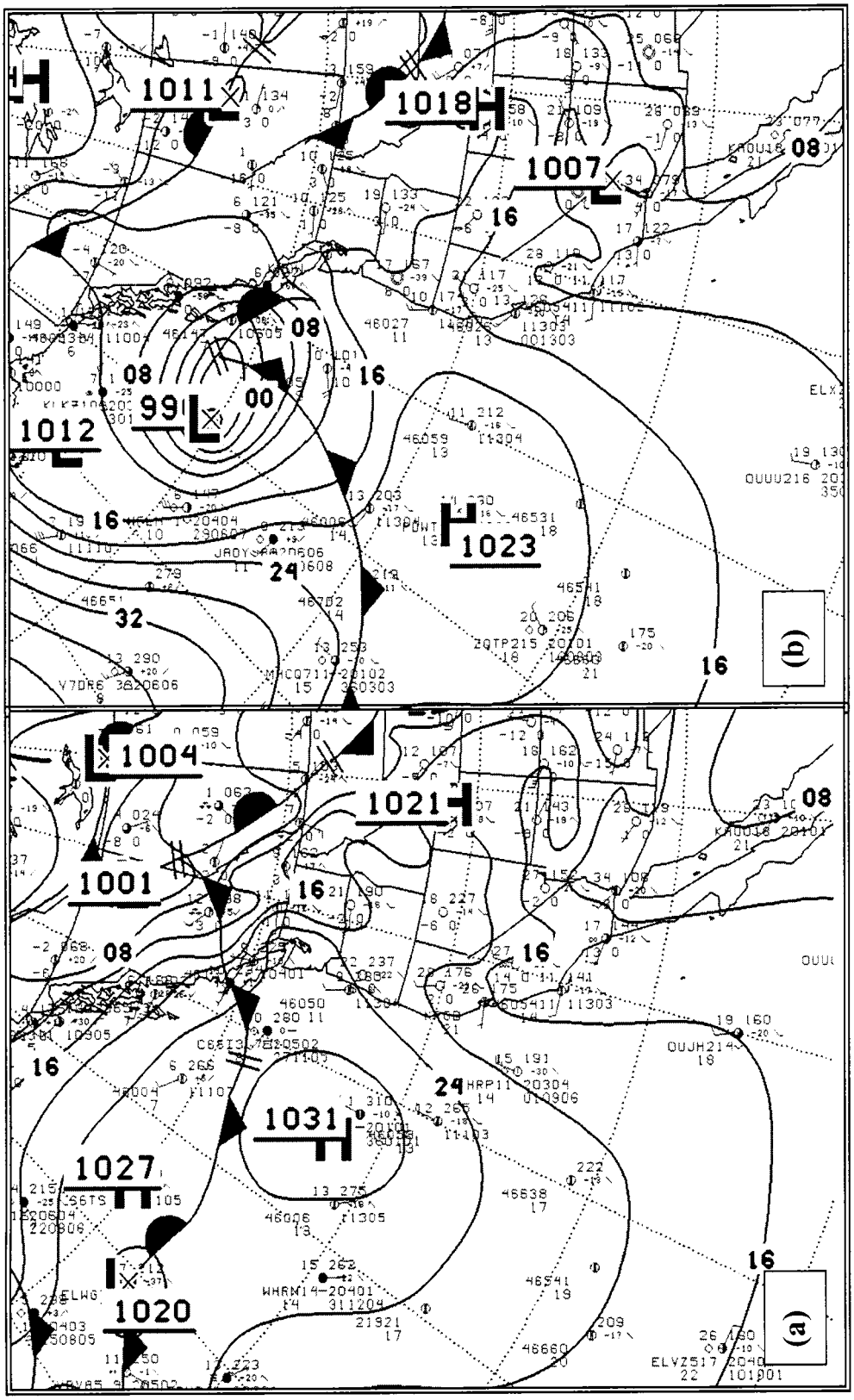


**Fig. 13.** Surface, analysis heights/temperature valid 0000 UTC for weak offshore case (a) 17 March 2004 and (b) 18 March 2004 (wind speed in knots and temperature in °C).


**Fig. 14.** Three nested grids configuration for Case 1 of the research study

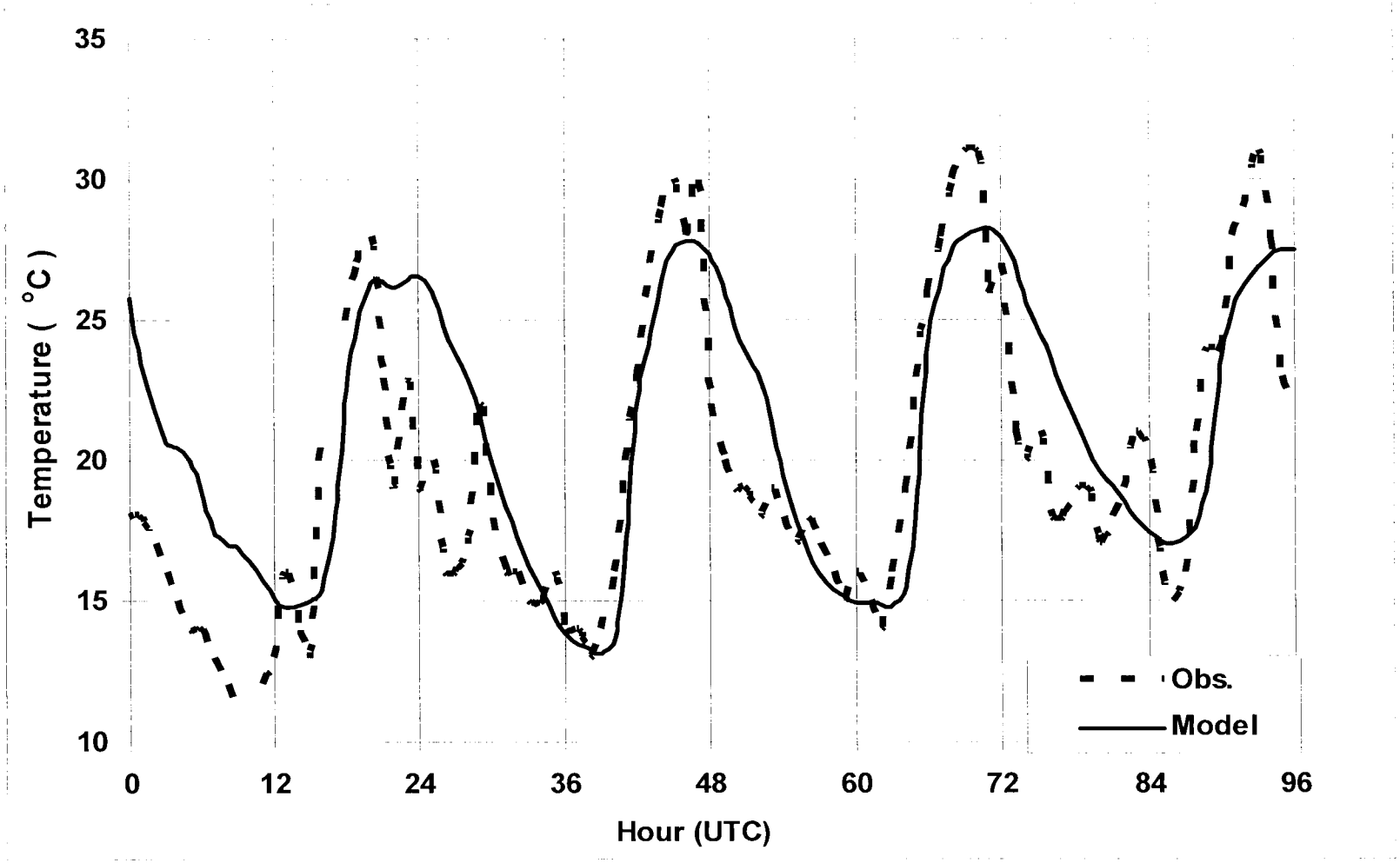


**Fig. 15.** Model (- - -) vs. observed (—) surface temperature (°C) comparison at the station in Monterey (strong offshore case).

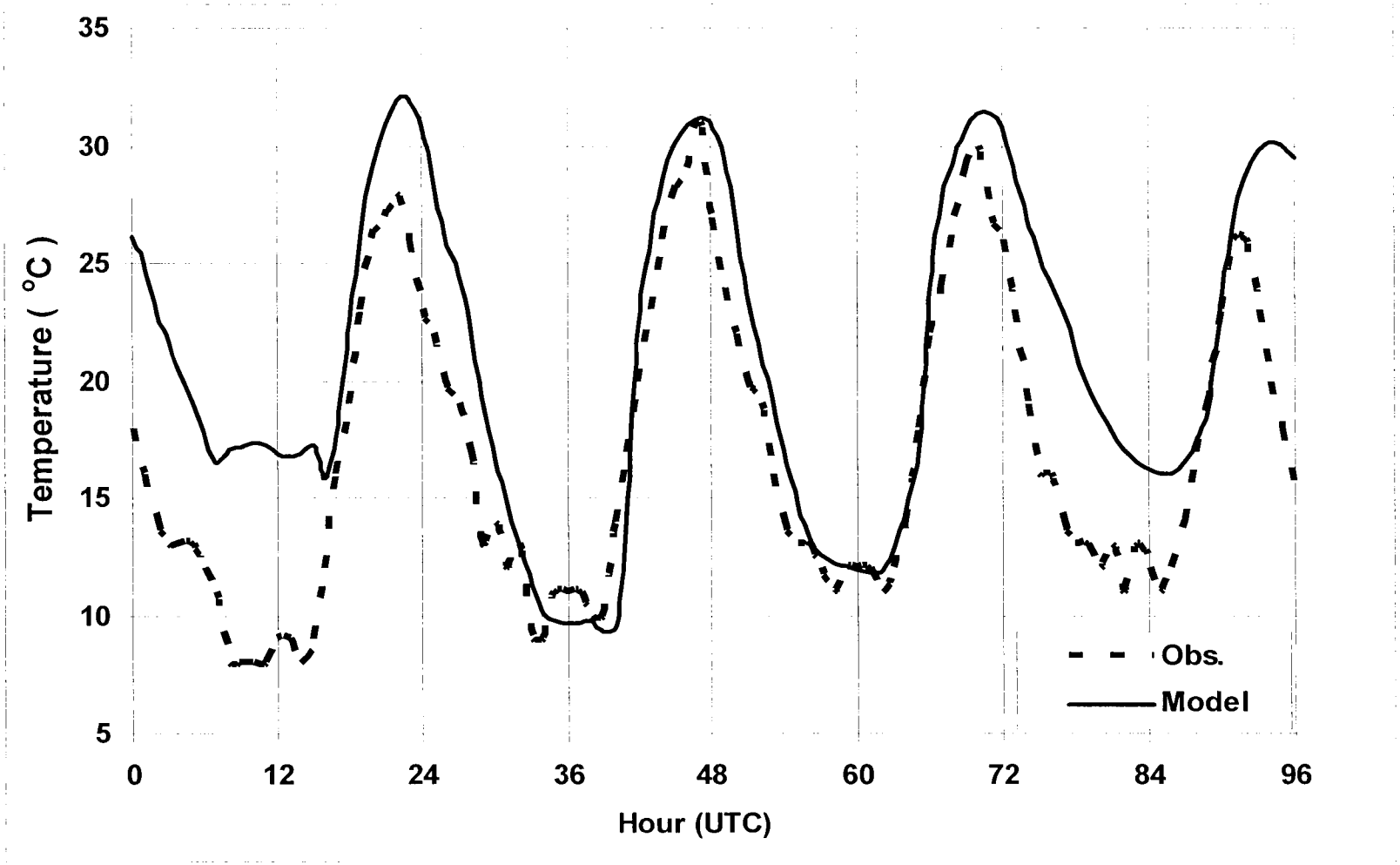


**Fig. 16.** Model (- - -) vs. observed (—) surface temperature (°C) comparison at the station in Salinas (strong offshore case).

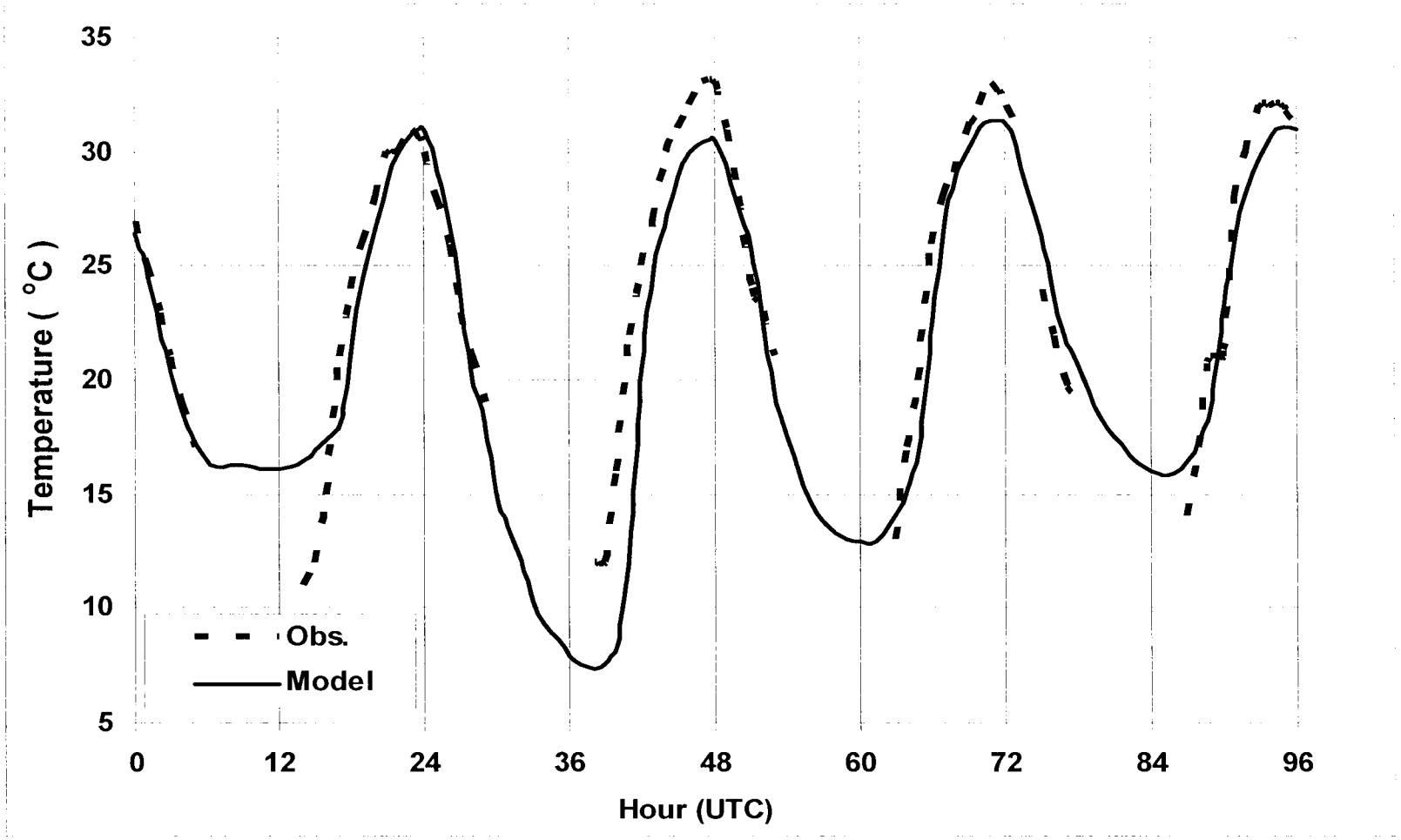


**Fig. 17.** Model (- - -) vs. observed (—) surface temperature (°C) comparison at the station in San Jose (strong offshore case).

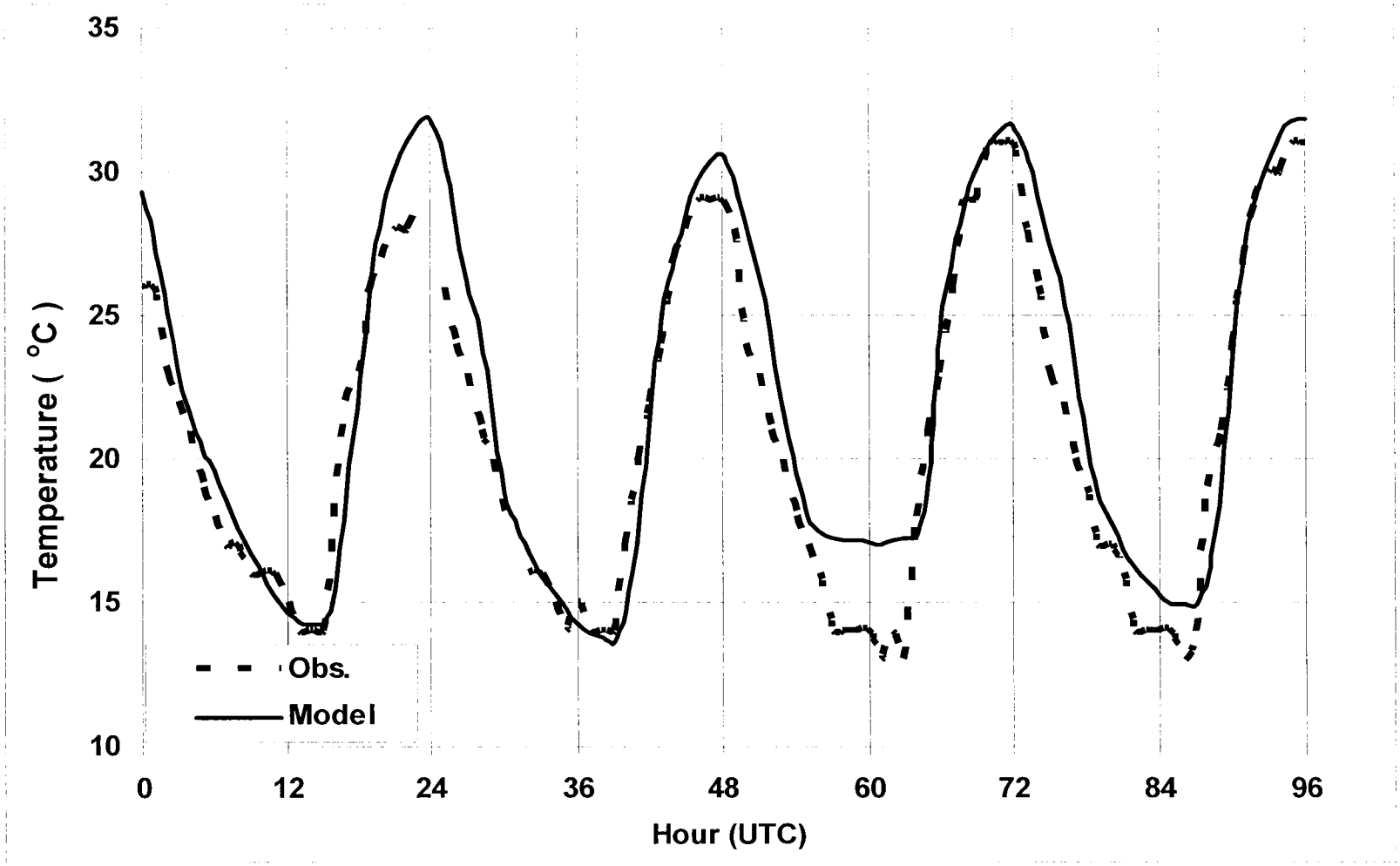


**Fig. 18.** Model (- - -) vs. observed (—) surface temperature (°C) comparison at the station in Fresno (strong offshore case).

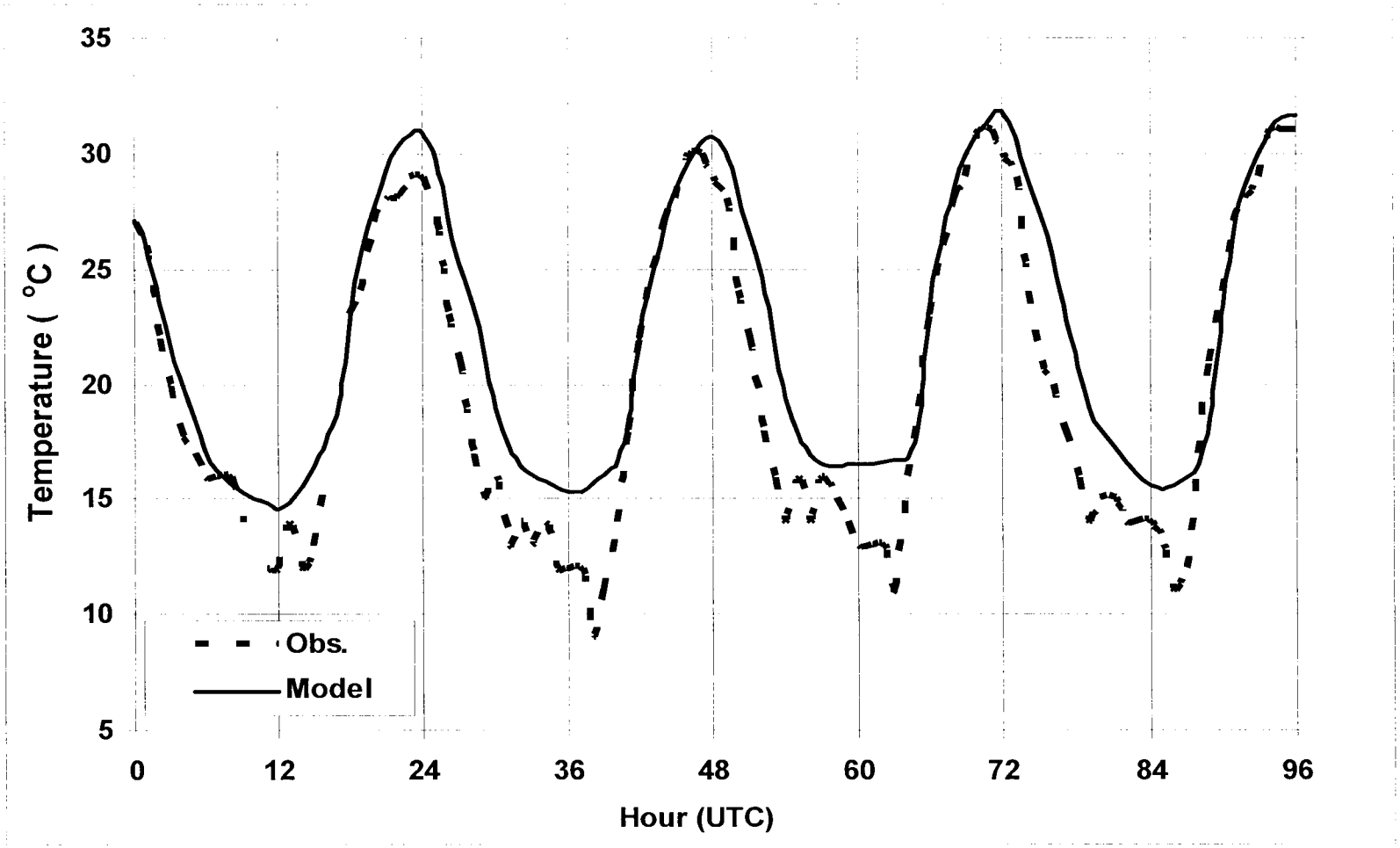


**Fig. 19.** Model (- - -) vs. observed (—) surface temperature (°C) comparison at the station in Sacramento(strong offshore case).

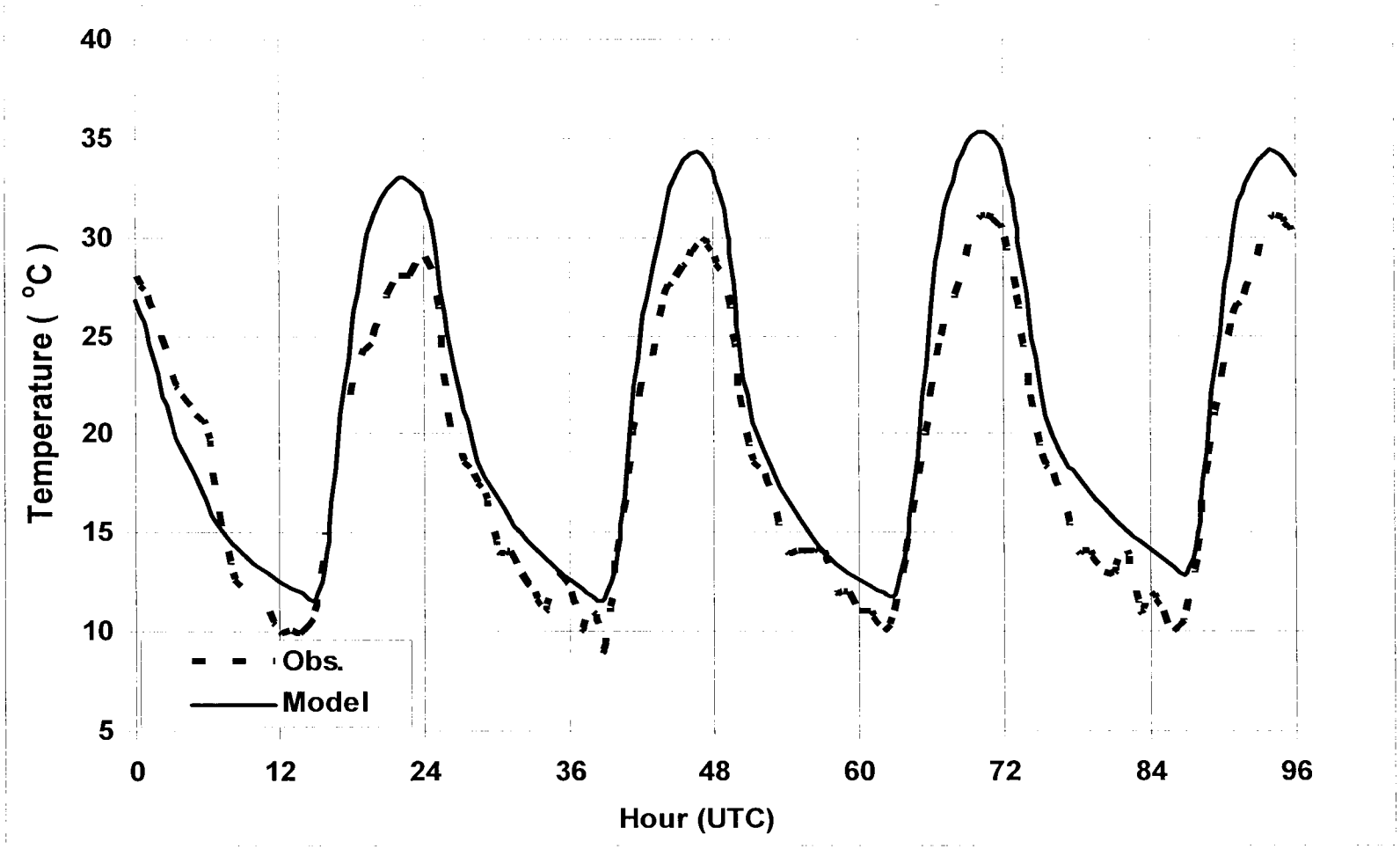


**Fig. 20.** Model (- - -) vs. observed (—) surface temperature (°C) comparison at the station in Modesto (strong offshore case).

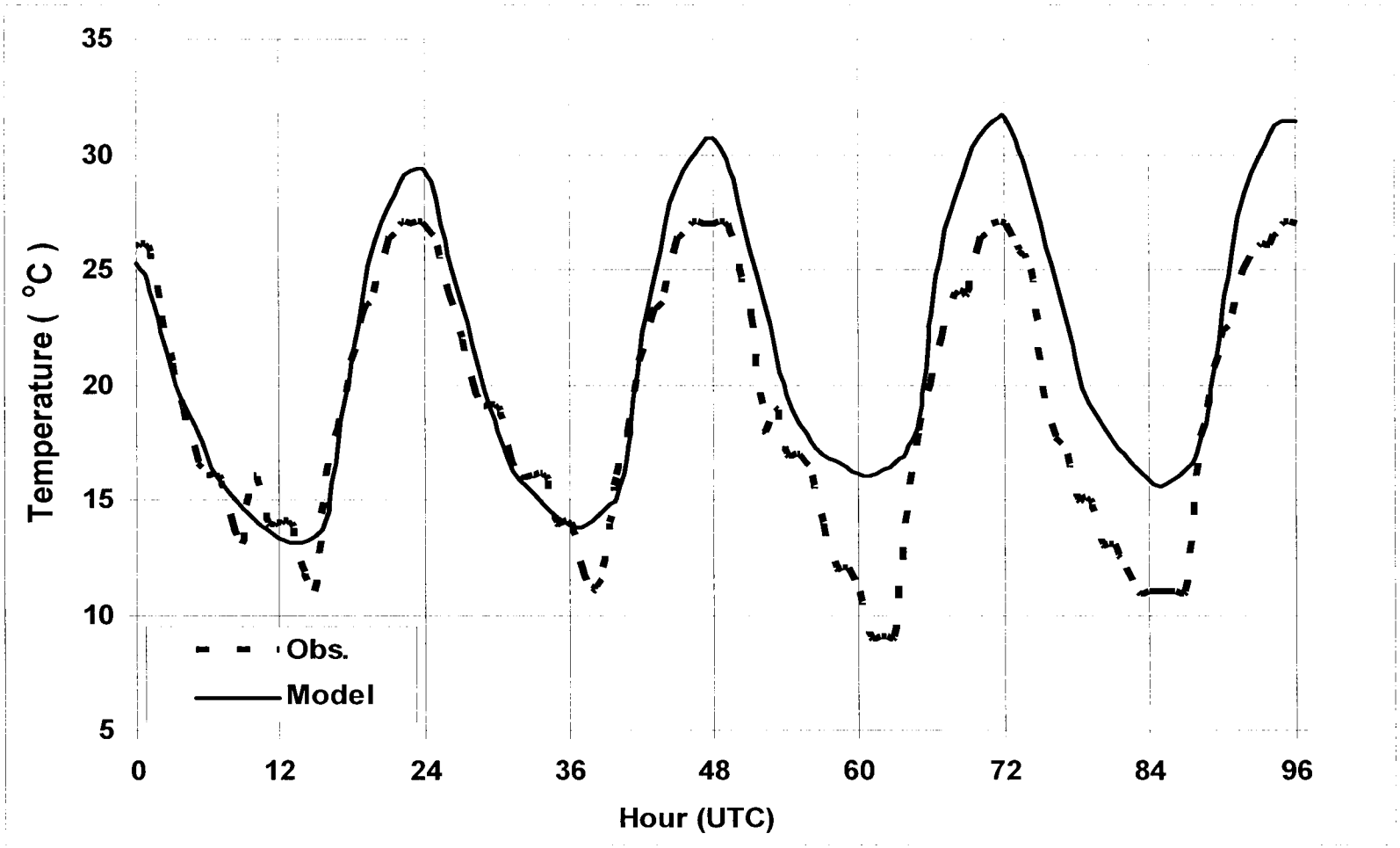


**Fig. 21.** Model (- - -) vs. observed (—) temperature (°C) comparison at the station in Merced Macready (strong offshore case).

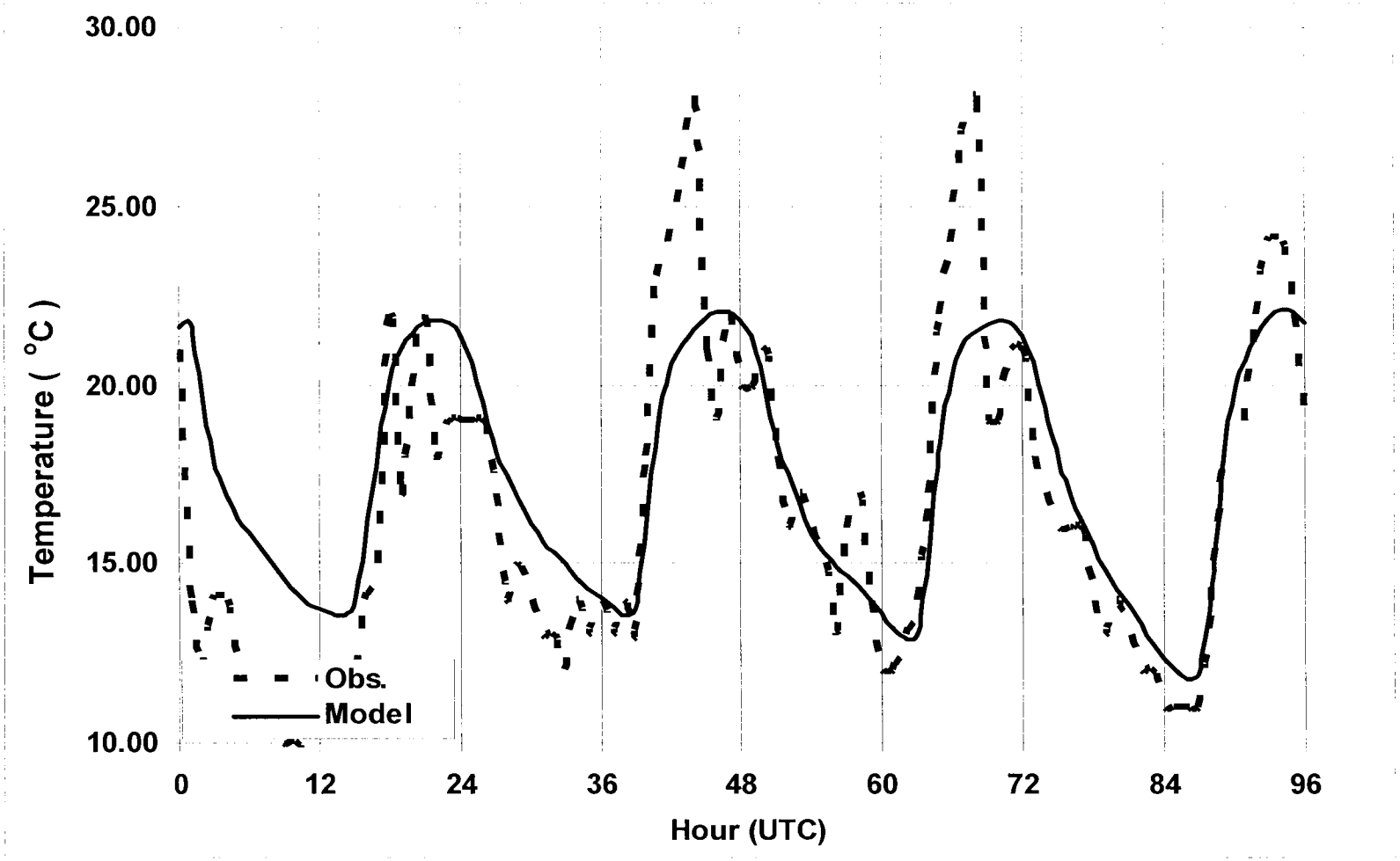


**Fig. 22.** Model (- - -) vs. observed (—) surface temperature (°C) comparison at the station in Monterey (weak offshore case).

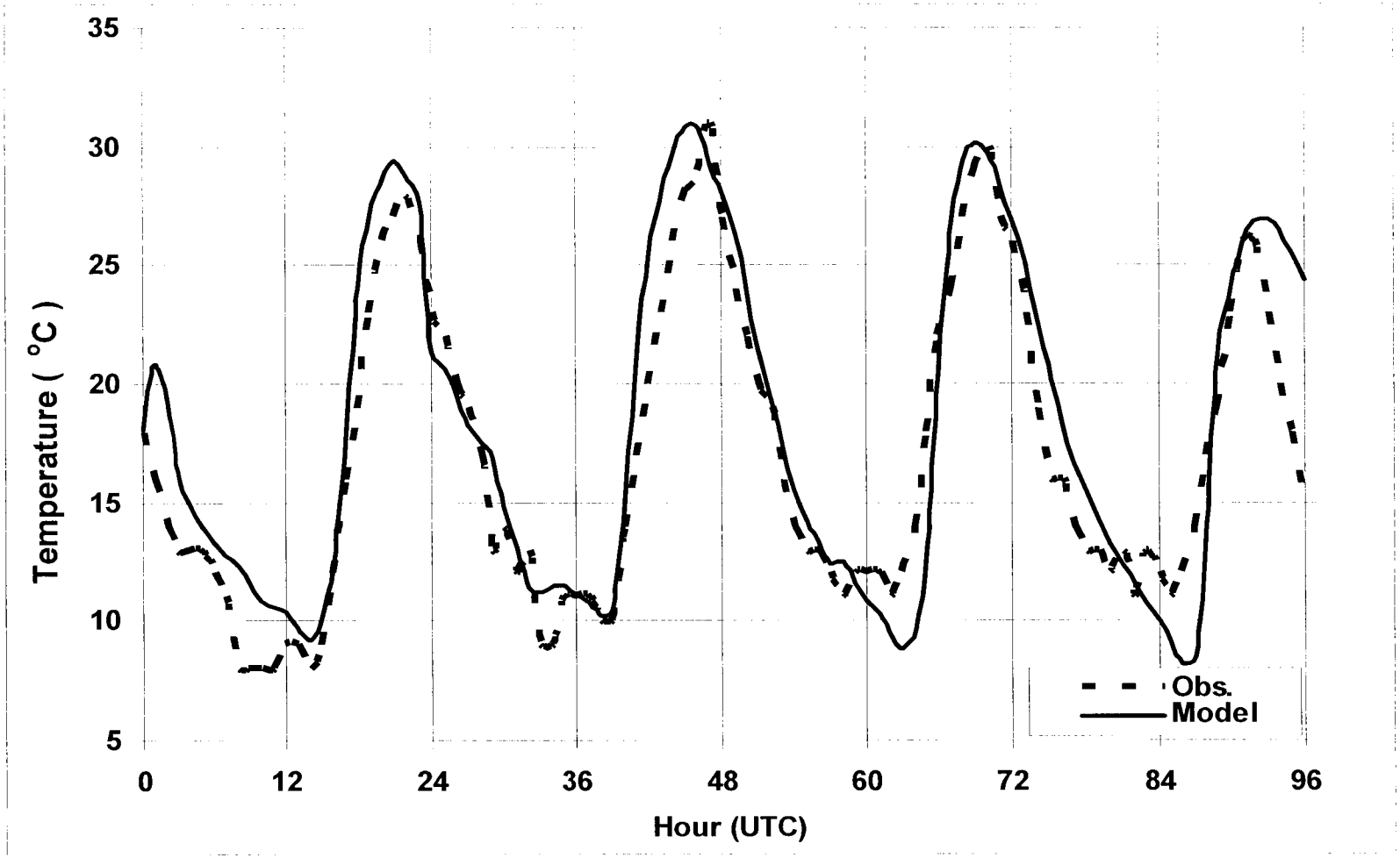


**Fig. 23.** Model (- - -) vs. observed (—) surface temperature (°C) comparison at the station in Salinas (weak offshore case).

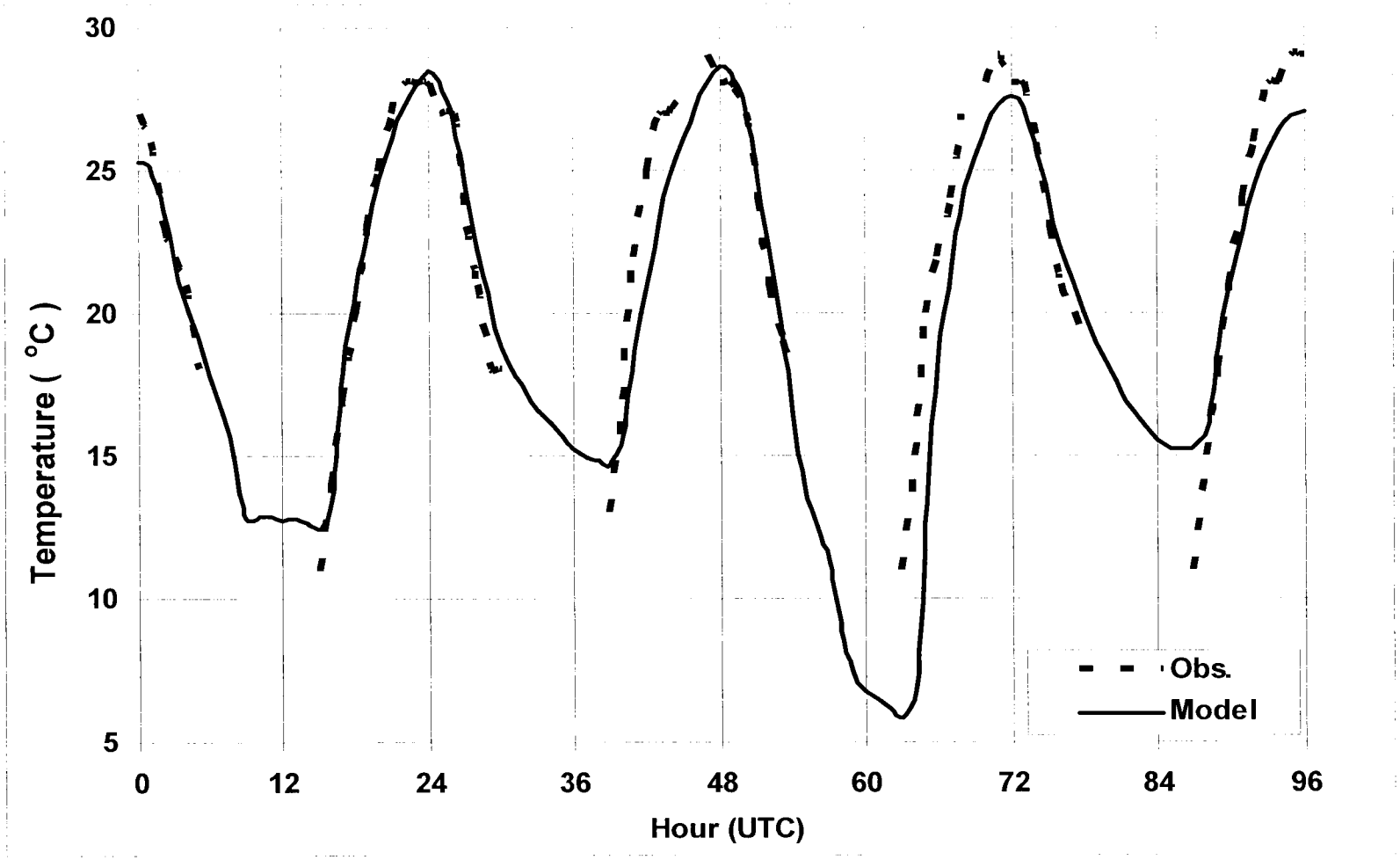


**Fig. 24.** Model (- - -) vs. observed (—) surface temperature (°C) comparison atthe station in San Jose (weak offshore case).

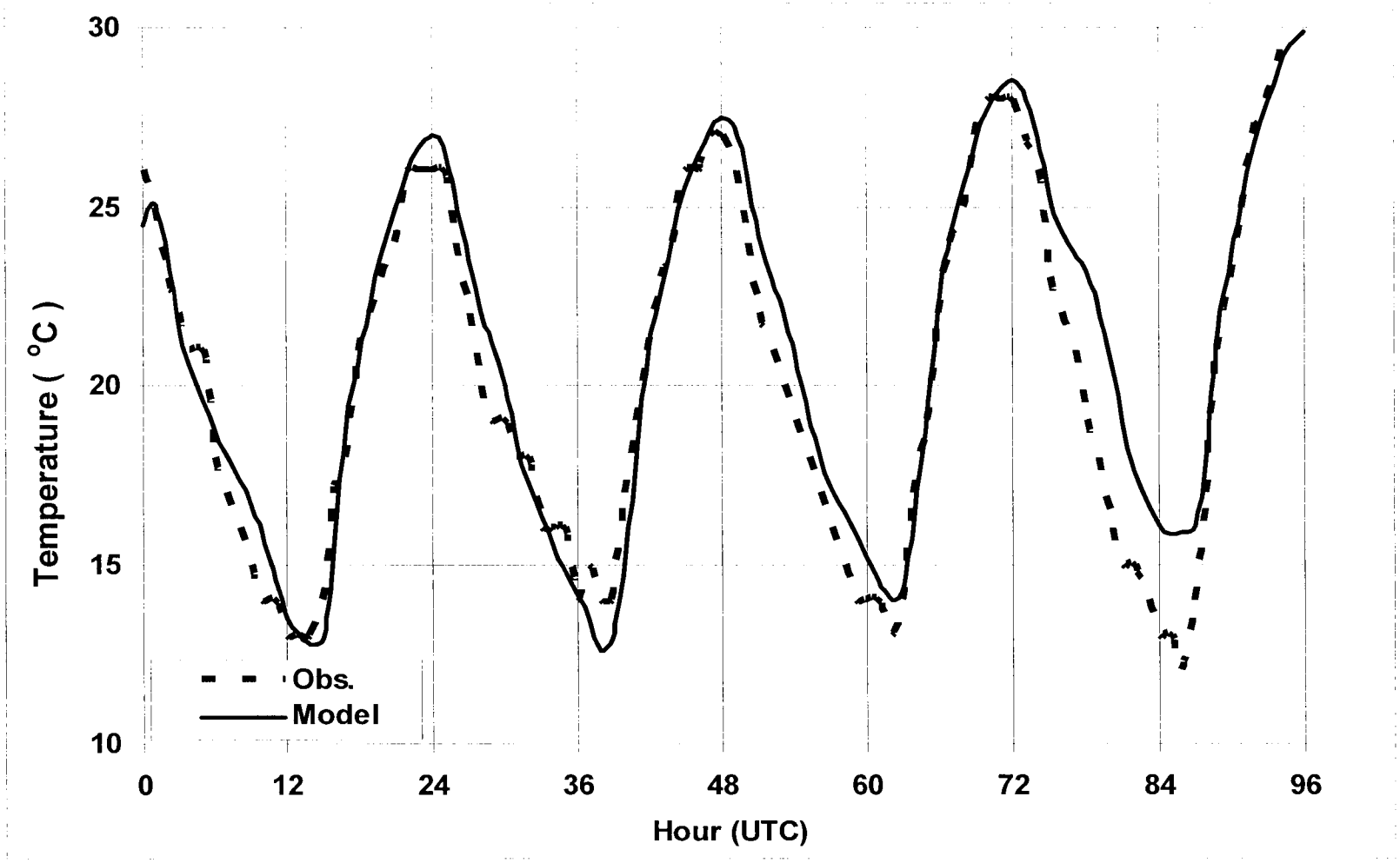


**Fig. 25.** Model (- - -) vs. observed (—) surface temperature (°C) comparison at the station in Sacramento (weak offshore case).

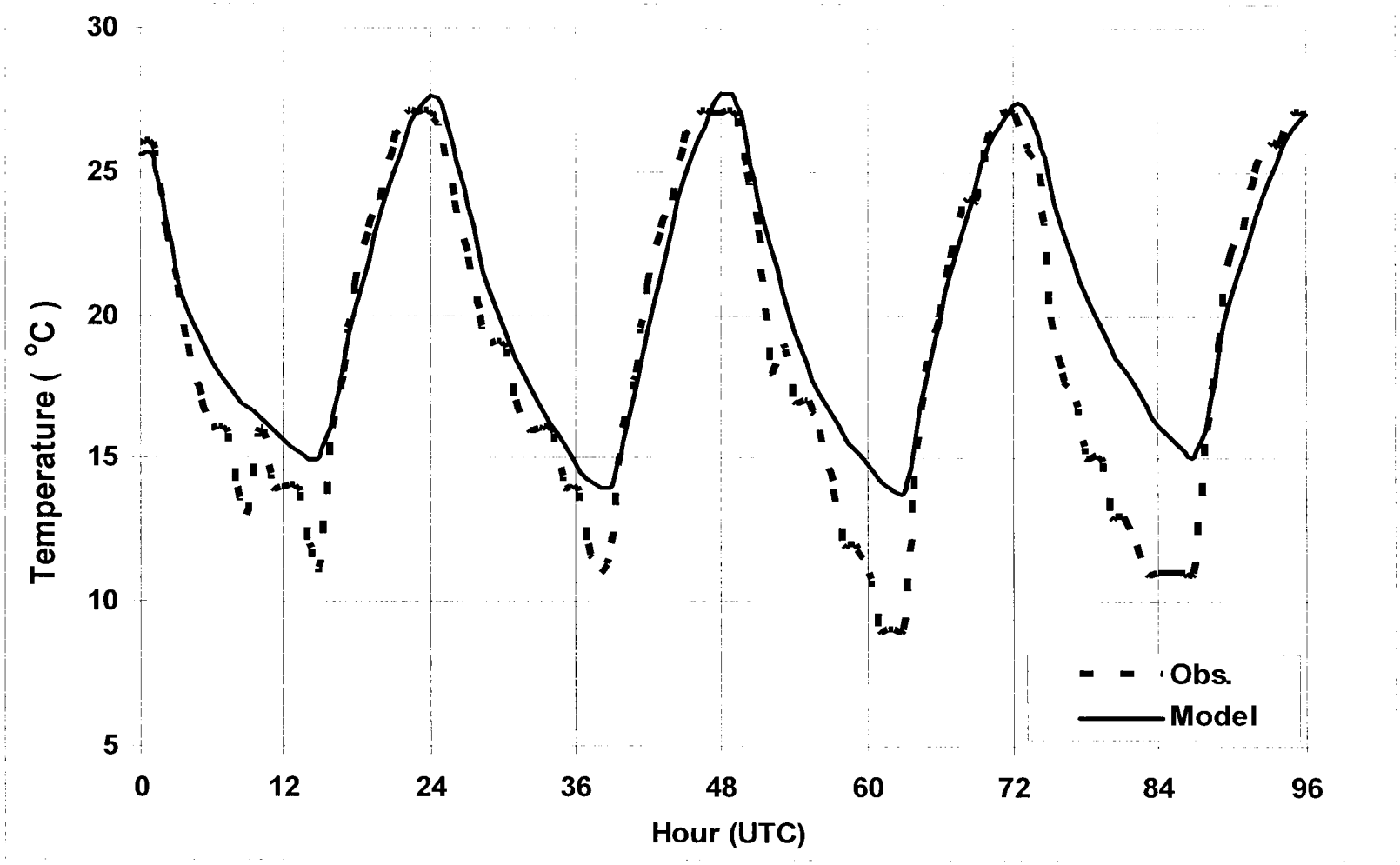


**Fig. 26.** Model (- - -) vs. observed (—) surface temperature (°C) comparison at the station in Modesto (weak offshore case)

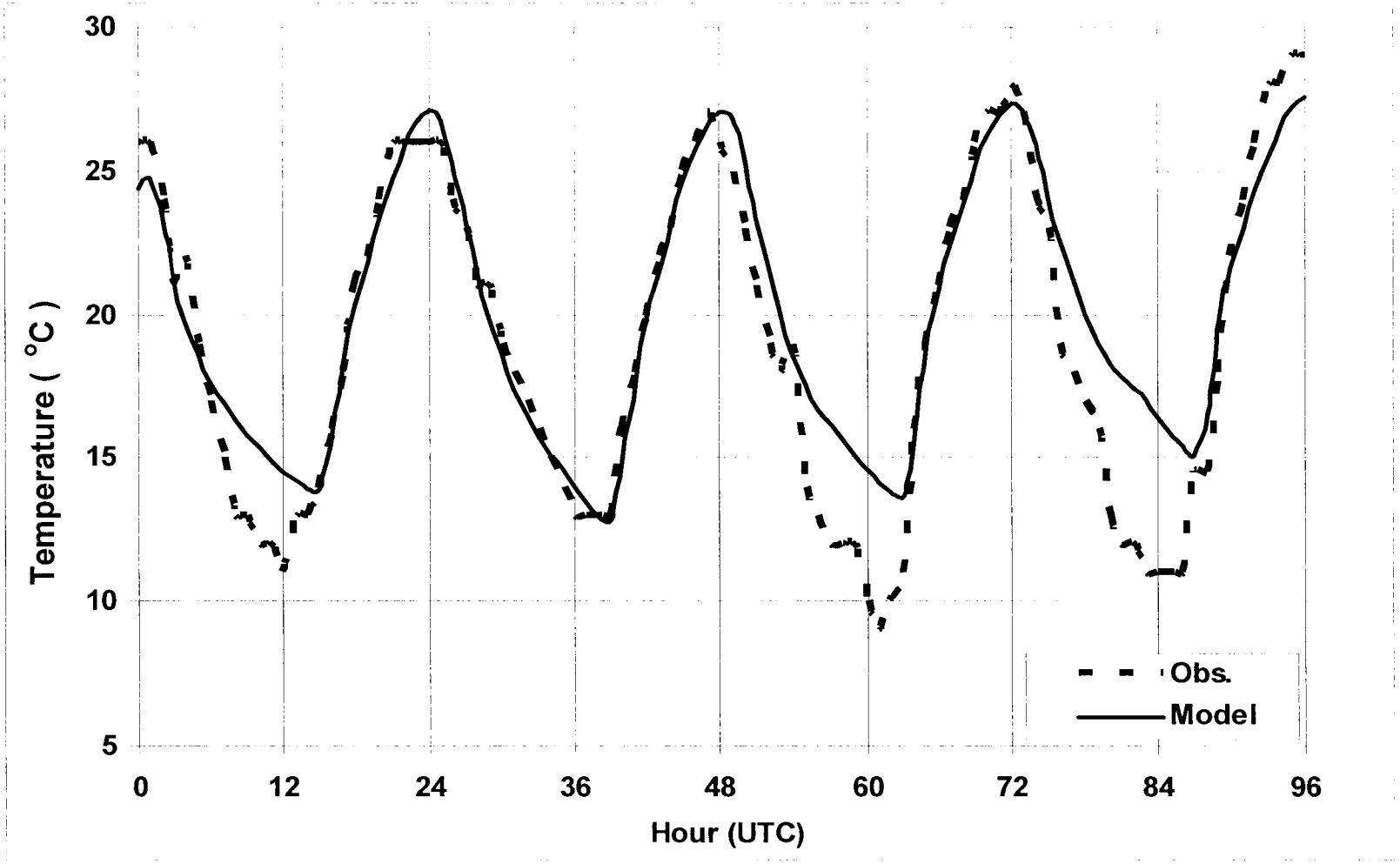


**Fig. 27.** Model (- - -) vs. observed (—) surface temperature (°C) comparison at the station in Fresno (weak offshore case).

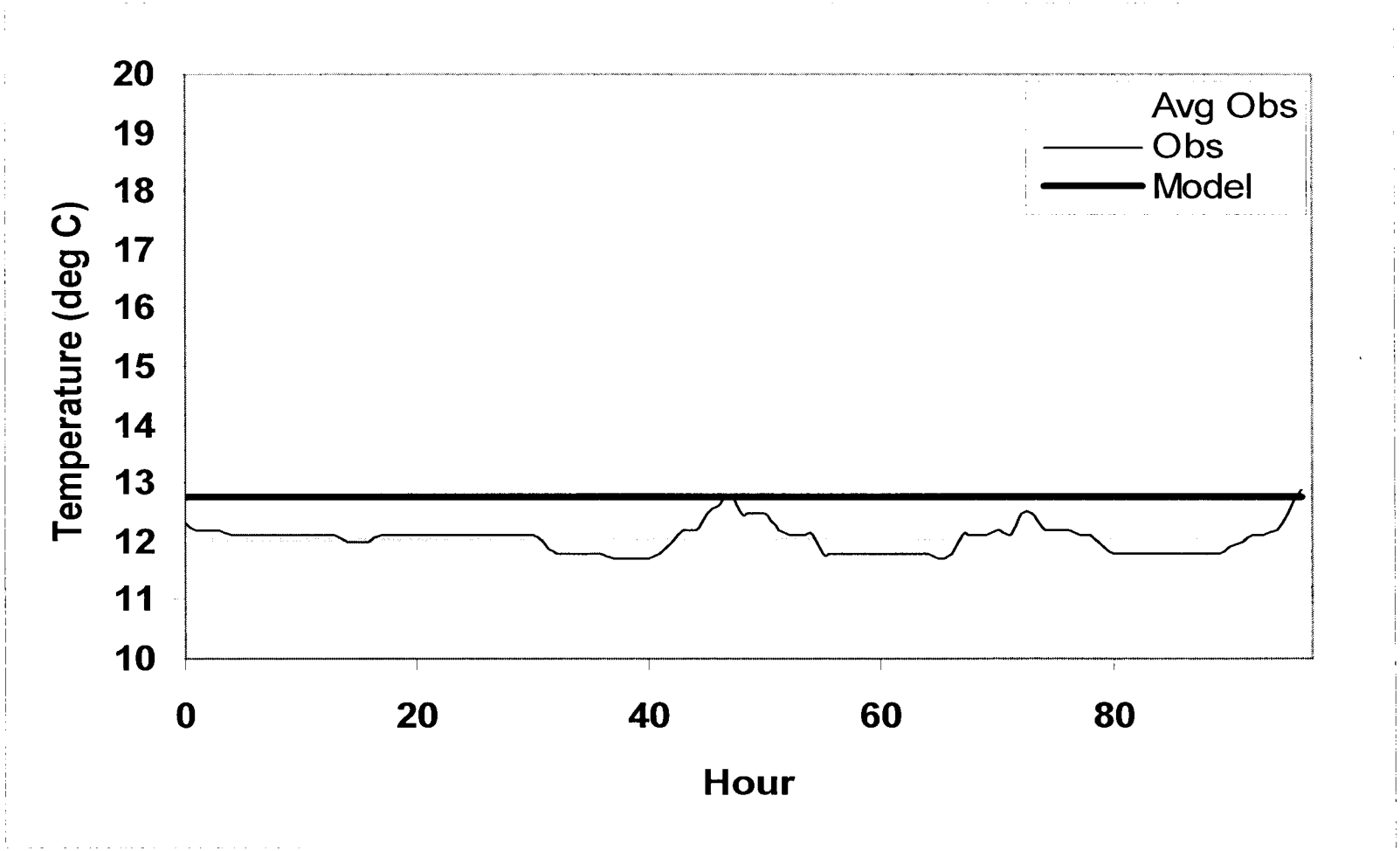


**Fig. 28.** Model vs. observed sea surface temperature (°C) comparison at a buoy station 49 km from Monterey (seaward), model surface temperatures were not updated with time

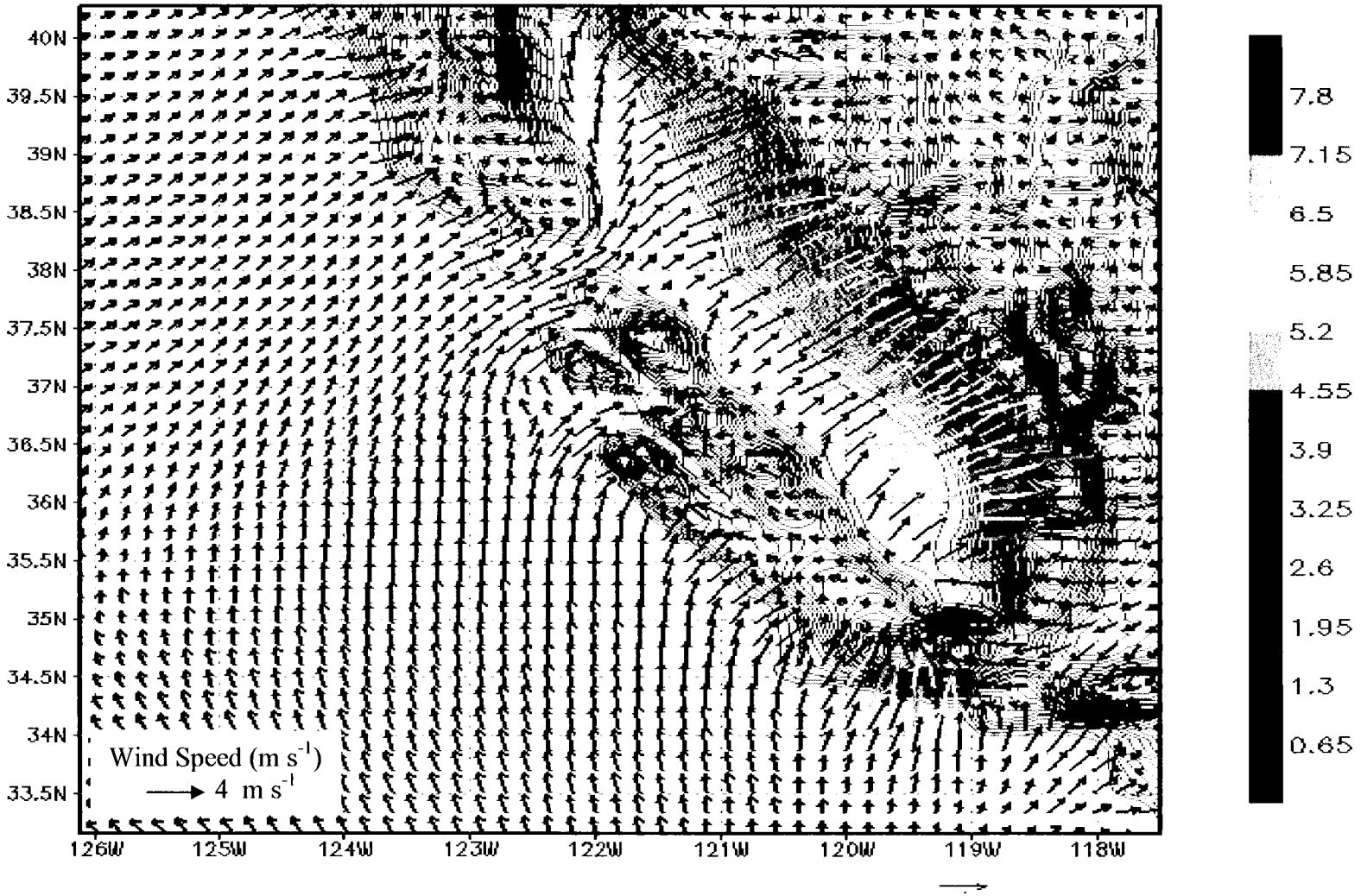


**Fig. 29.** 1000 mb wind field (m $s^{-1}$) 0000 UTC 25 OCT 2003 (Strong offshore case).

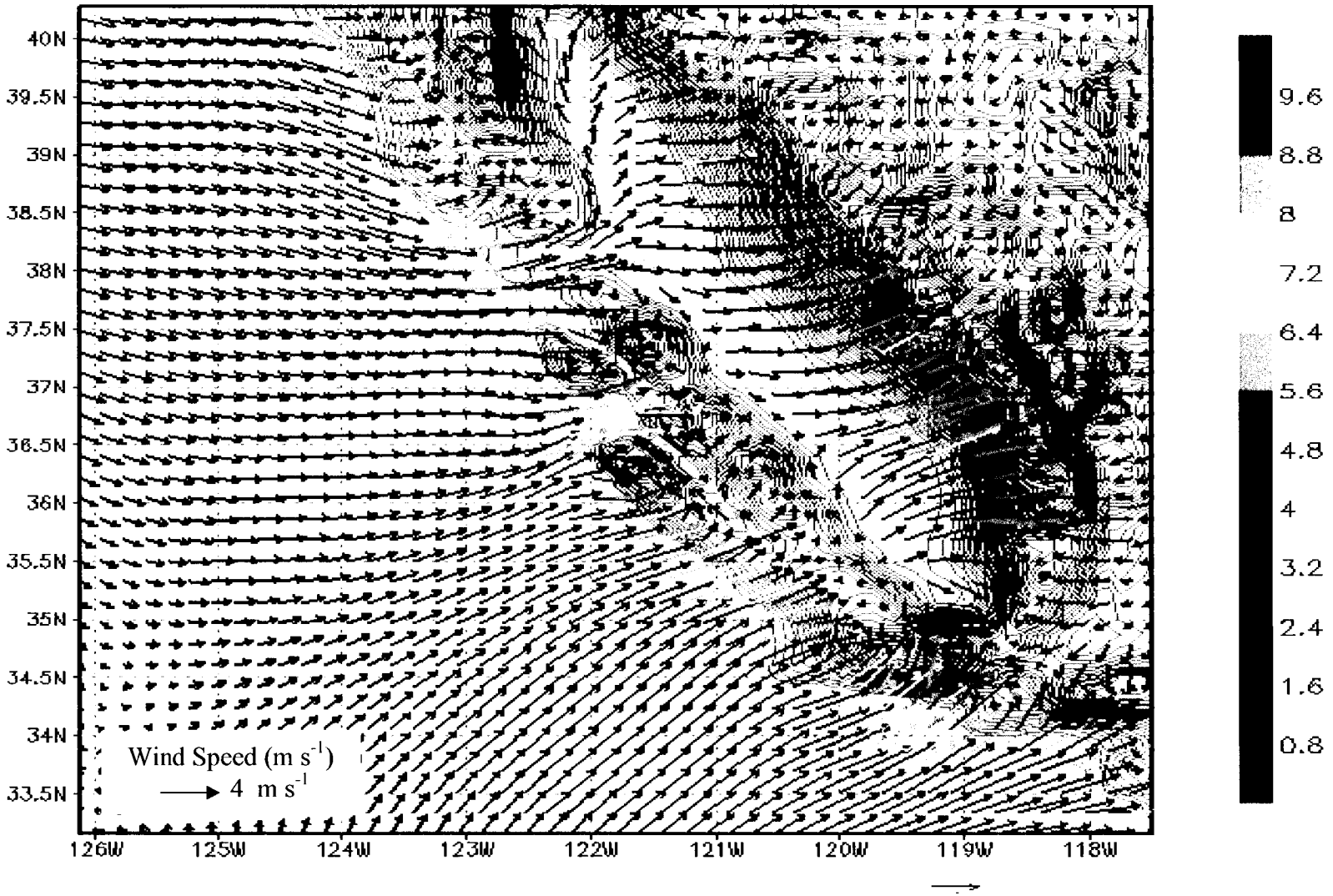


**Fig. 30.** 1000 mb wind field (m $s^{-1}$) 0000 UTC 26 OCT 2003 (Strong offshore case).

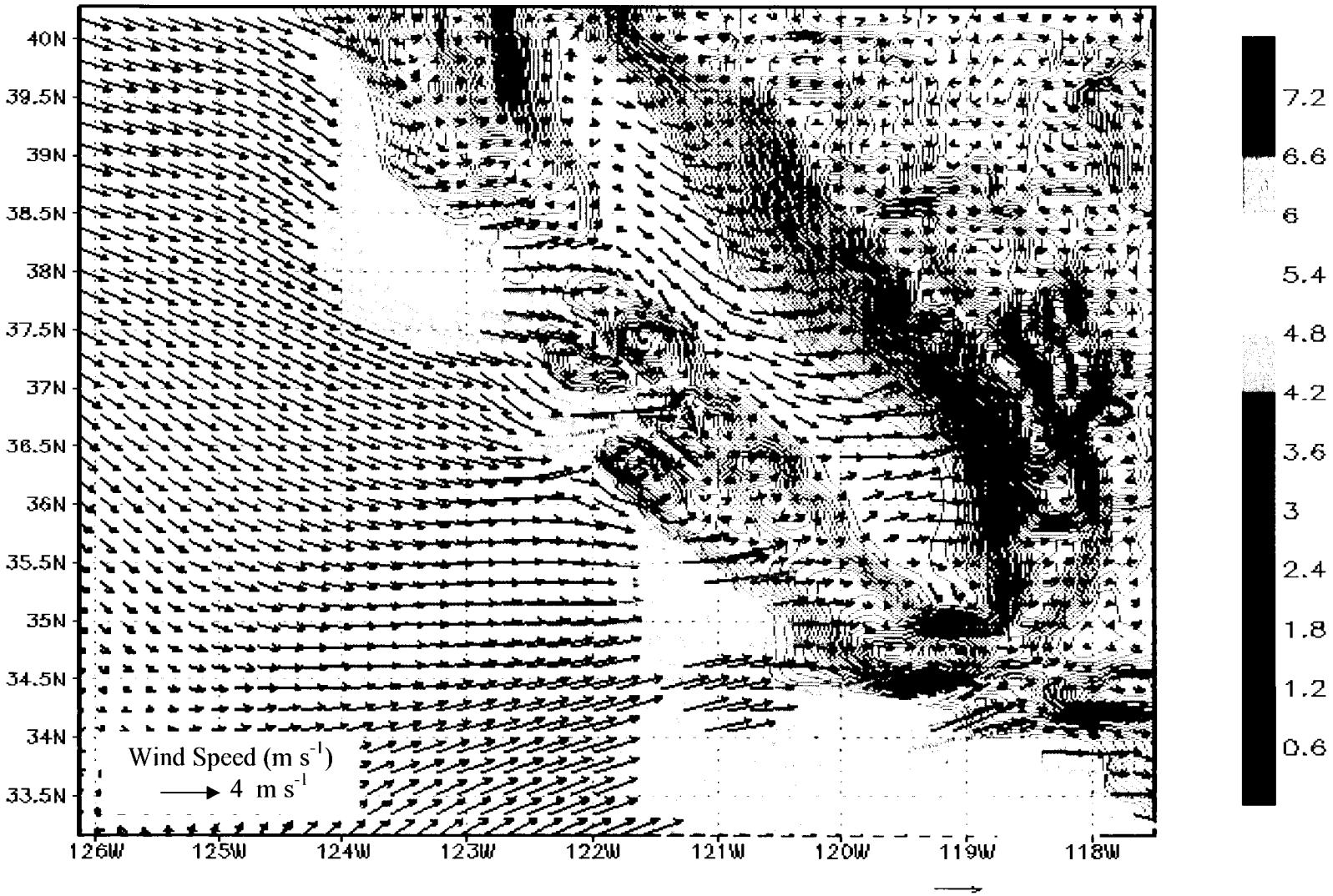


**Fig. 31.** 1000 mb wind field (m $s^{-1}$) 0400 UTC 25 OCT 2003 (Strong offshore case).

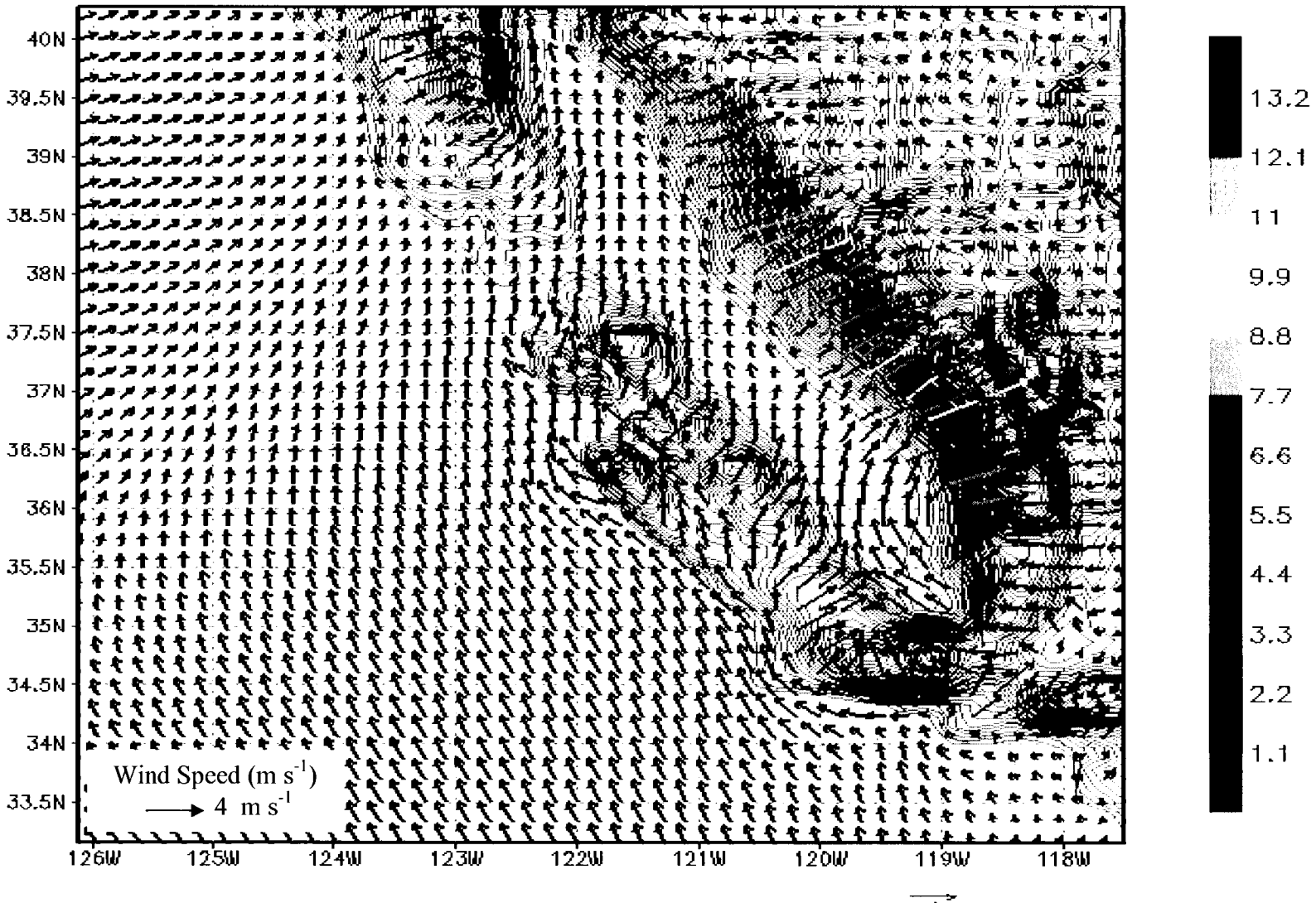


**Fig. 32.** 925 mb wind field (m $s^{-1}$) 2000 UTC 25 OCT 2003 (Strong offshore case).

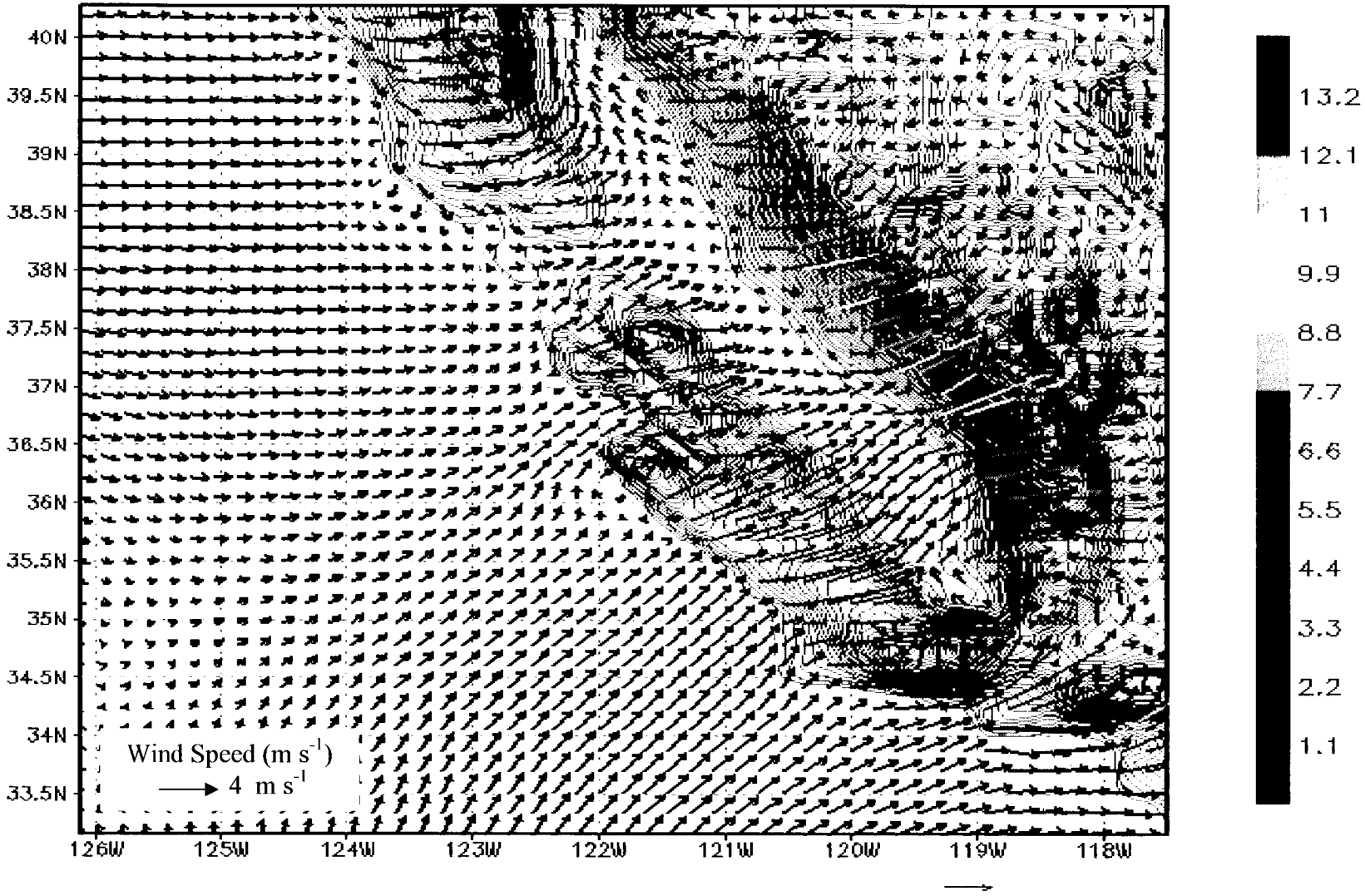


**Fig. 33.** 925 mb wind field (m $s^{-1}$) 0000 UTC 26 OCT 2003 (Strong offshore case).

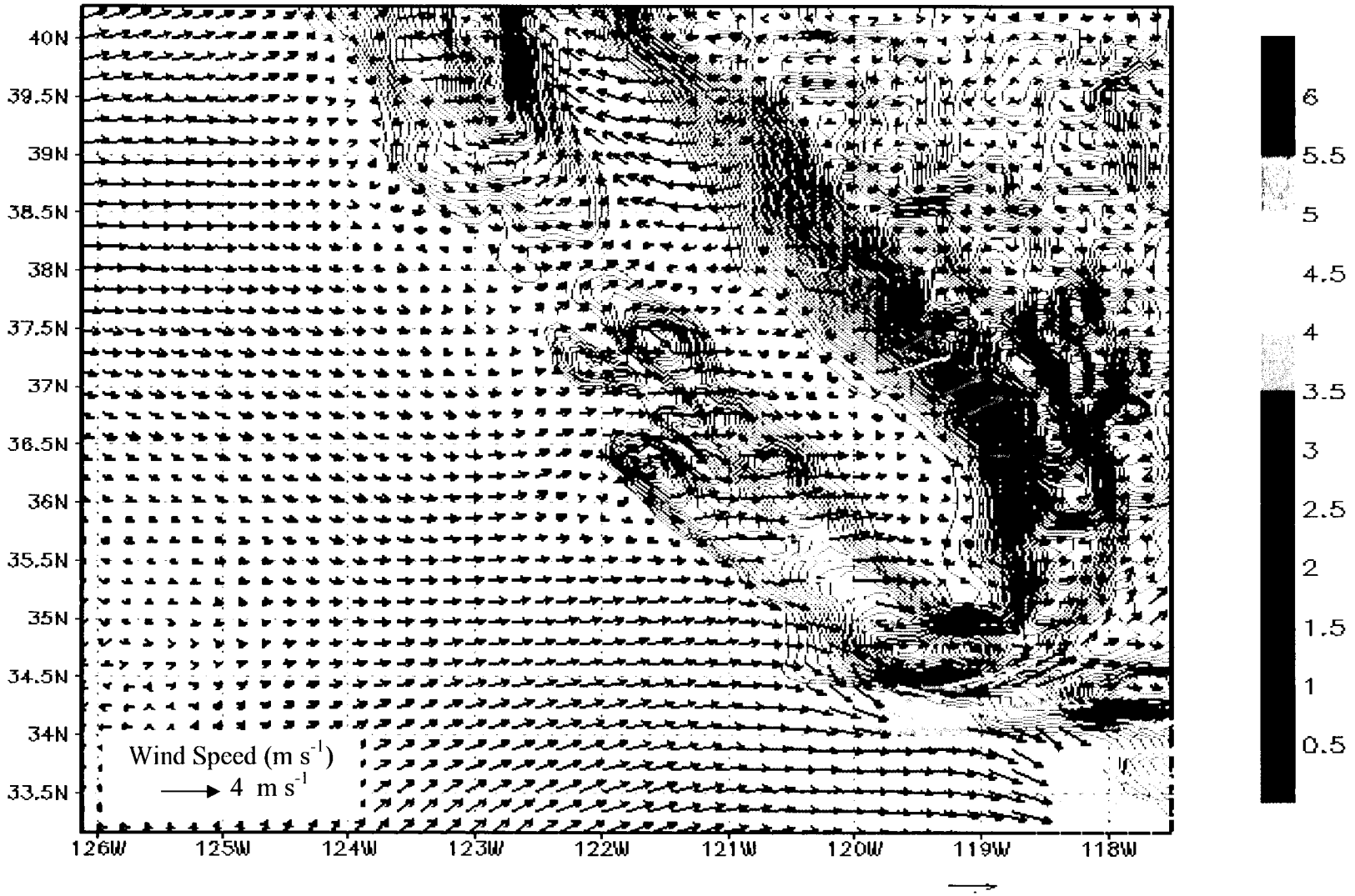


**Fig. 34.** 925 mb wind field (m $s^{-1}$) 0400 UTC 26 OCT 2003 (Strong offshore case).

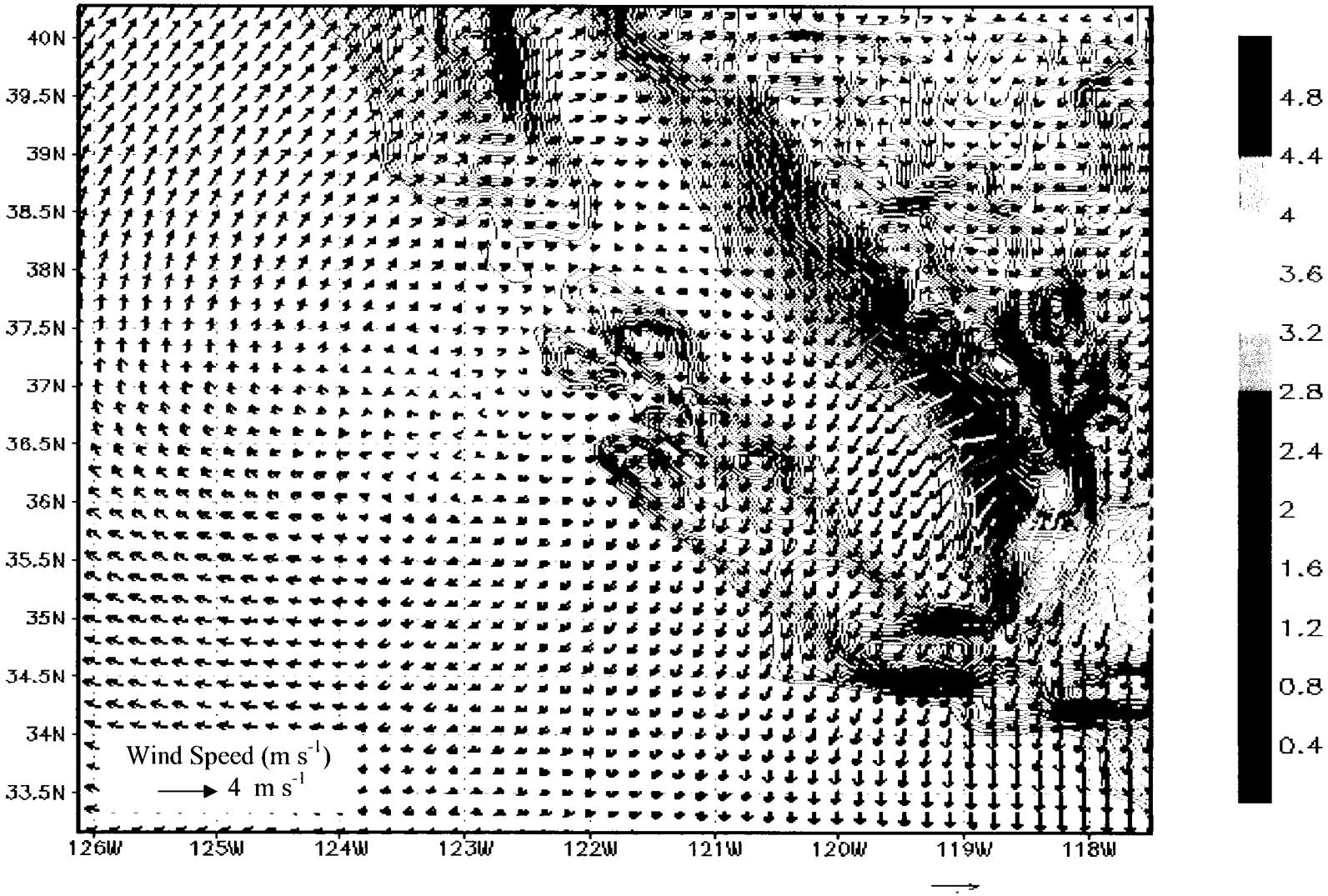


**Fig. 35.** 700 mb wind field (m $s^{-1}$) 2000 UTC 25 OCT 2003 (Strong offshore case).

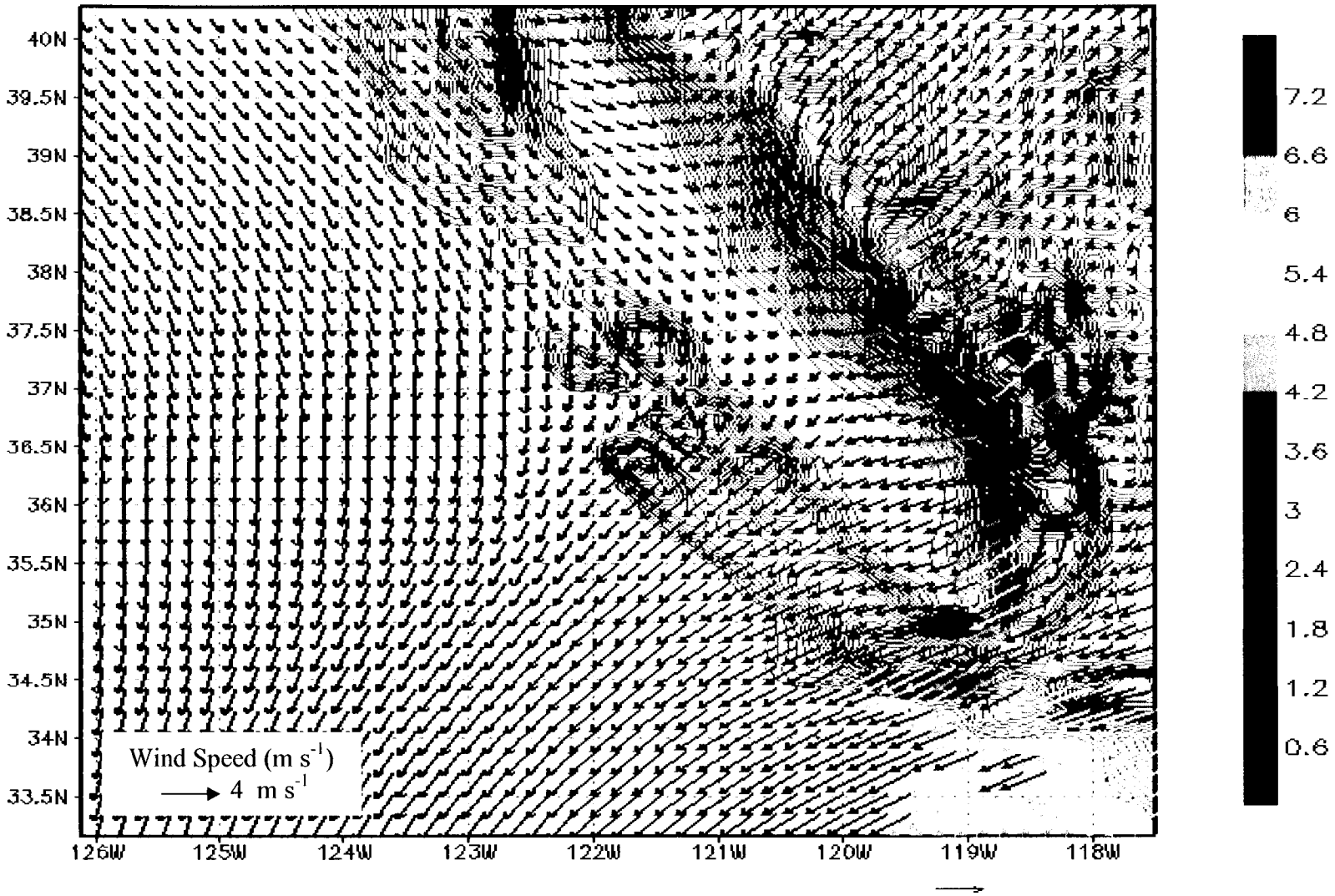


**Fig. 36.** 700 mb wind field (m $s^{-1}$) 0000 UTC 26 OCT 2003 (Strong offshore case).

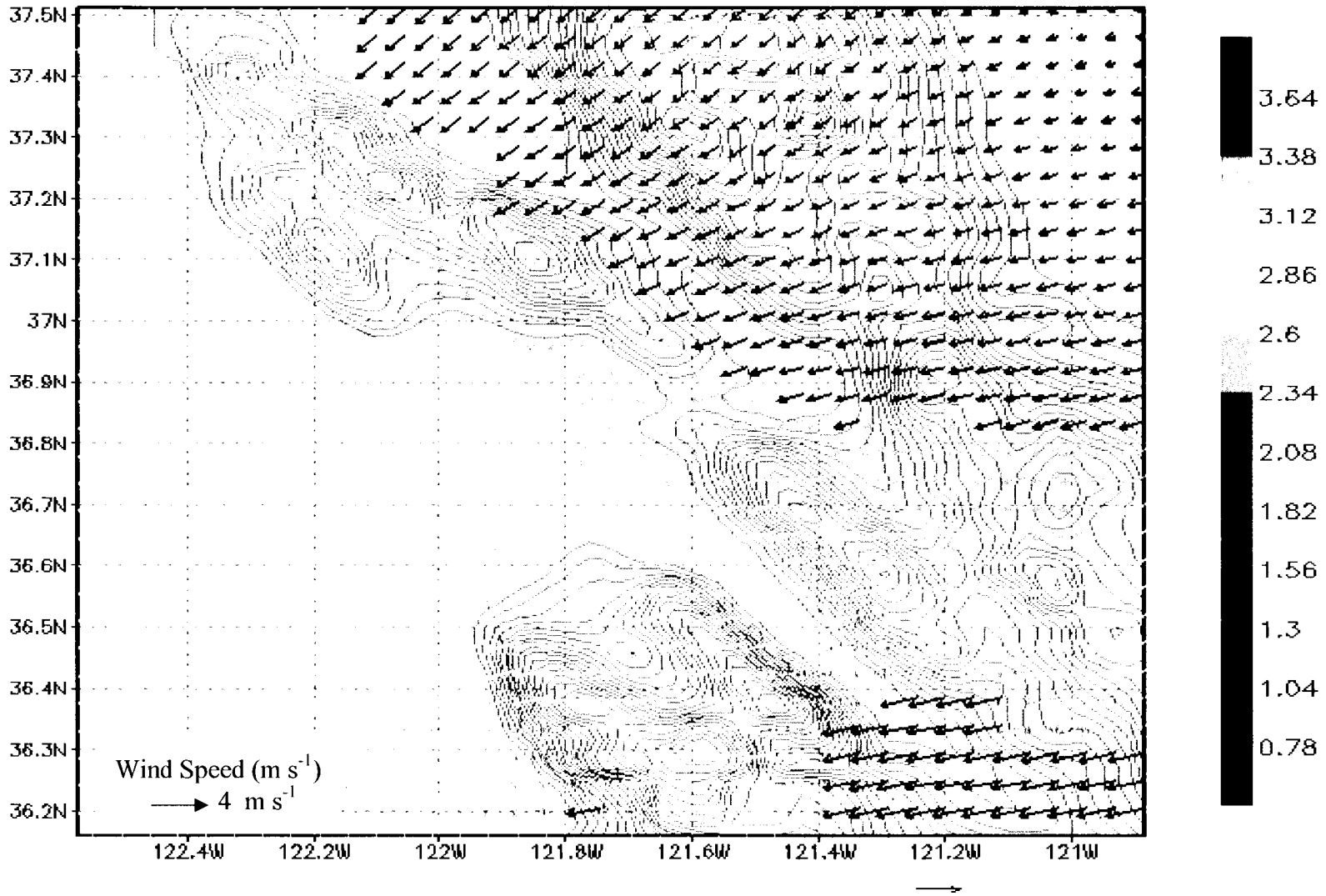


**Fig. 37.** 700 mb wind field (m $s^{-1}$) 0400 UTC 27 OCT 2003 (Strong offshore case).

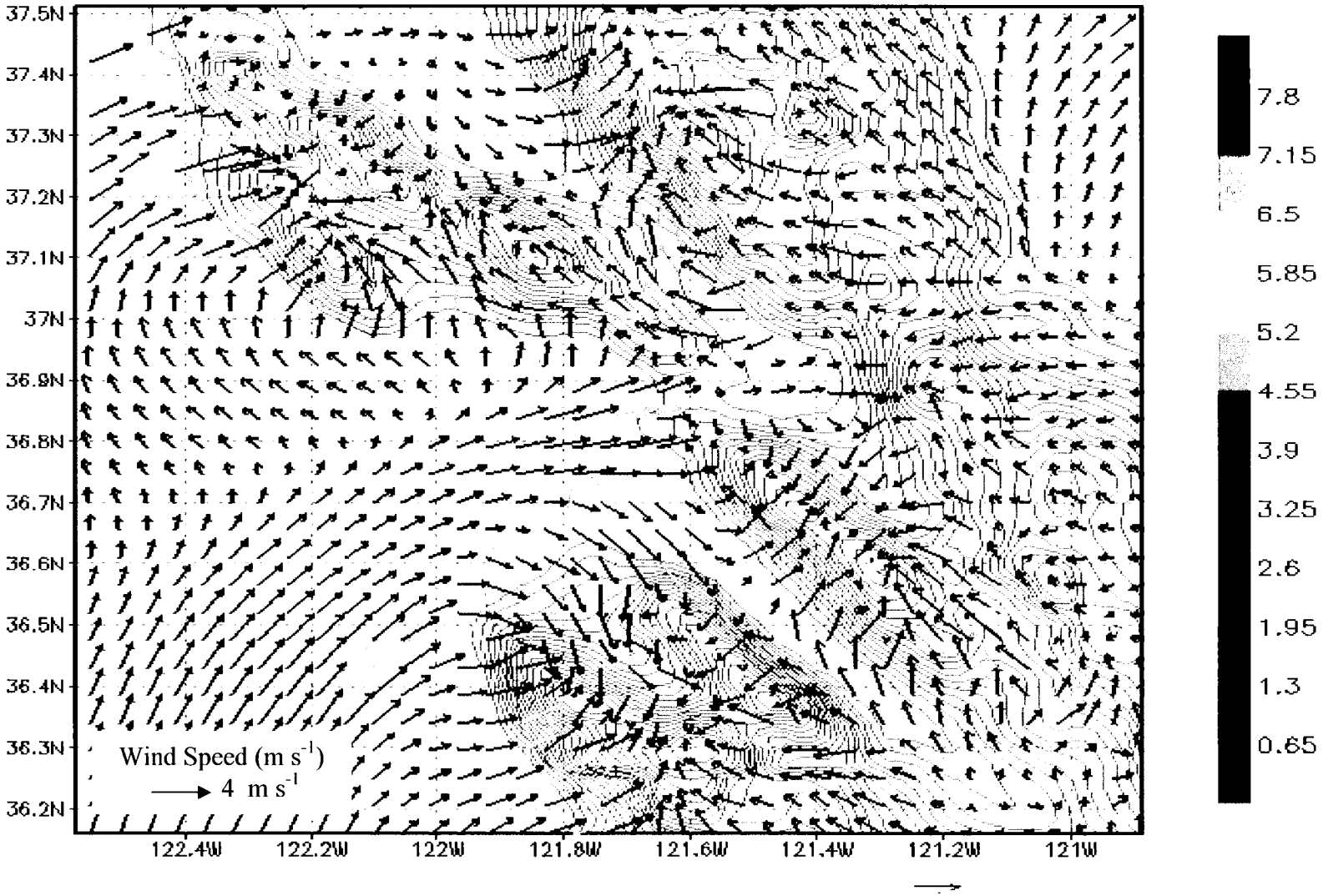


**Fig. 38.** 1000 mb wind field (m $s^{-1}$) 2000 UTC 25 OCT 2003 (Strong offshore case).

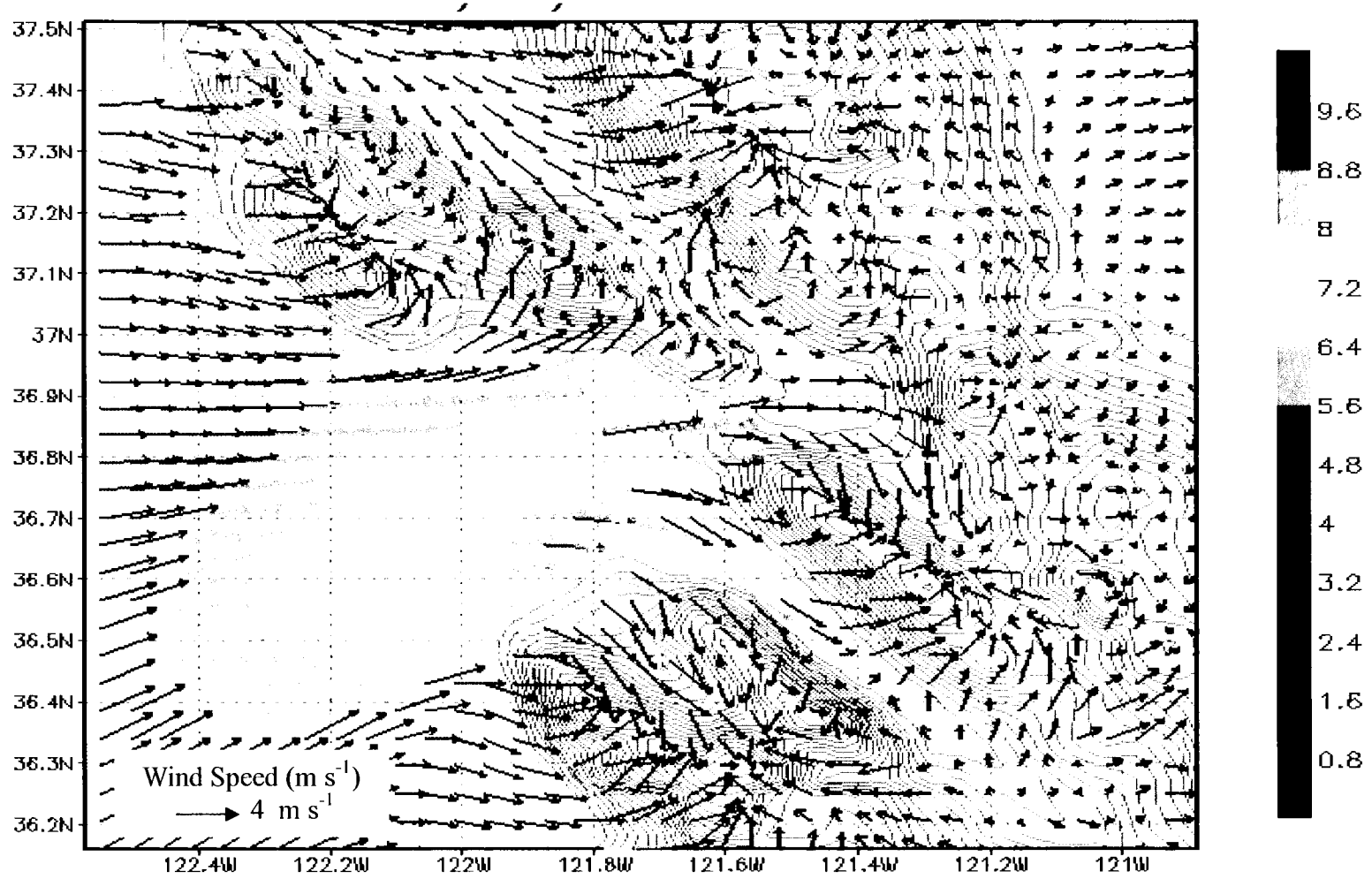


**Fig. 39.** 1000 mb wind field (m $s^{-1}$) 0000 UTC 26 OCT 2003 Strong offshore case).

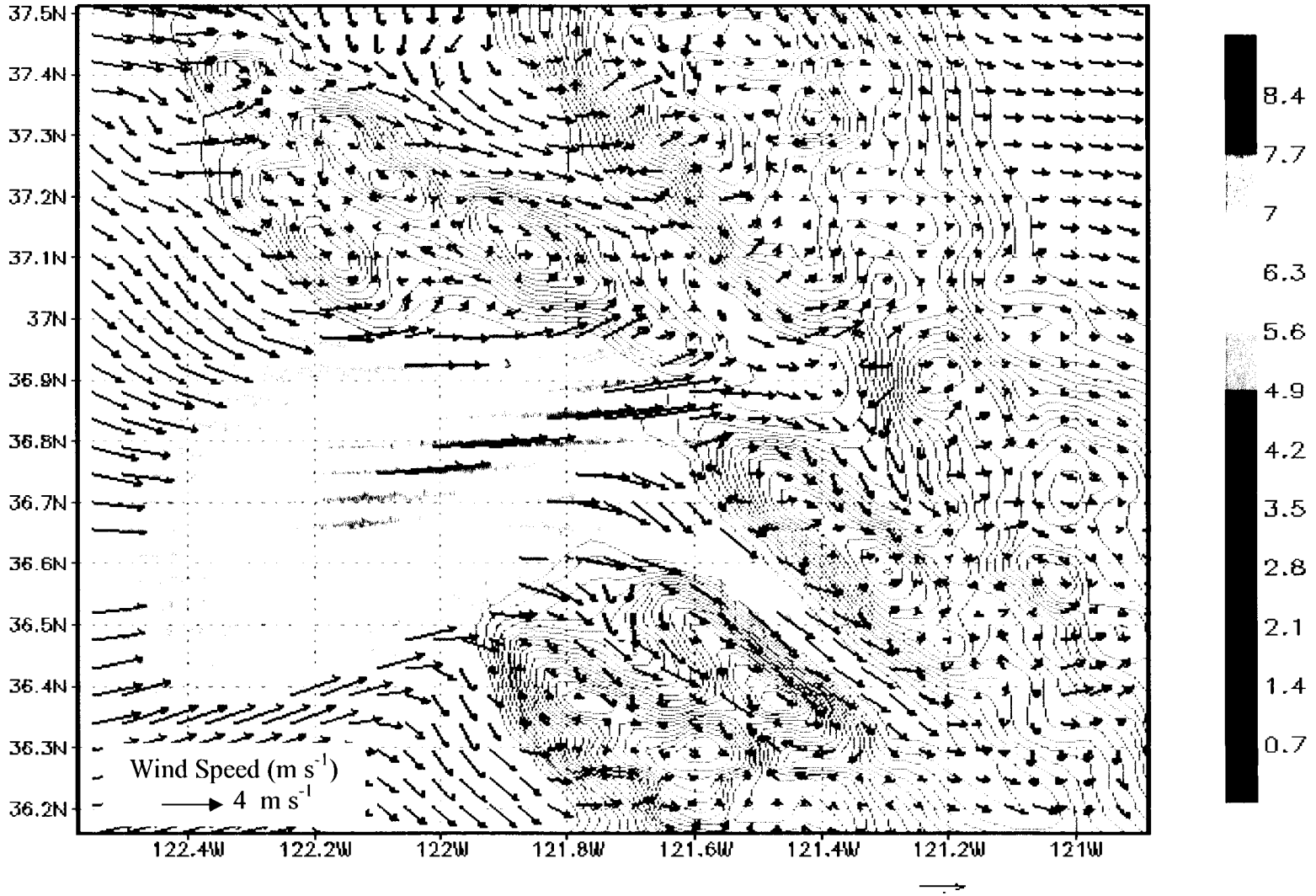


**Fig. 40.** 1000 mb wind field (m $s^{-1}$) 0400 UTC 26 OCT 2003 (Strong offshore case).

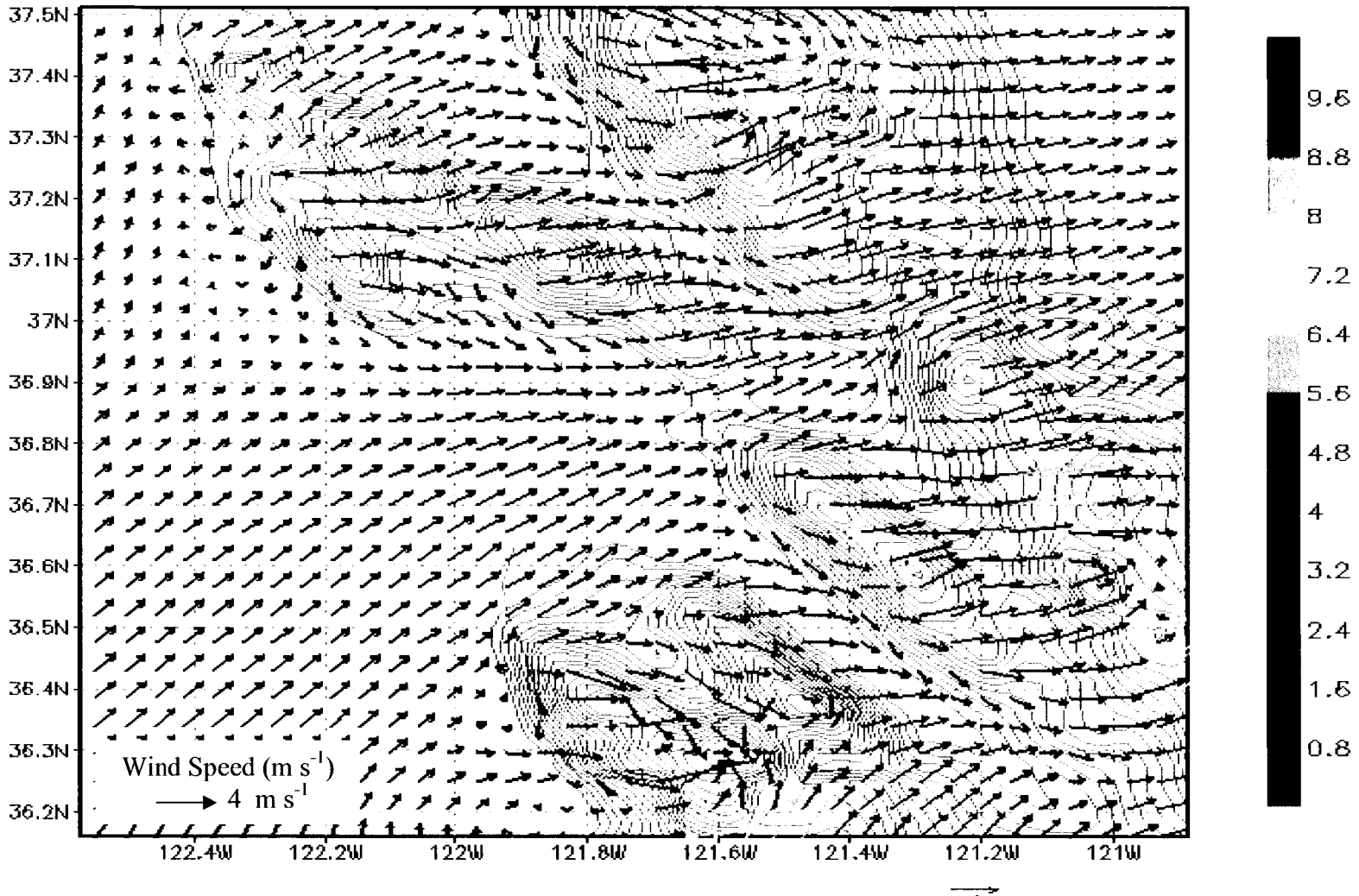


**Fig. 41.** 925 mb wind field (m $s^{-1}$) 0000 UTC 26 OCT 2003 (Strong offshore case).

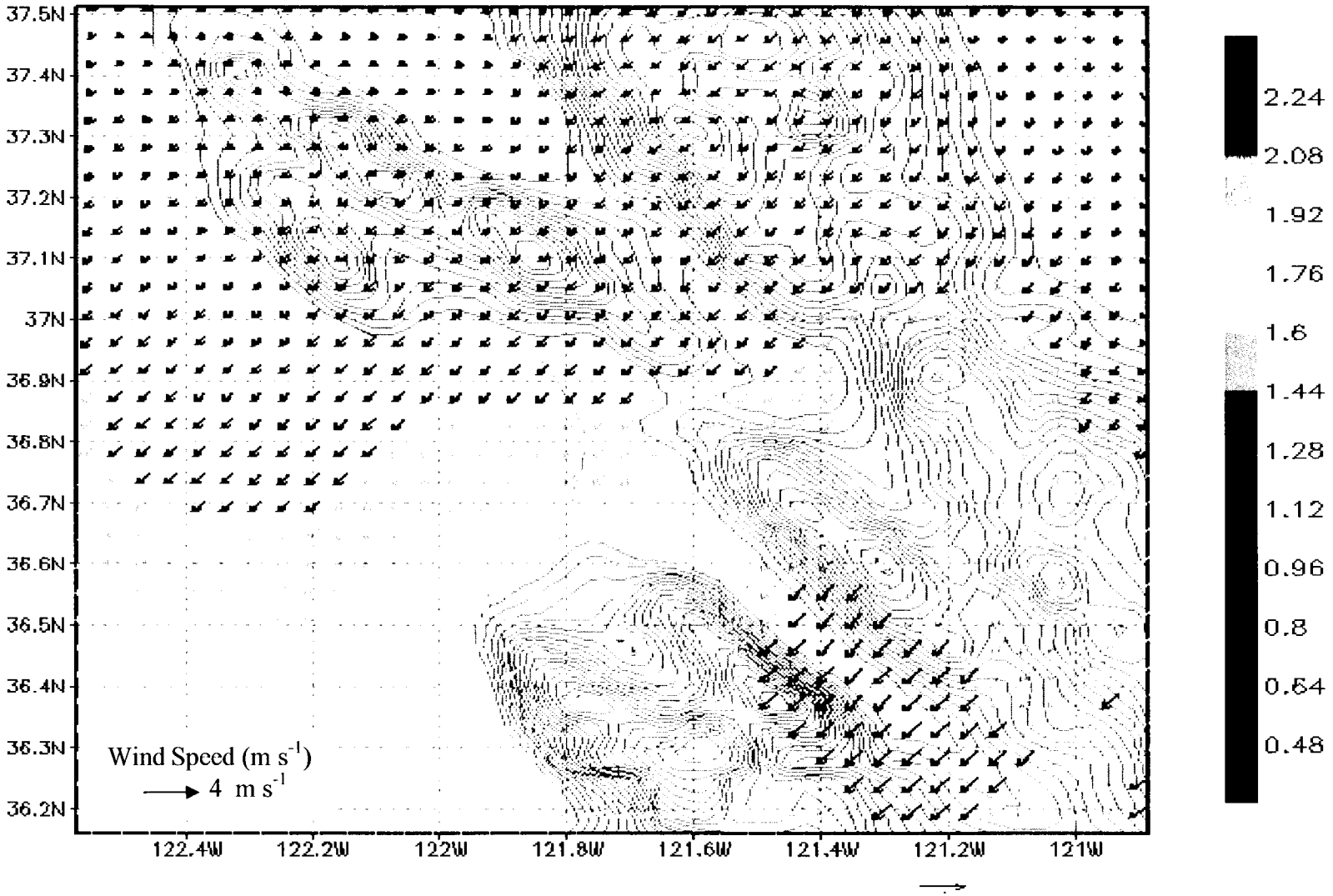


**Fig. 42.** 700 mb wind field (m $s^{-1}$) 0400 UTC 26 OCT 2003 (Strong offshore case).

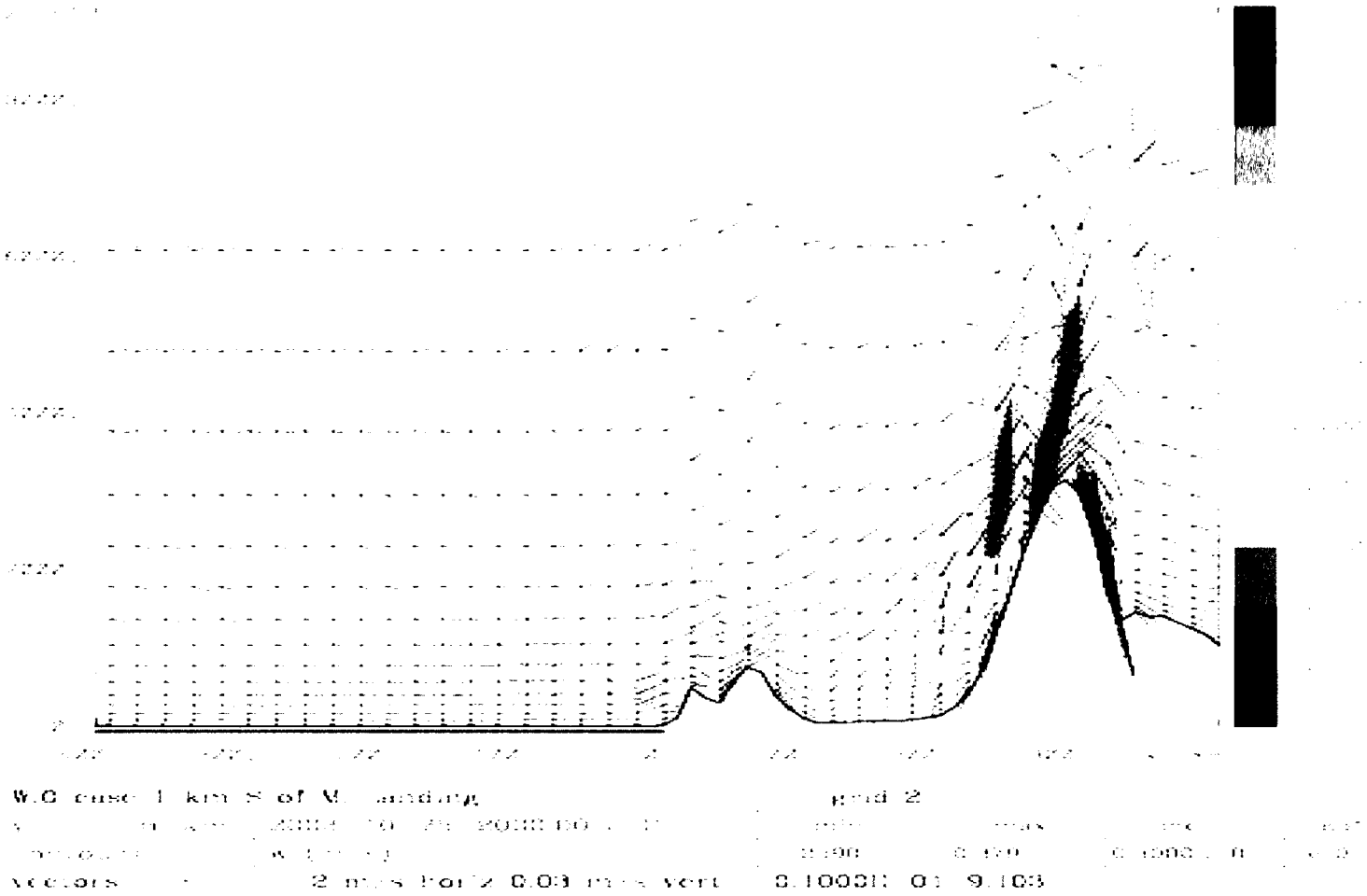

**Fig. 43.** Vertical Slice of wind vector fields and vertical velocity contours for 2000 UTC 25 OCT 2003 (strong offshore case).

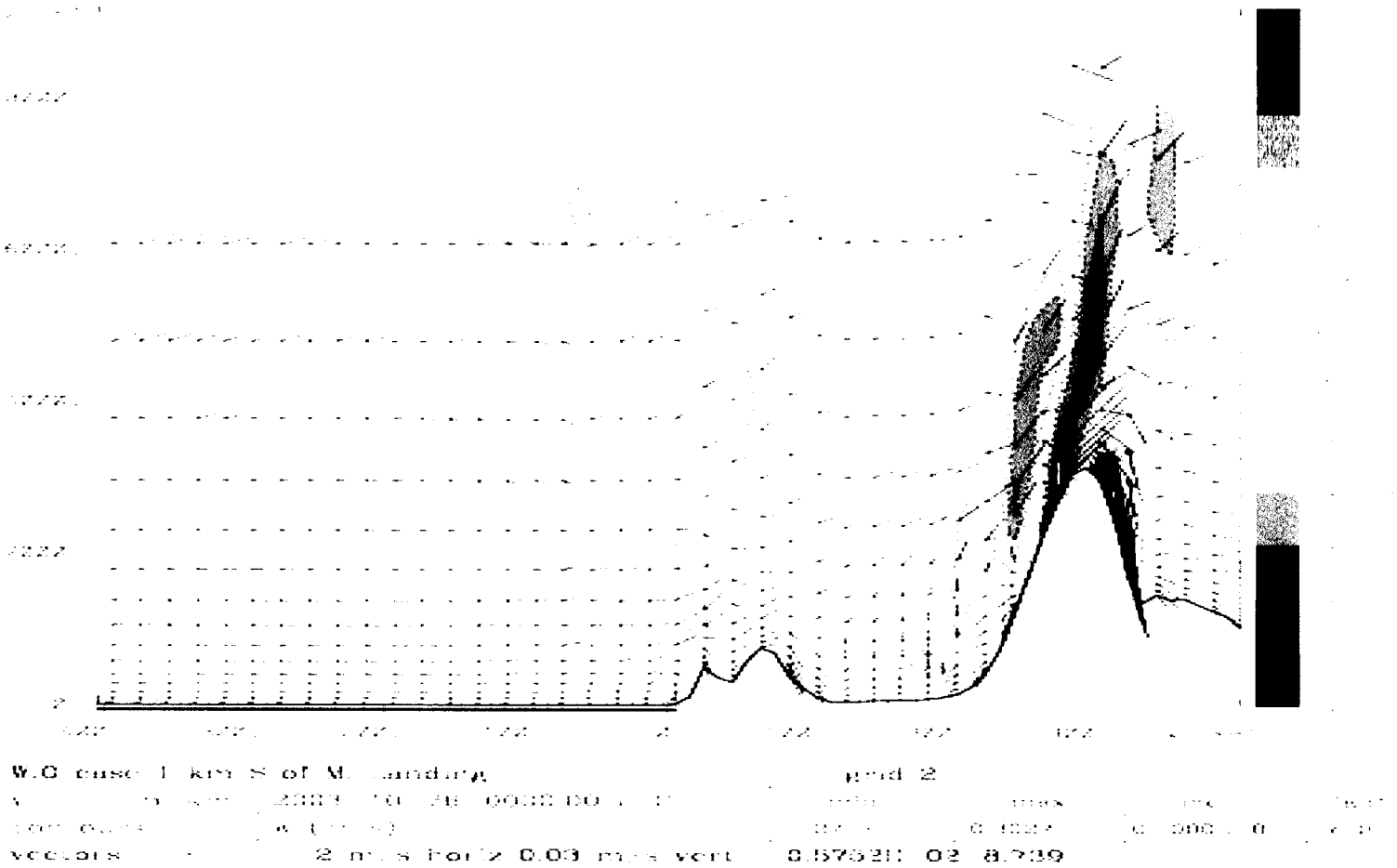

**Fig. 44.** Vertical Slice of wind vector fields and vertical velocity contours for 0000 UTC 26 OCT 2003 (strong offshore case).

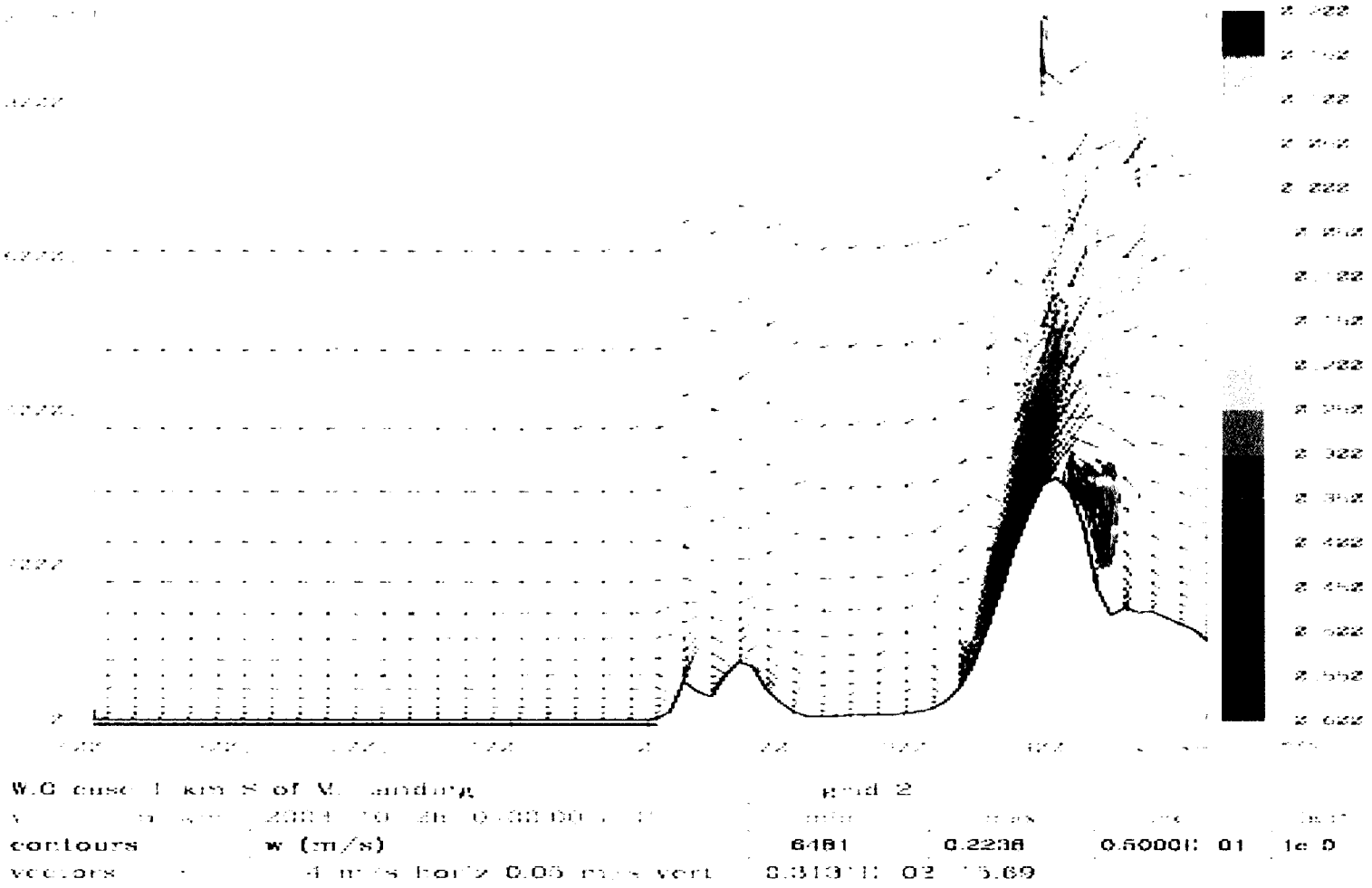


**Fig. 45.** Vertical Slice of wind vector fields and vertical velocity contours for 0400 UTC 26 OCT 2003 (strong offshore case).

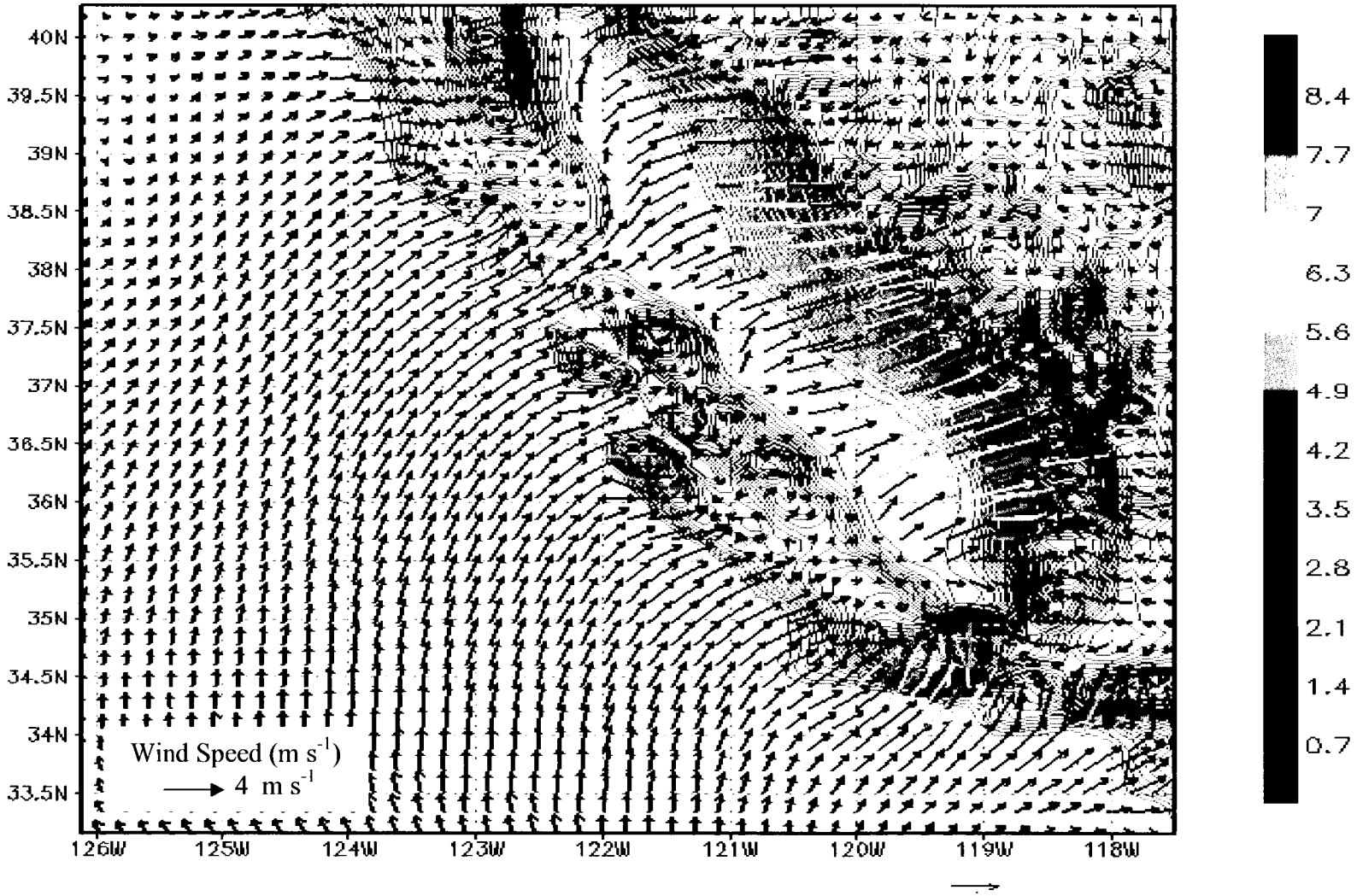


**Fig. 46.** 1000 mb wind field (m $s^{-1}$) 2000 UTC 16 March 2004 (Weak offshore case).

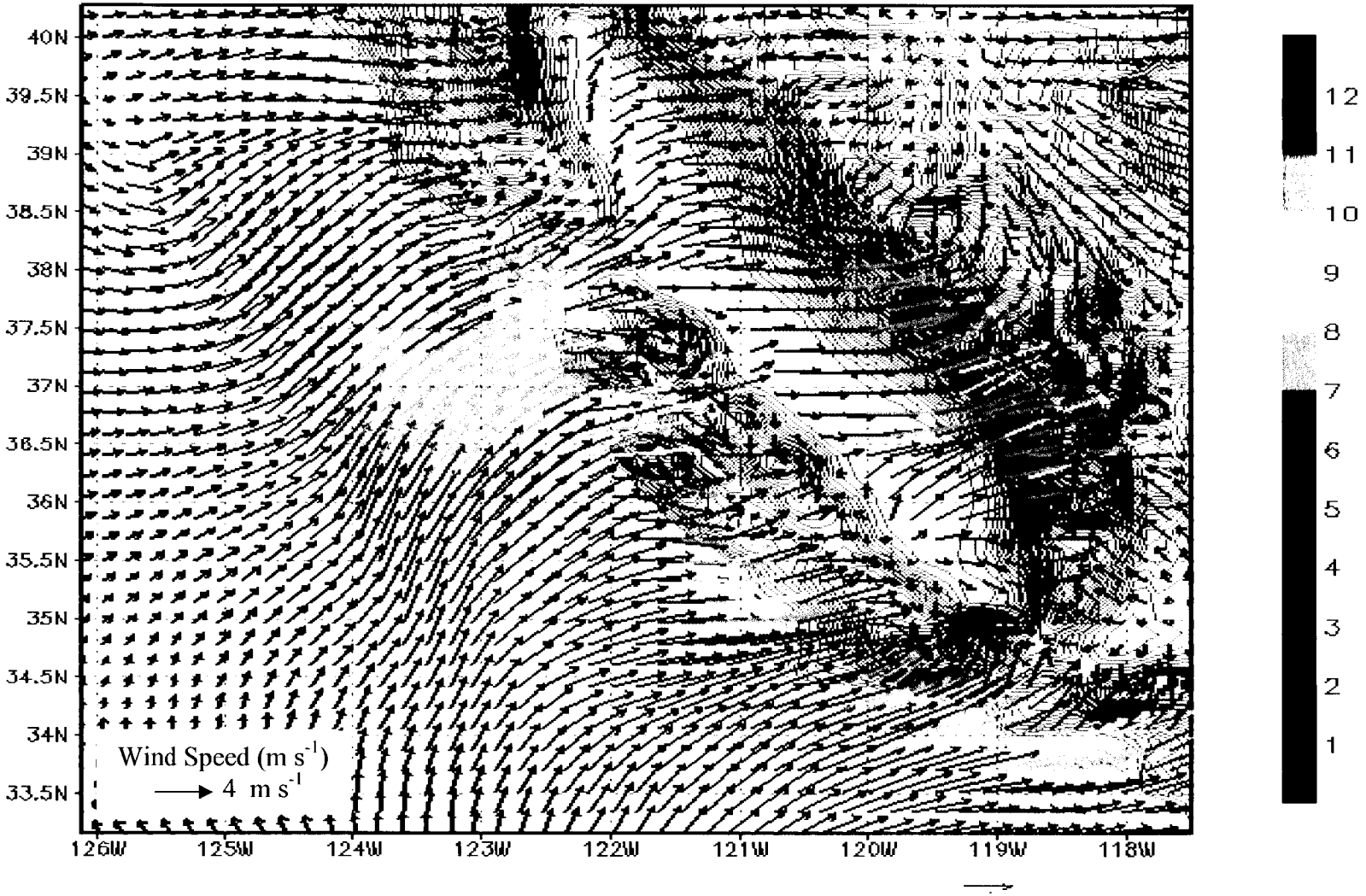


**Fig. 47.** 1000 mb wind field (m $s^{-1}$) 0000 UTC 17 March 2004 (Weak offshore case).

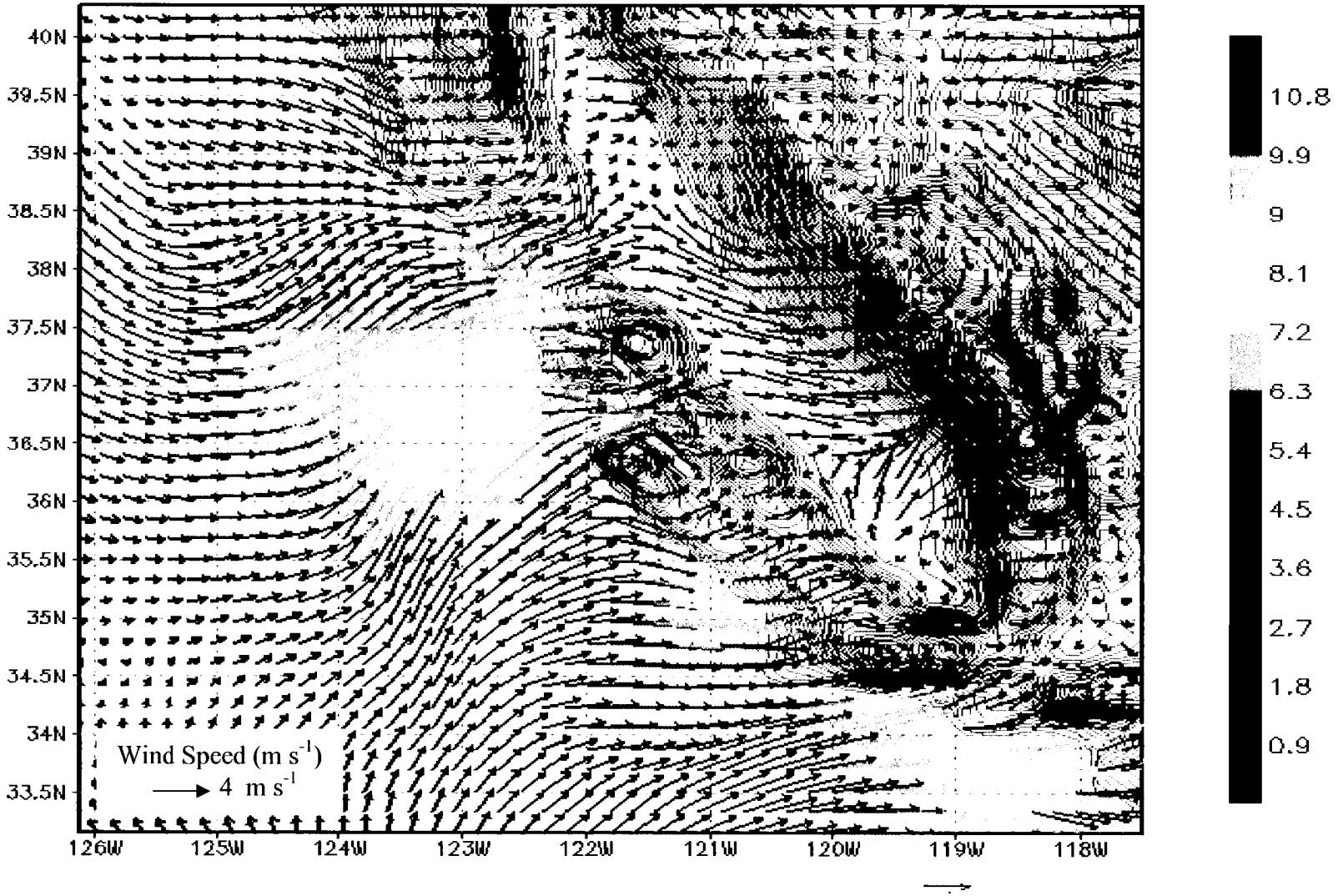


**Fig. 48.** 1000 mb wind field (m $s^{-1}$) 0400 UTC 17 March 2004 (Weak offshore case).

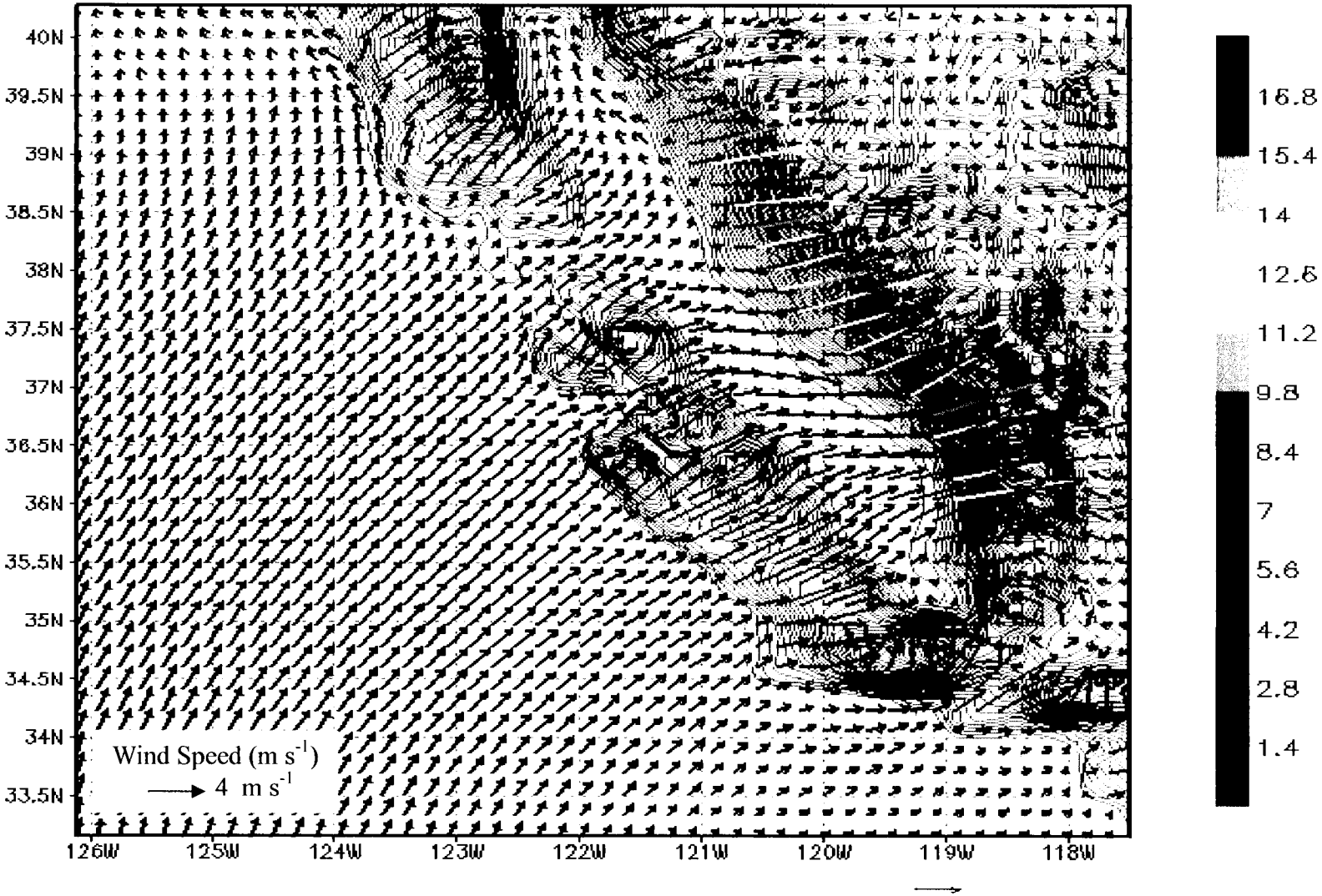


**Fig. 49.** 925 mb wind field (m $s^{-1}$) 2000 UTC 16 March 2004 (Weak offshore case).

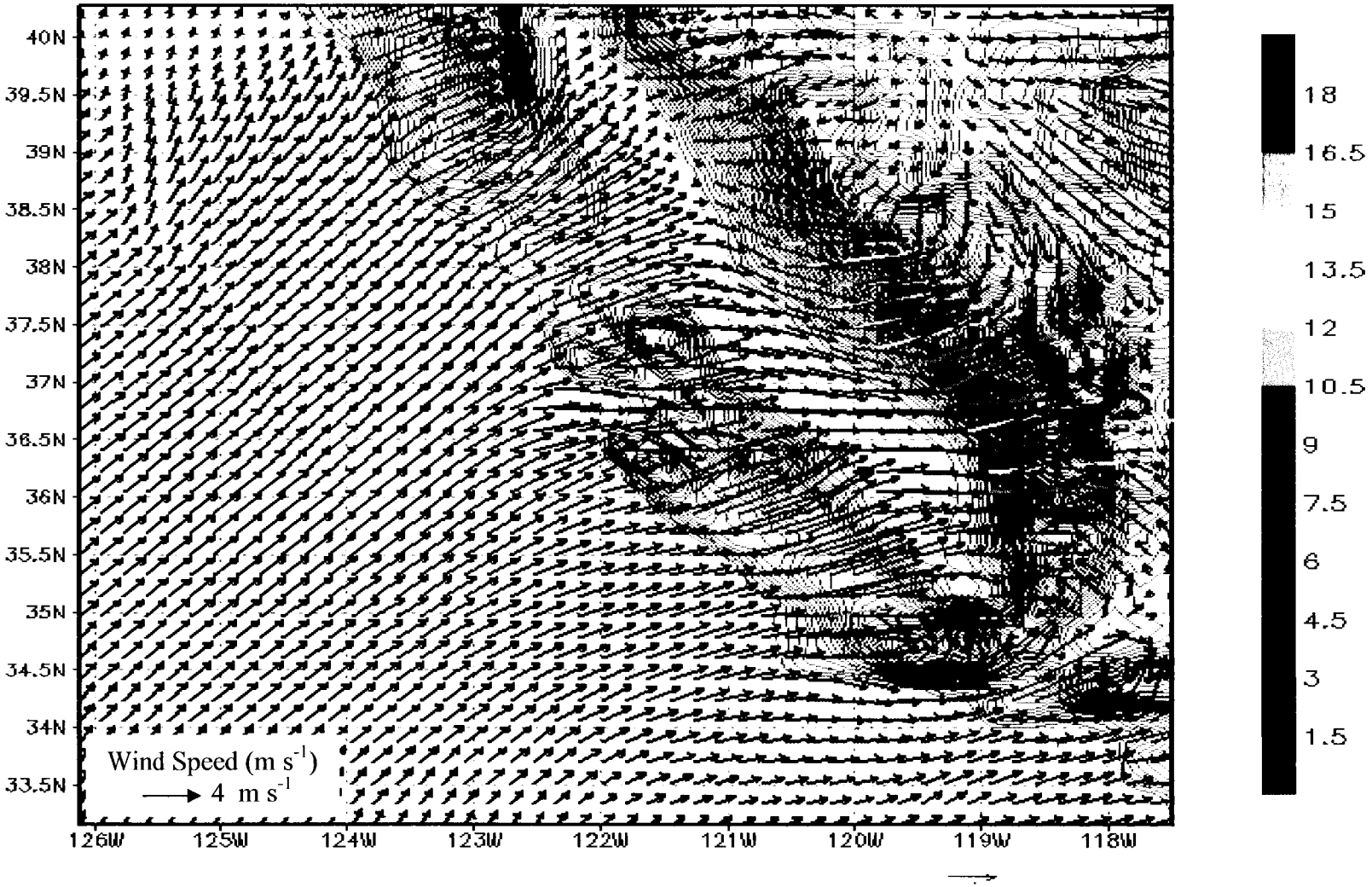


**Fig. 50.** 925 mb wind field (m $s^{-1}$) 0000 UTC 17 March 2004 (Weak offshore case).

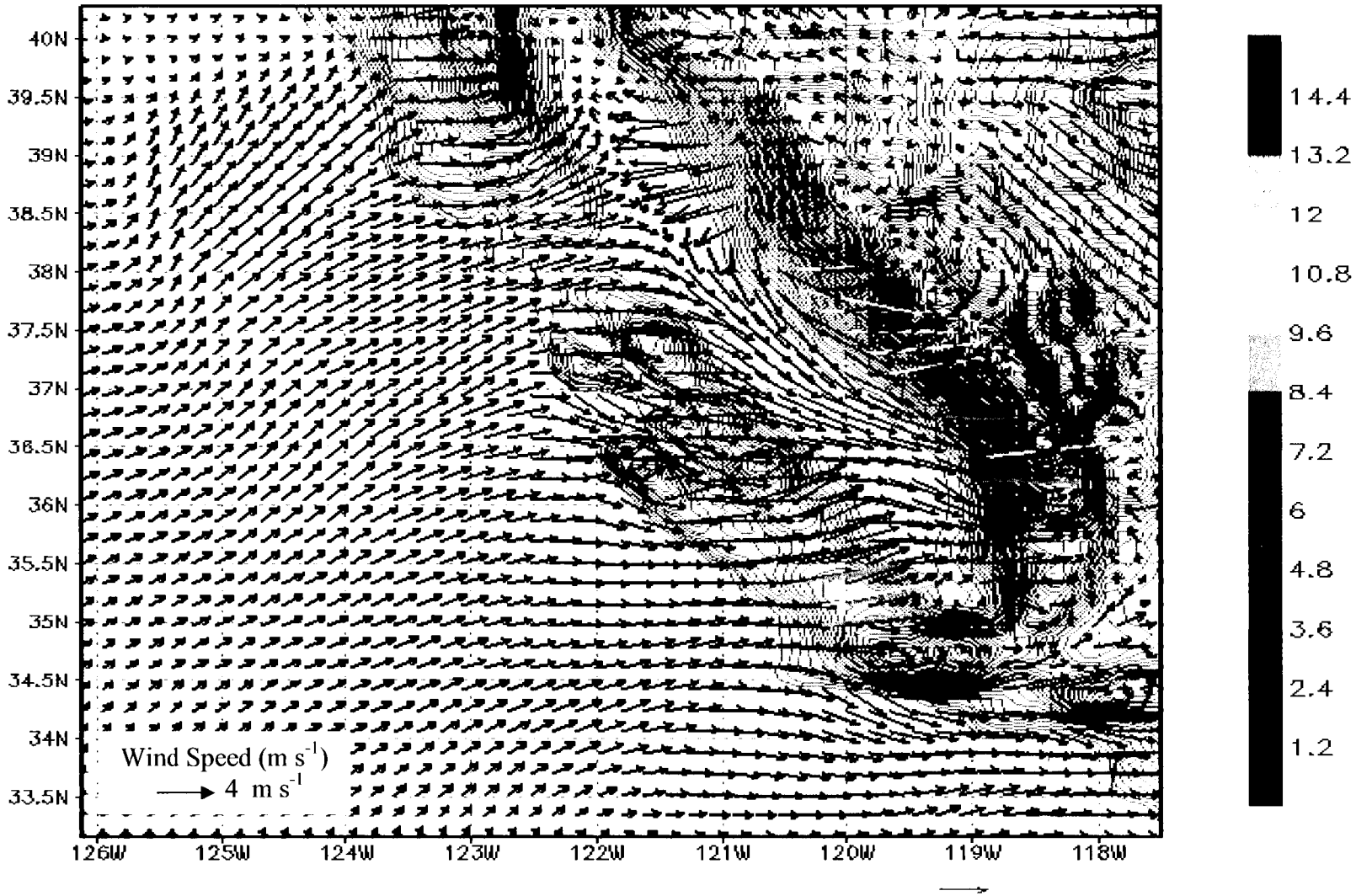


**Fig. 51.** 925 mb wind field (m $s^{-1}$) 0400 UTC 17 March 2004 (Weak offshore case).

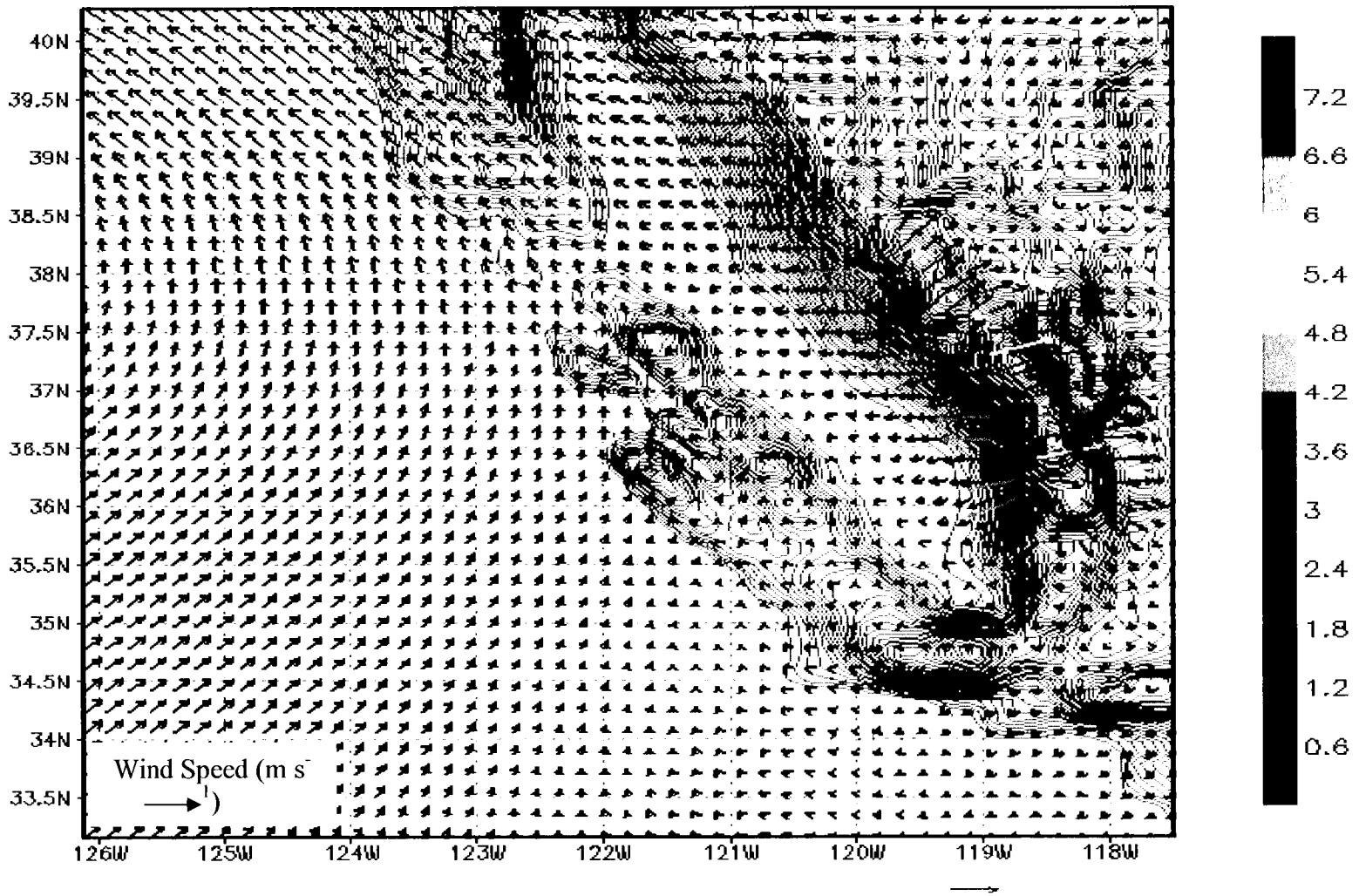


**Fig. 52.** 700 mb wind field (m $s^{-1}$) 2000 UTC 16 March 2004 (Weak offshore case).

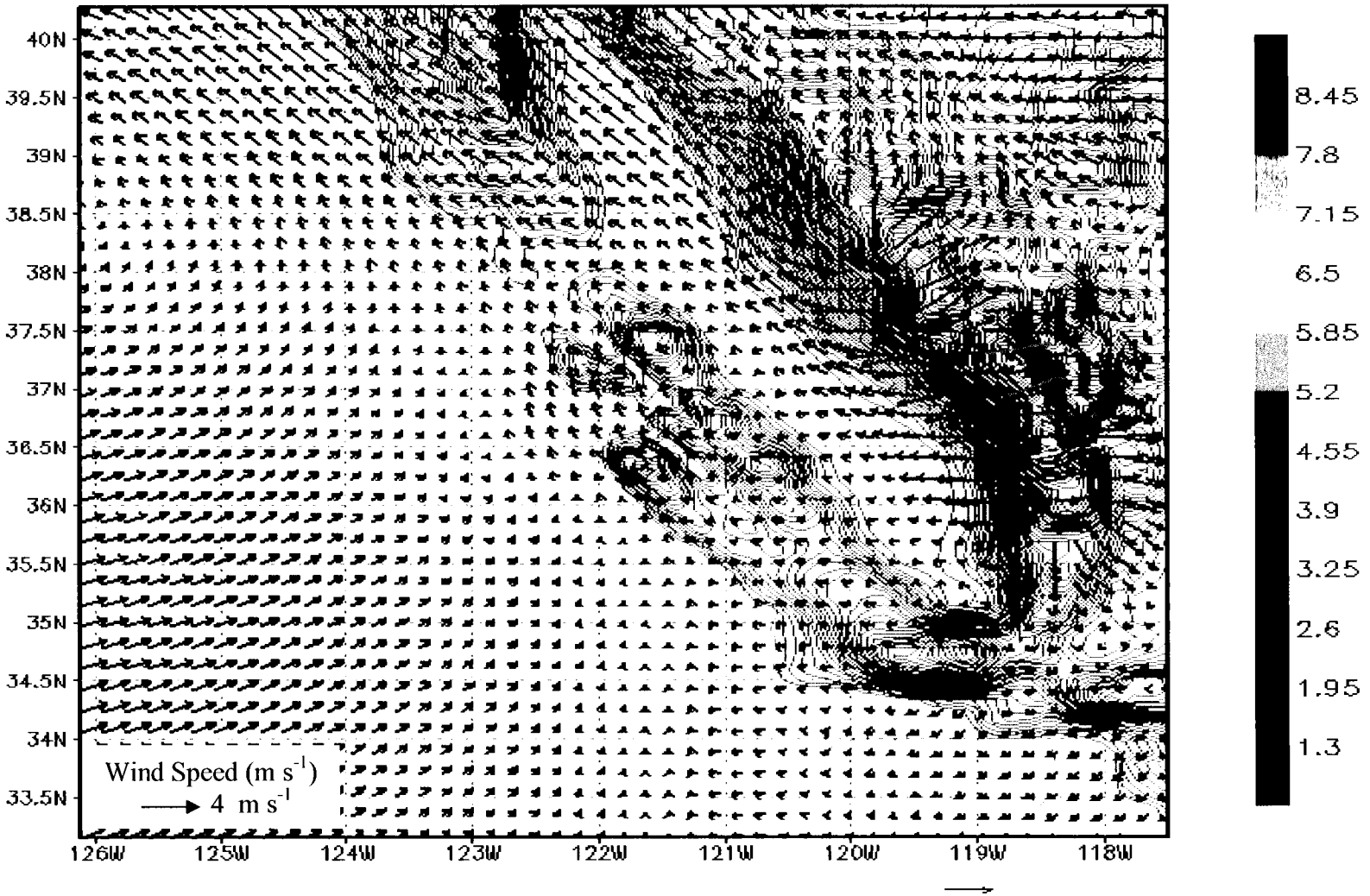


**Fig. 53.** 700 mb wind field (m $s^{-1}$) 0000 UTC 17 March 2004 (Weak offshore case).


**Fig. 54.** 700 mb wind field (m $s^{-1}$) 0400 UTC 17 March 2004 (Weak offshore case).

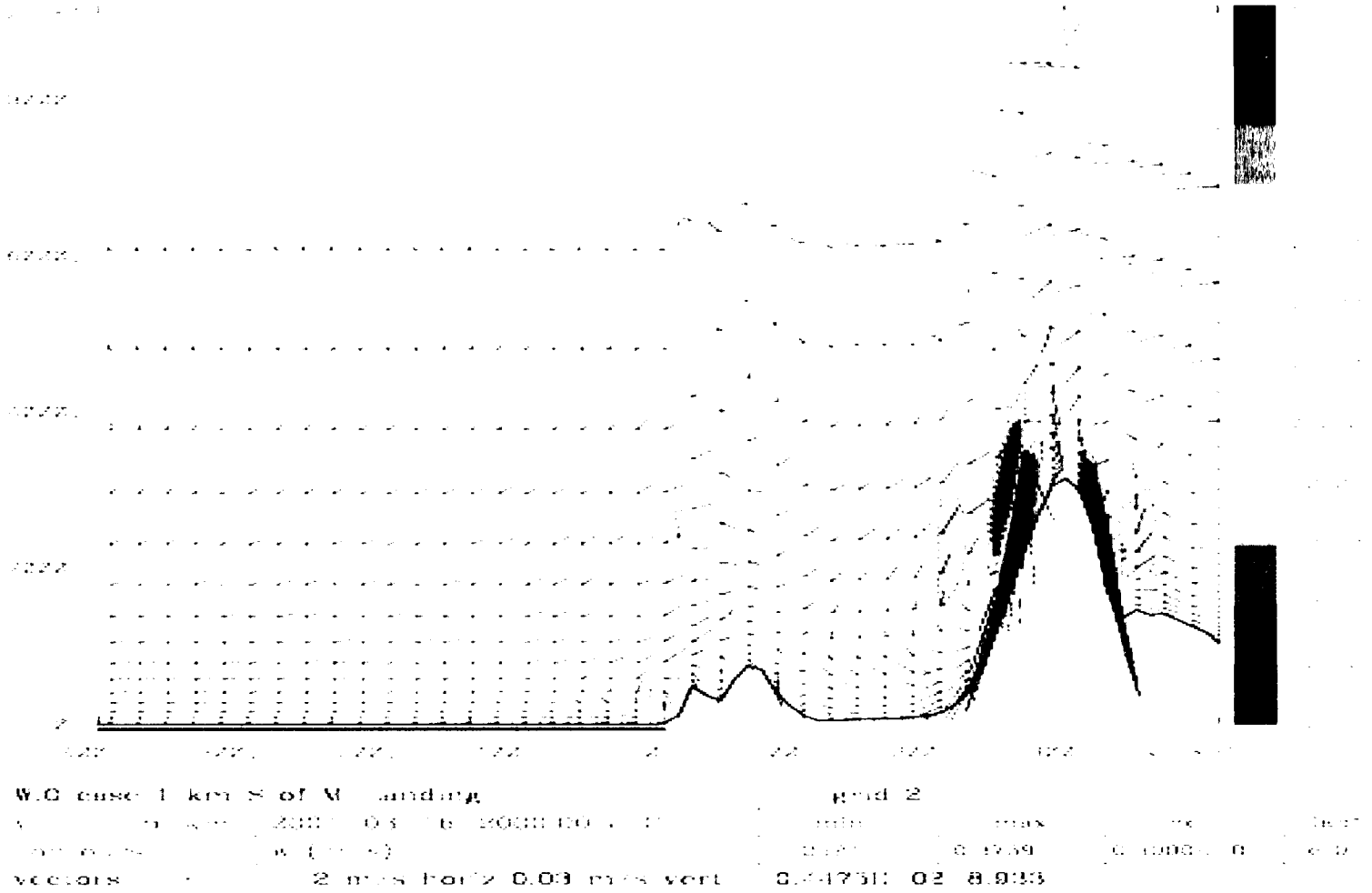

**Fig. 55.** Vertical Slice of wind vector fields and vertical velocity contours for 2000 UTC 16 March 2004 (weak offshore case).

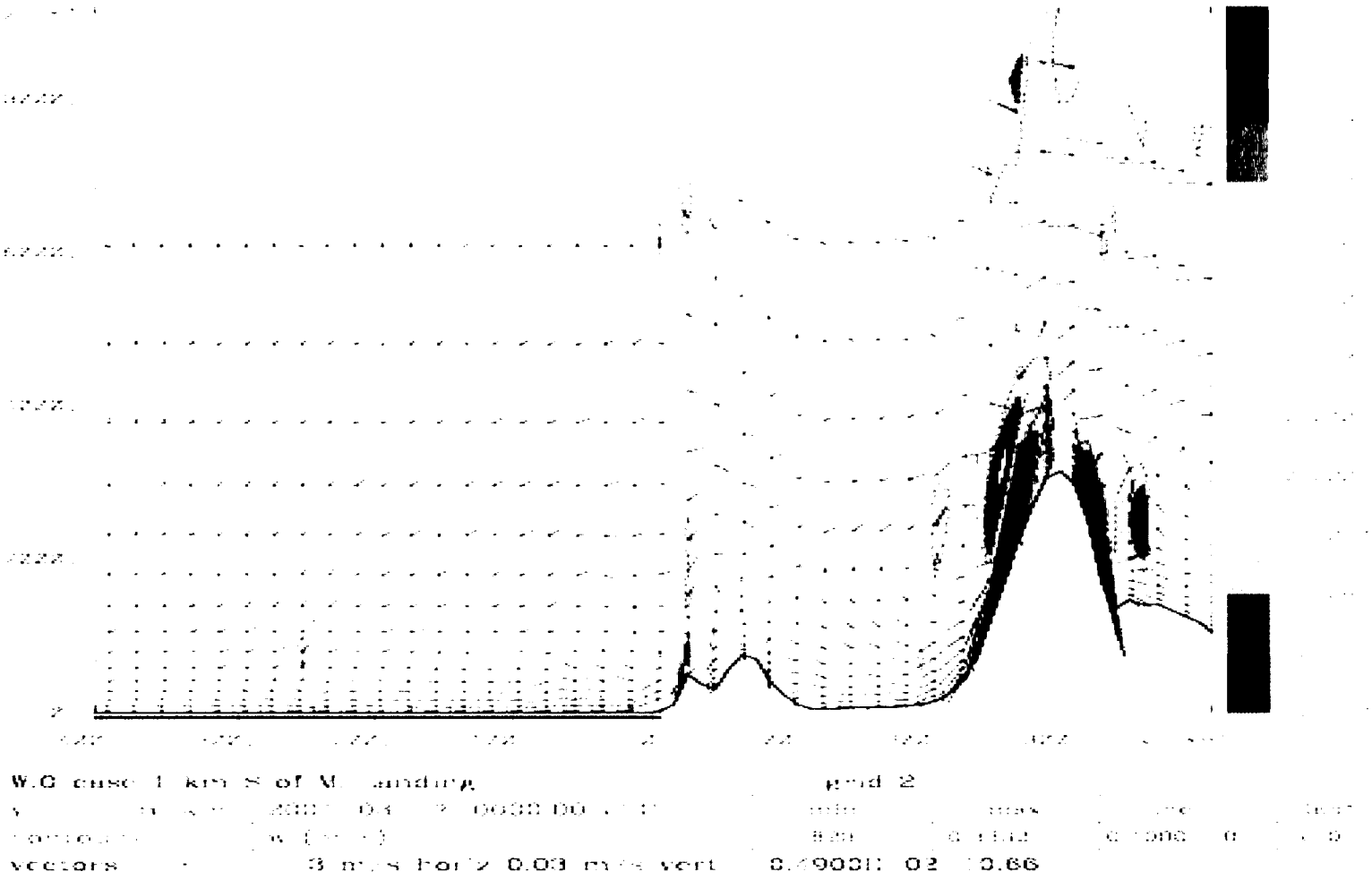

**Fig. 56.** Vertical Slice of wind vector fields and vertical velocity contours for 0000 UTC 17 March 2004 (weak offshore case).

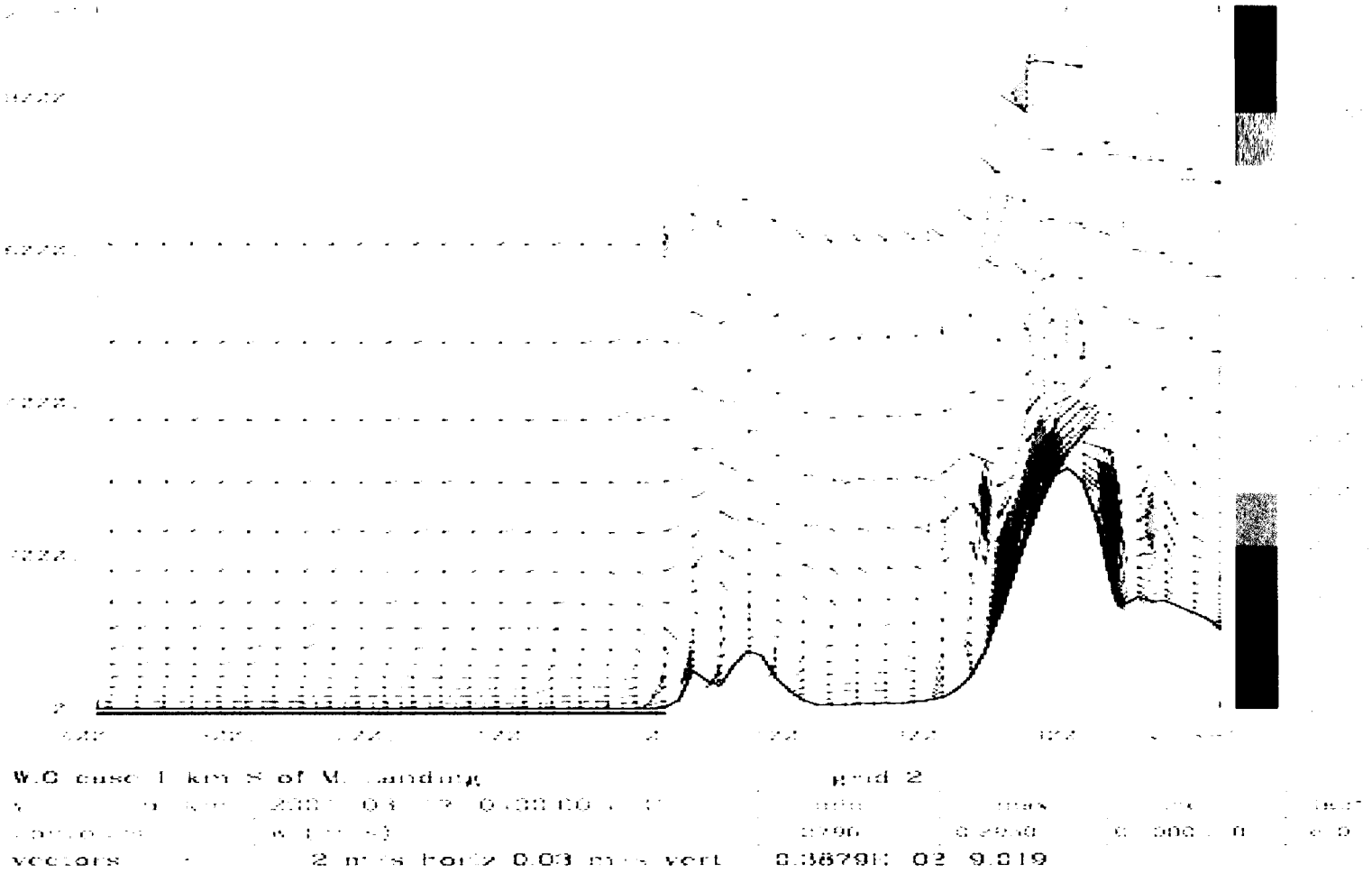

**Fig. 57.** Vertical Slice of wind vector fields and vertical velocity contours for 04000 UTC 17 March 2004 (weak offshore case).

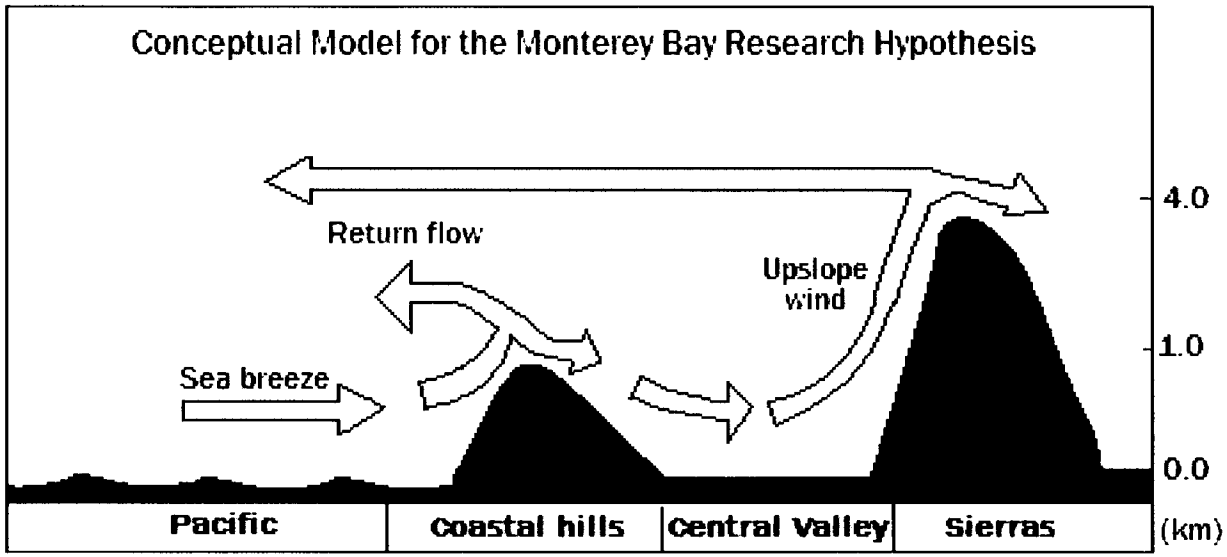


**Fig. 58.** Conceptual model for the Monterey Bay research hypothesis

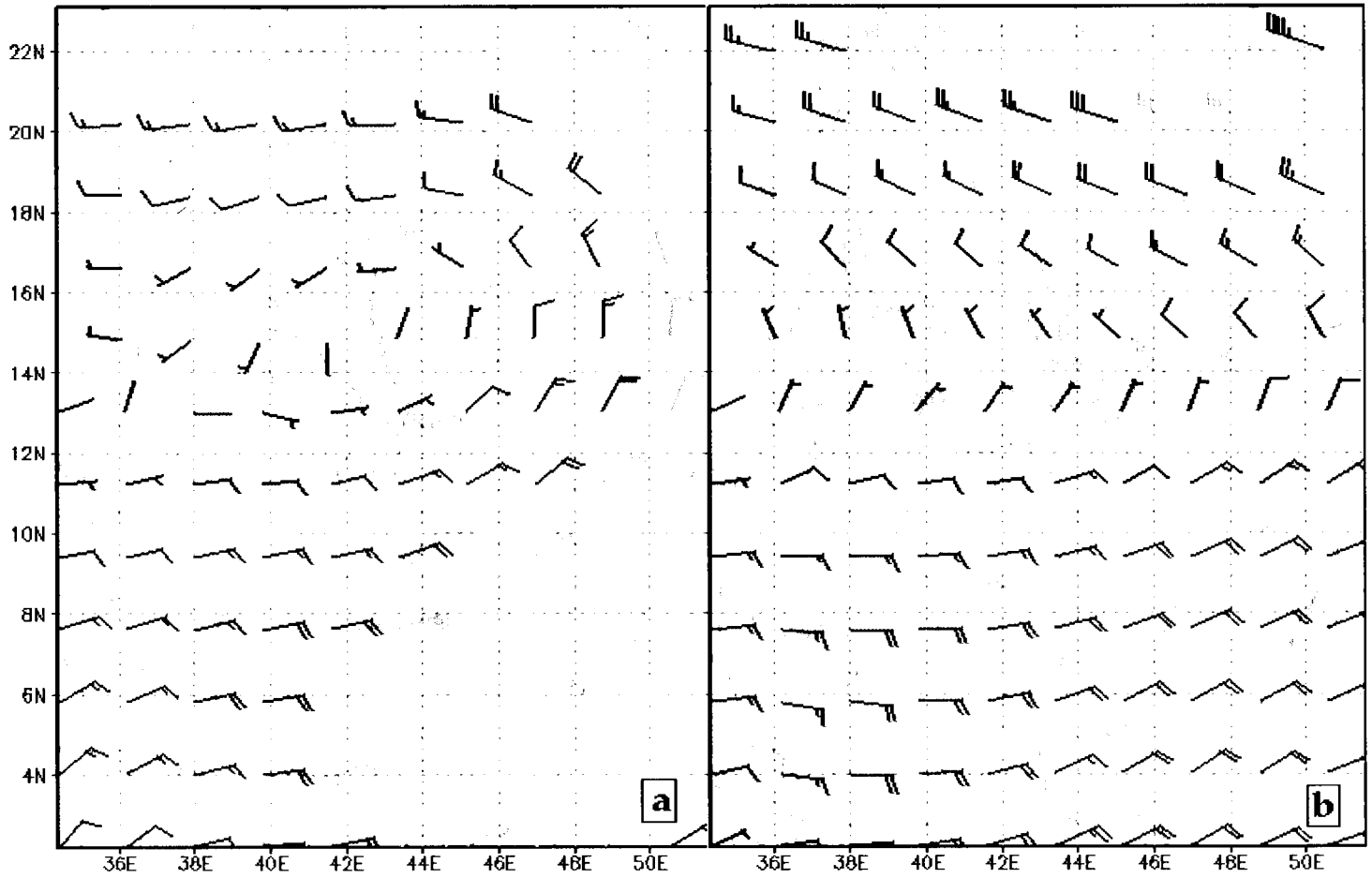


**Fig. 59.** 700 mb, 0000 UTC synoptic analysis maps for Eritrean southern coast (a) 08 February and (b) 09 February 2002.

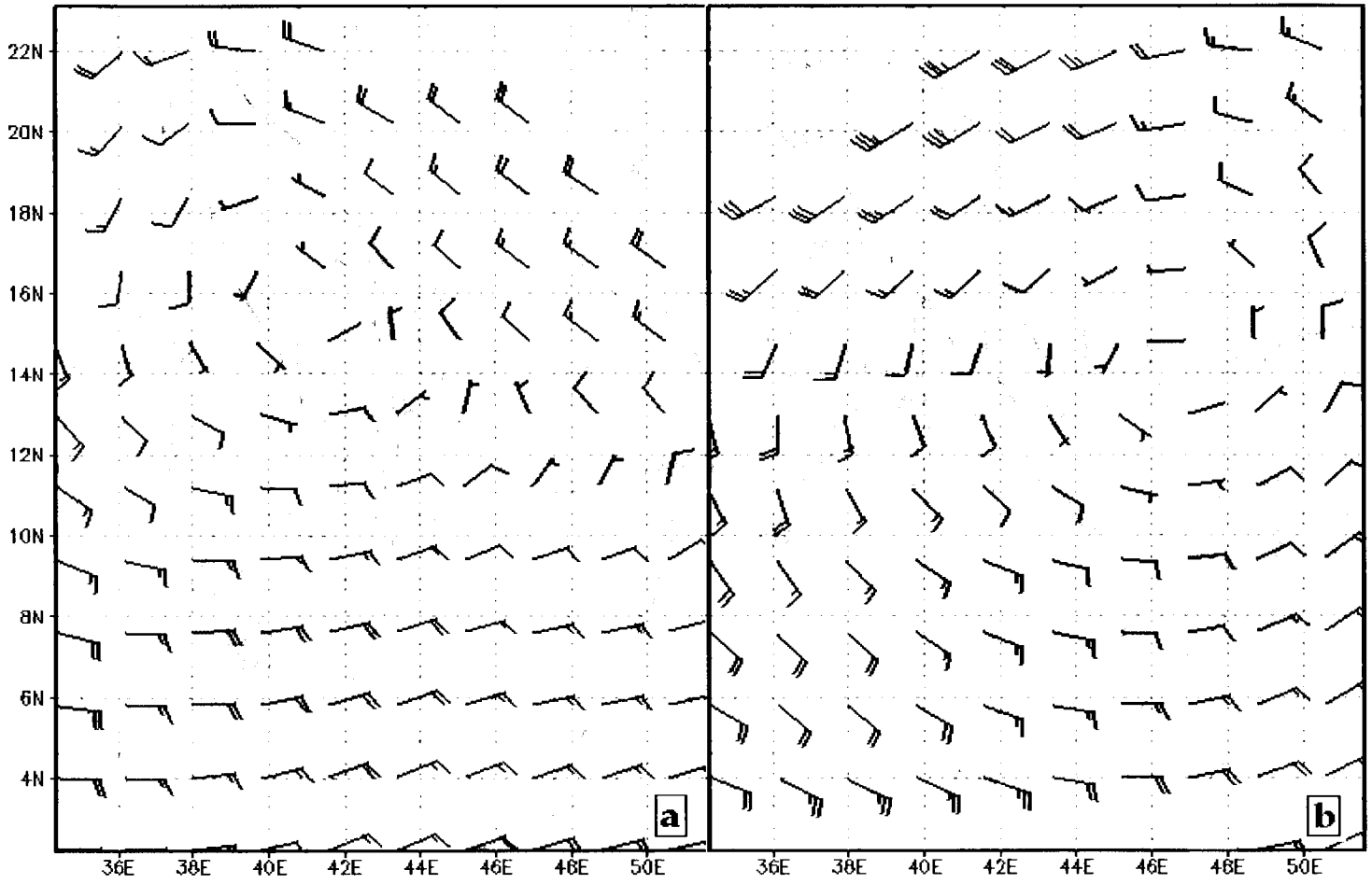


**Fig. 60.** 700 mb, 0000 UTC synoptic analysis maps for Eritrean southern coast (a) 10 February and (b) 11 February 2002.

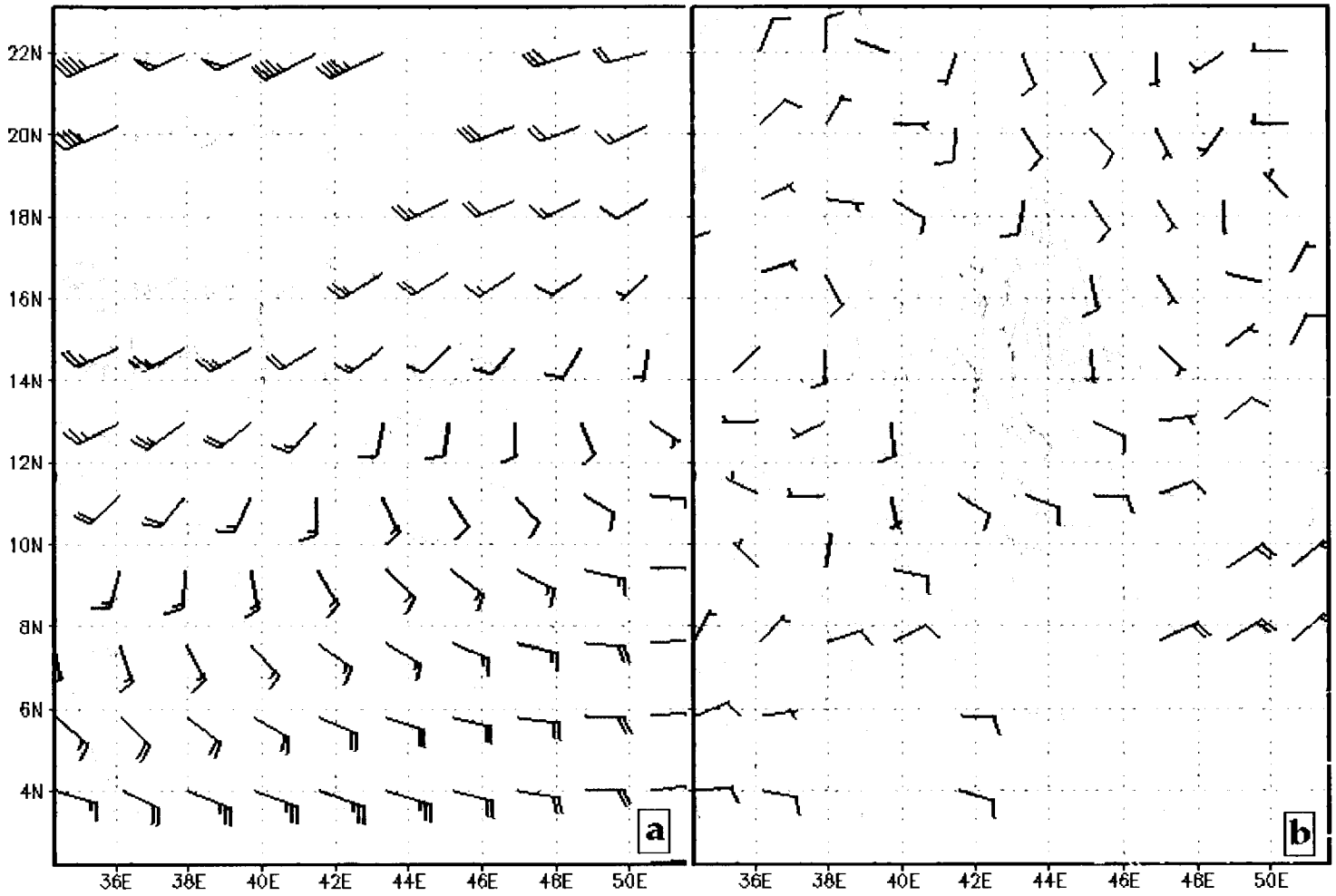


**Fig. 61.** 700 mb, 0000 UTC (a) and 1000 mb, 0000 UTC (b) synoptic analysis maps for Eritrean southern coast (a) 12 February 2002 and (b) 08 February 2002.

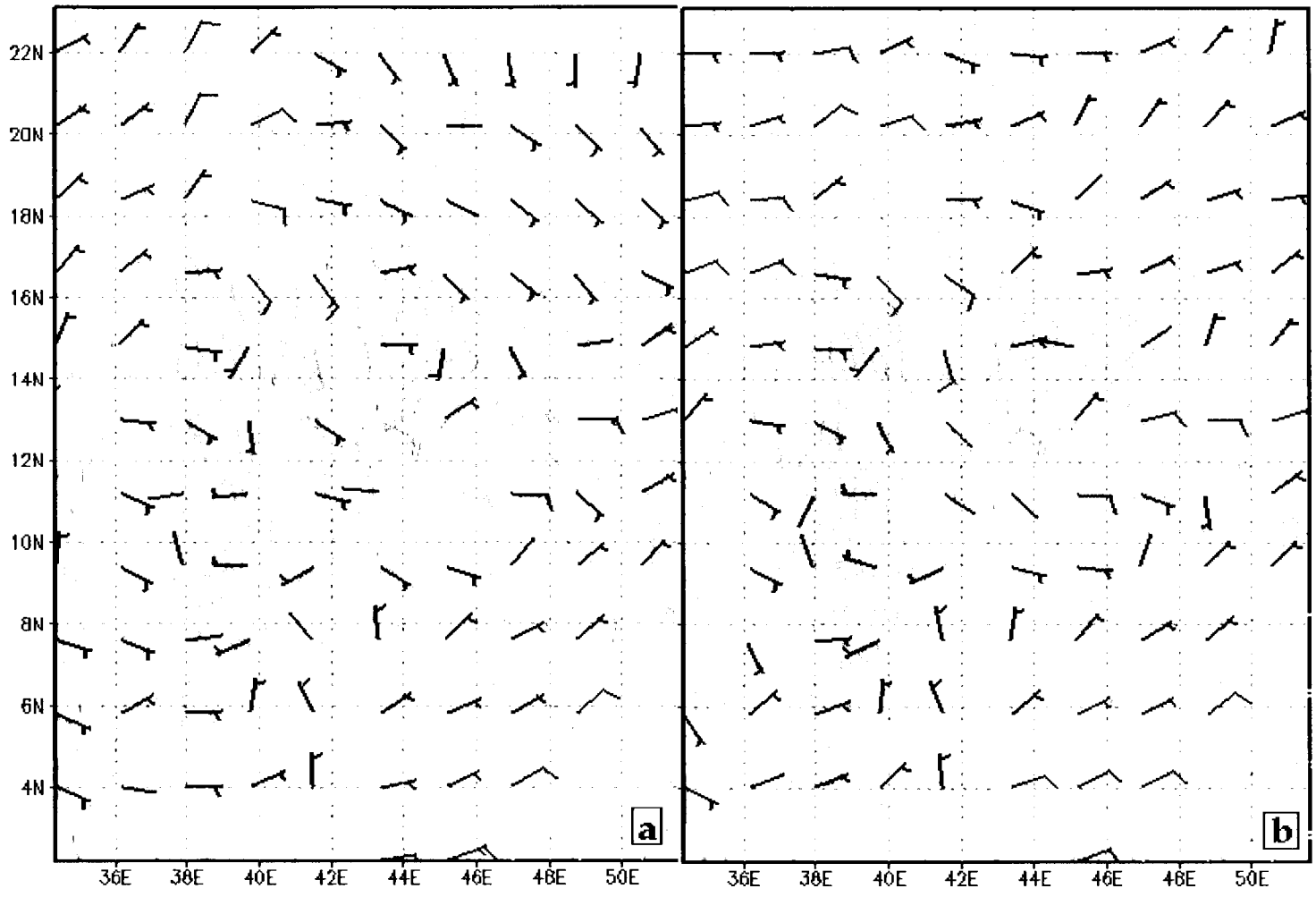


**Fig. 62.** 1000 mb, 0000 UTC synoptic analysis maps for Eritrean southern coast (a) 09 February and (b) 10 February 2002.

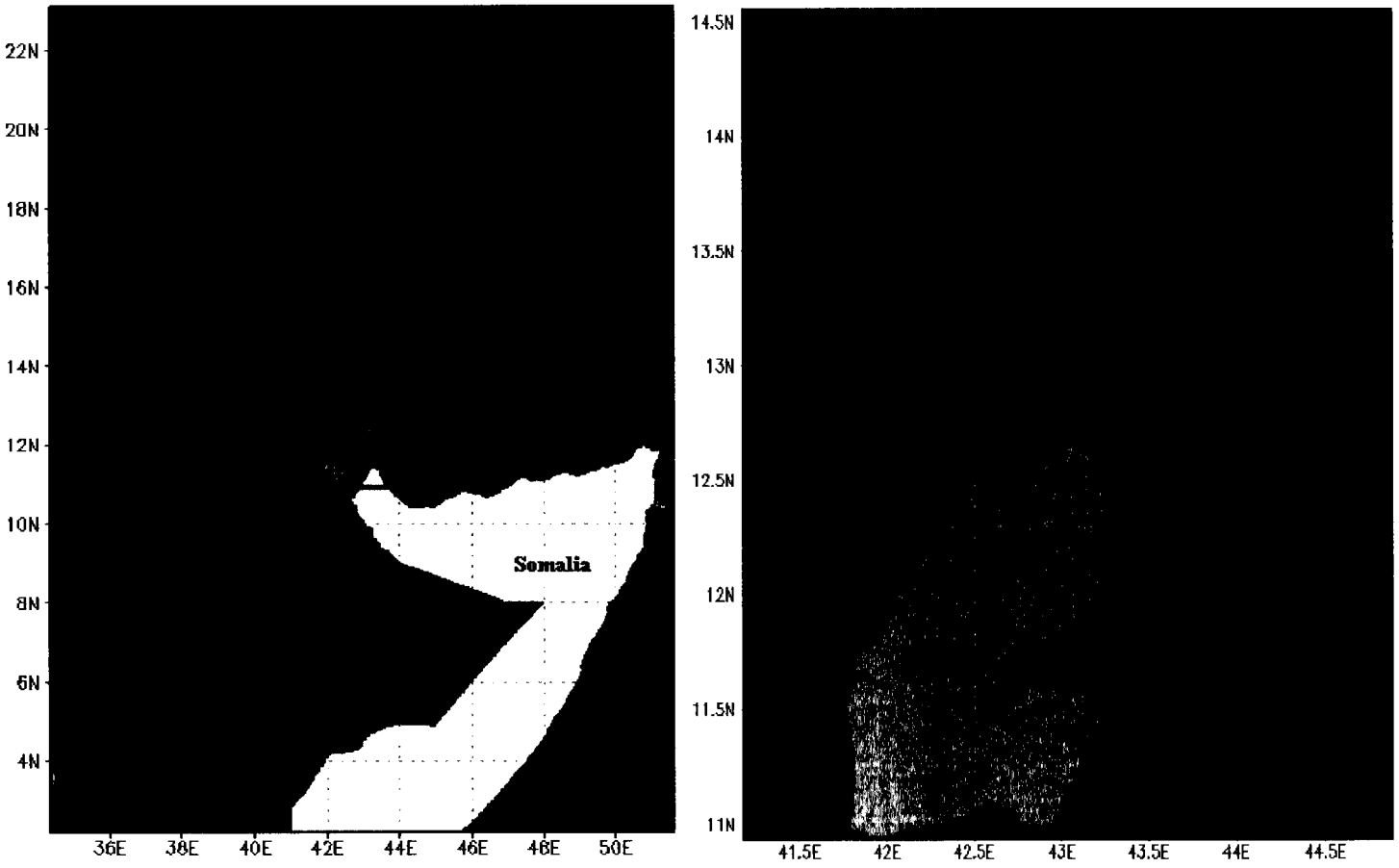


**Fig. 63.** RAMS model grids for the simulation region (a) Nested grids 1,2,3,and 4 and (b) Nested grids 1,2 and 3.

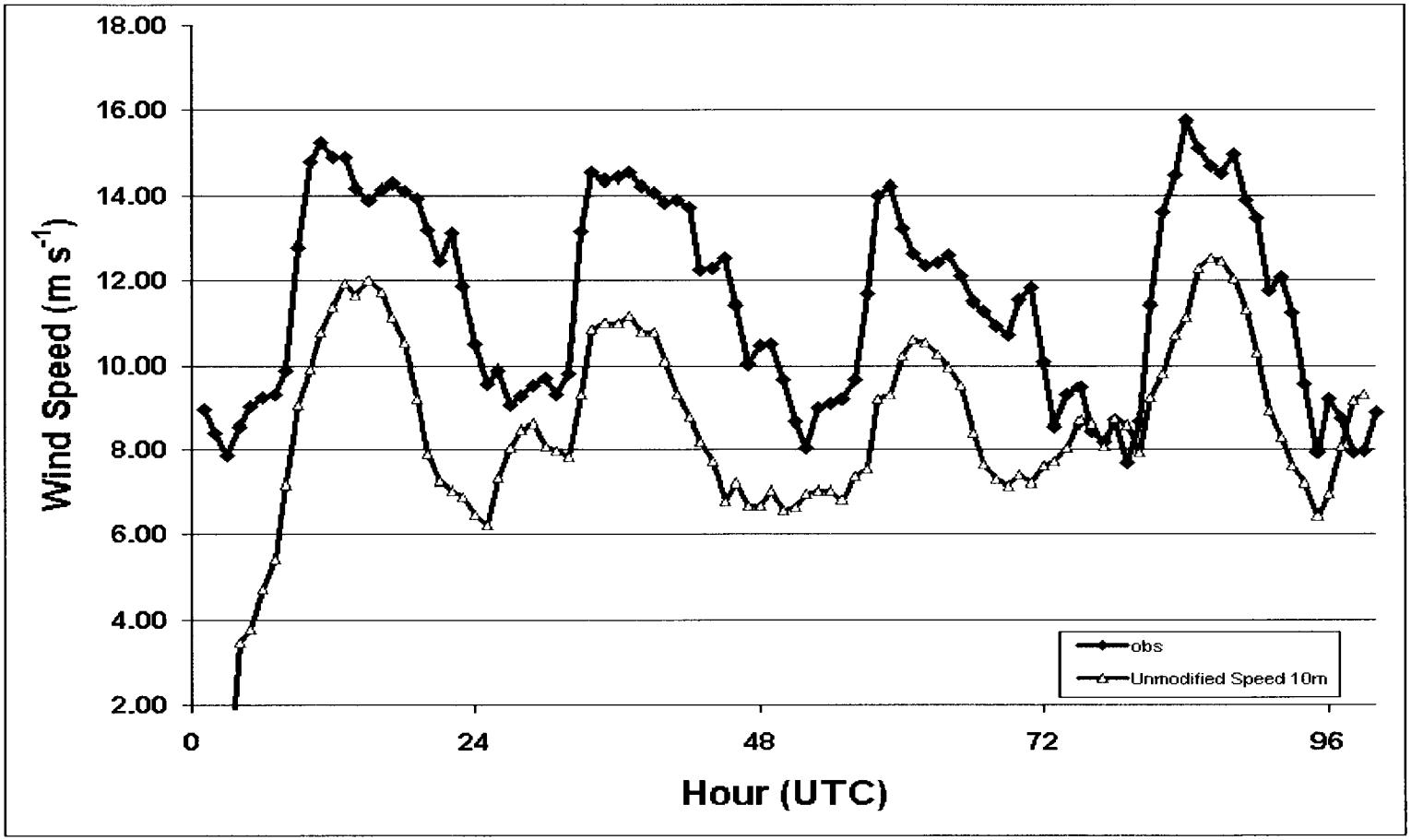


**Fig. 64.** Model (-♦-) vs. observed (-▲-) of 10 m wind speed (m $s^{-1}$) comparison at the station of Aseb Airport (with out roughness adjustment)

**Fig. 65.** Photograph of the Aseb region showing the land scape and the roughness of the land over the topography.

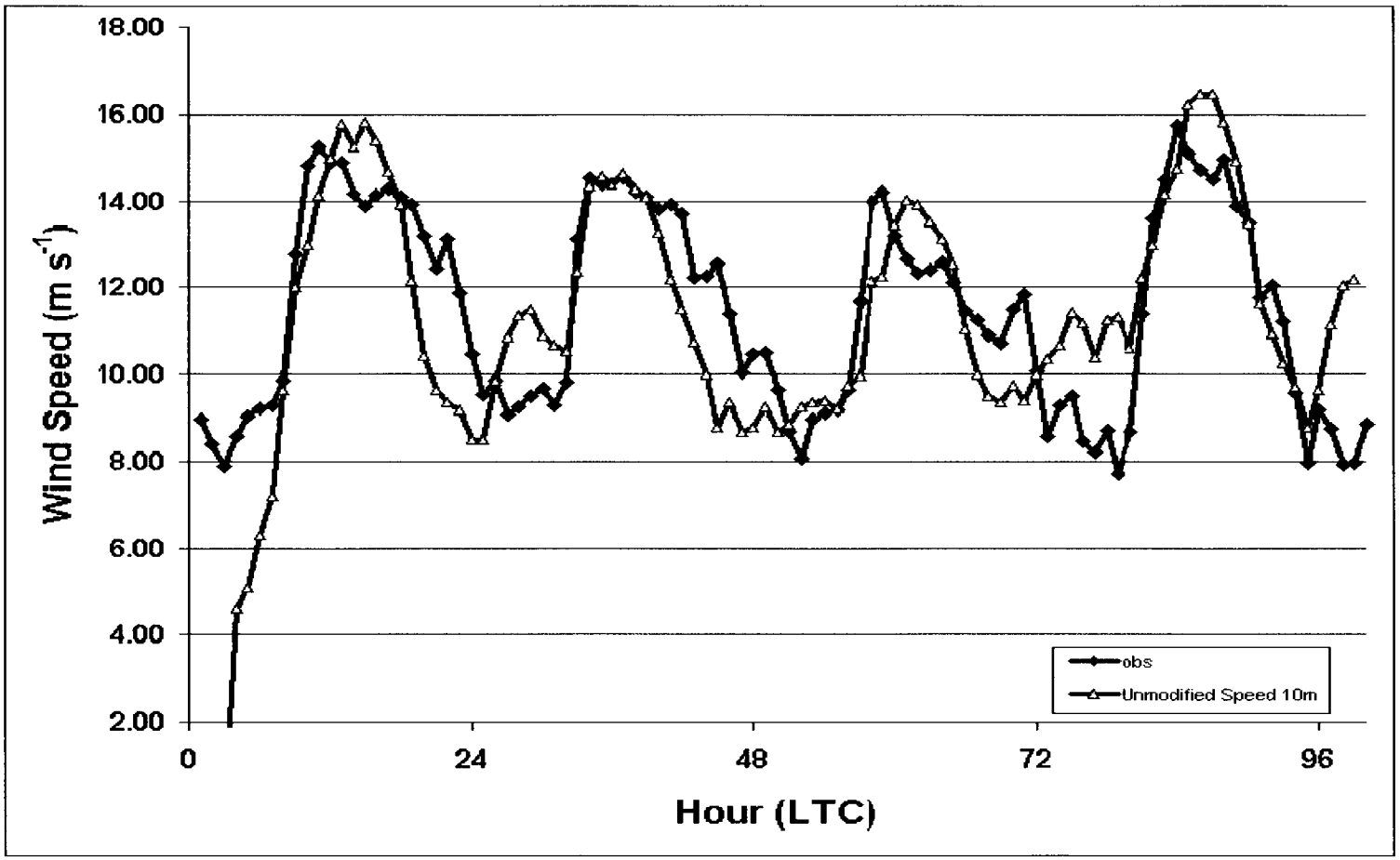


**Fig. 66.** Model (-♦-) vs. observed (-▲-) of 10 m wind speed (m $s^{-1}$) comparison at the station of Aseb Airport (with roughness adjustment)

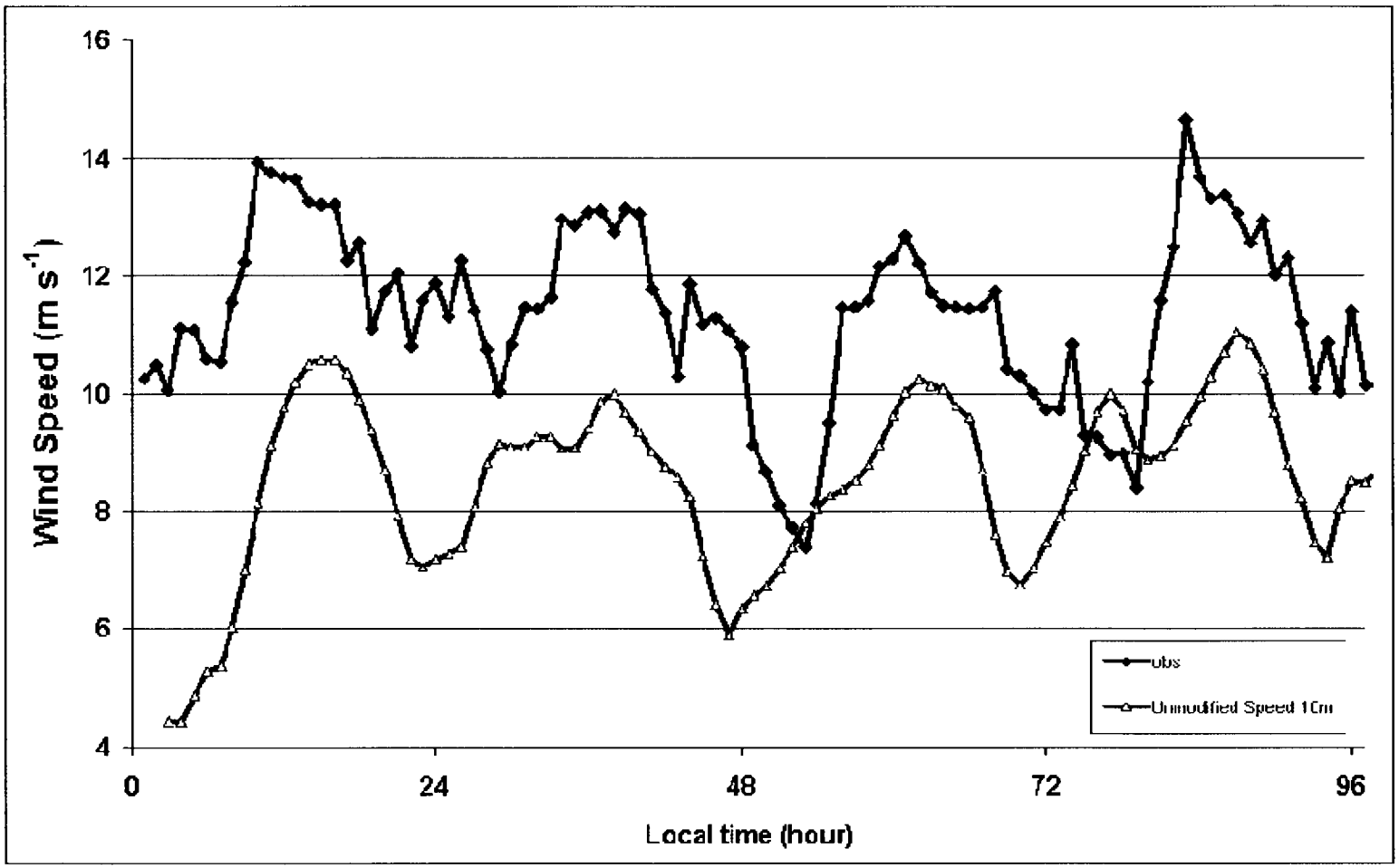


**Fig. 67.** Model (-♦-) vs. observed (-▲-) of 10 m wind speed (m $s^{-1}$) comparison at the station of Gahro (with out roughness adjustment).

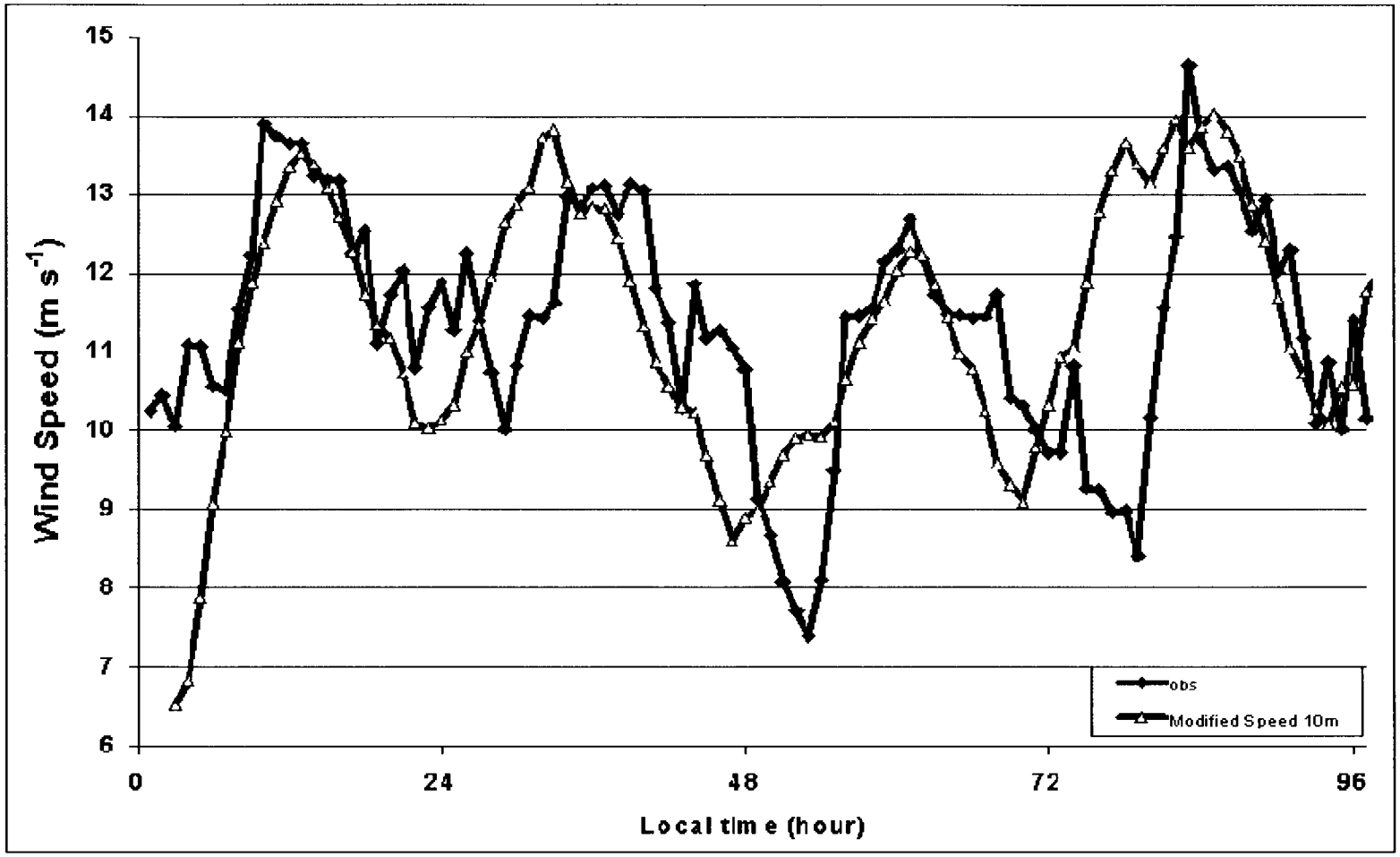


**Fig. 68.** Model (-♦-) vs. observed (-▲-) of 10 m wind speed (m $s^{-1}$) comparison at the station of Gahro (with roughness adjustment)

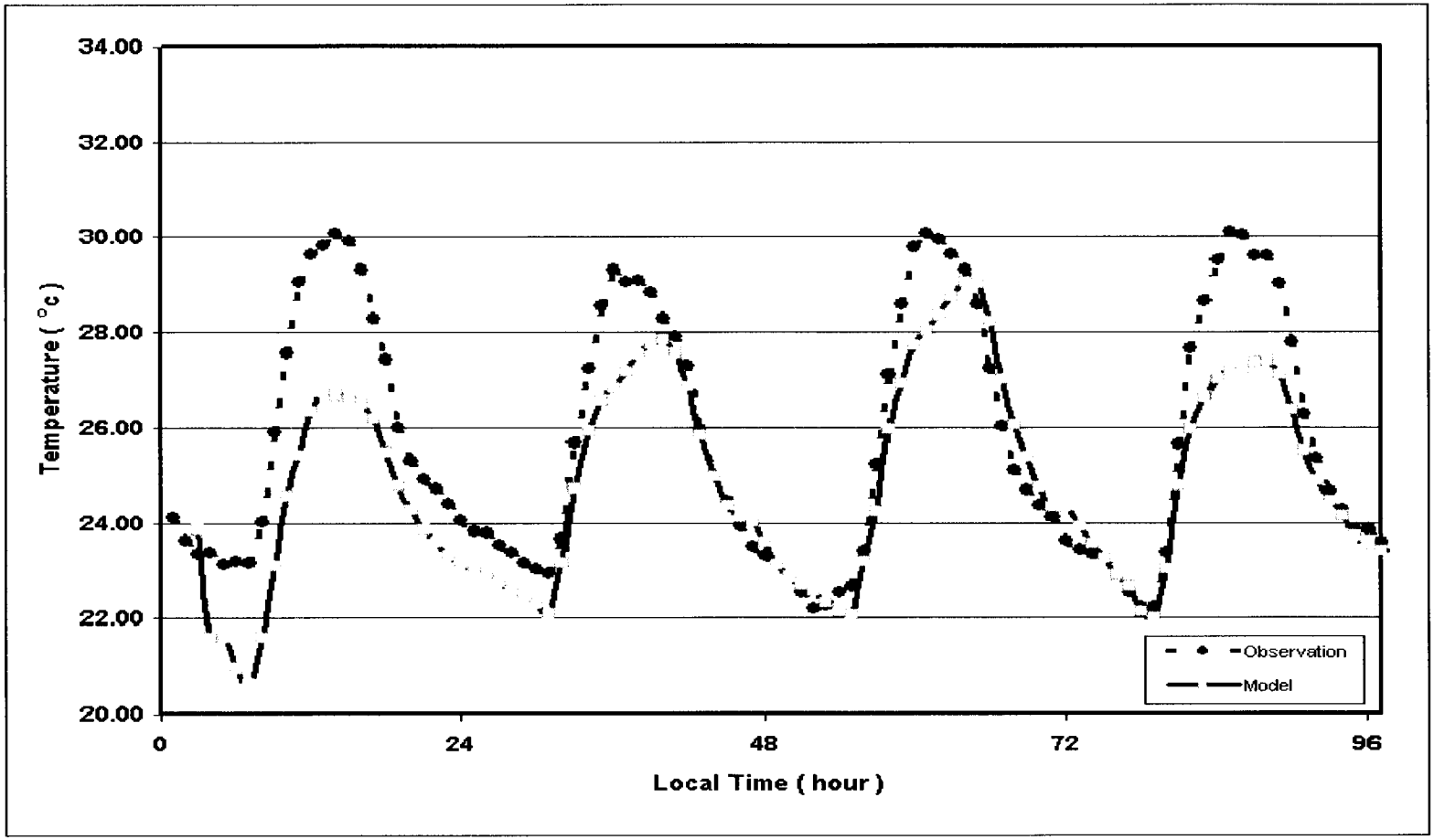


**Fig. 69.** Model (-●-) vs. observed (-■-) of surface temperature (°C) comparison at the station of Aseb (with out roughness adjustment)

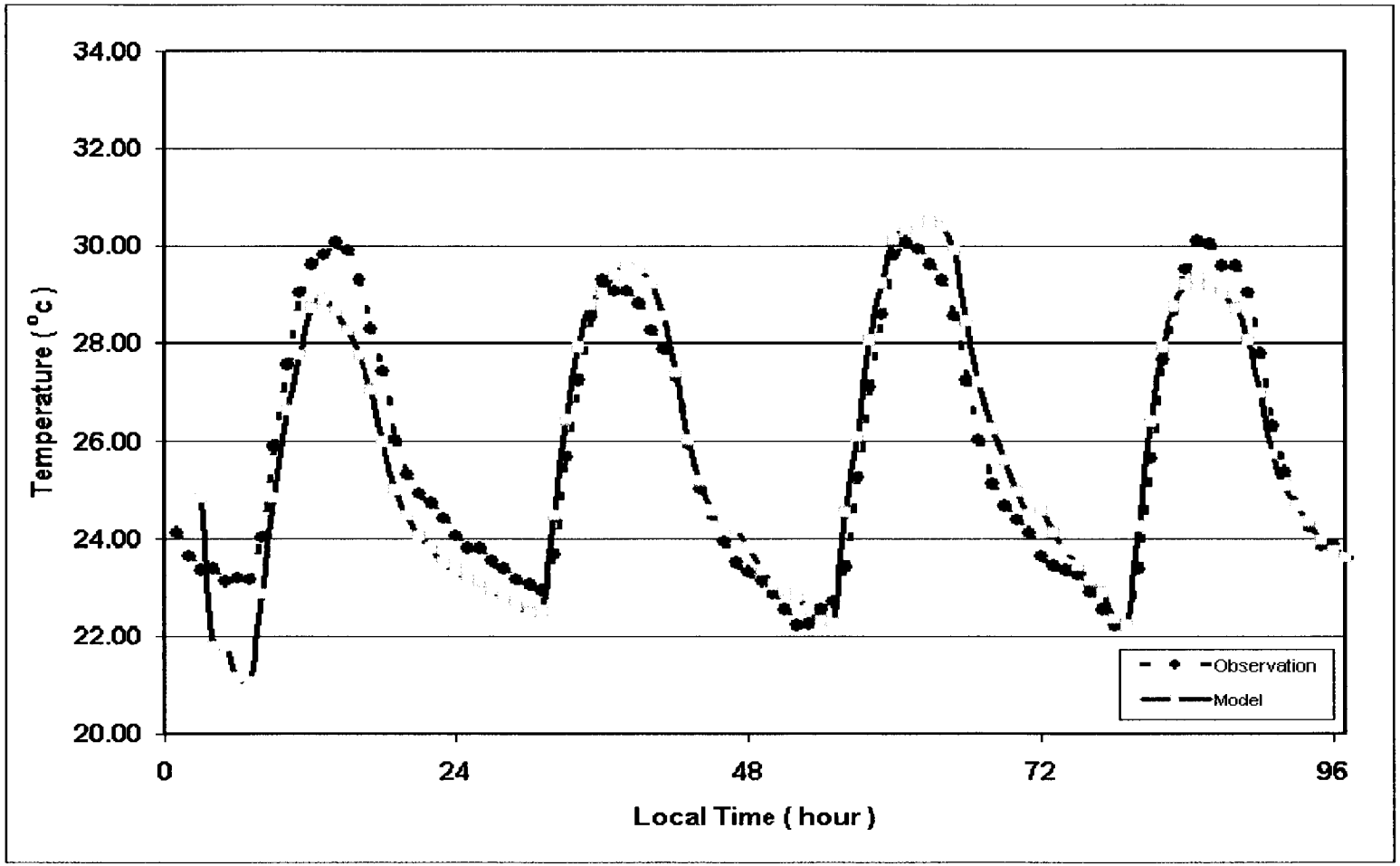


**Fig. 70.** Model (-●-) vs. observed (-■-) of surface temperature (°C) comparison at the station of Aseb (with roughness adjustment).

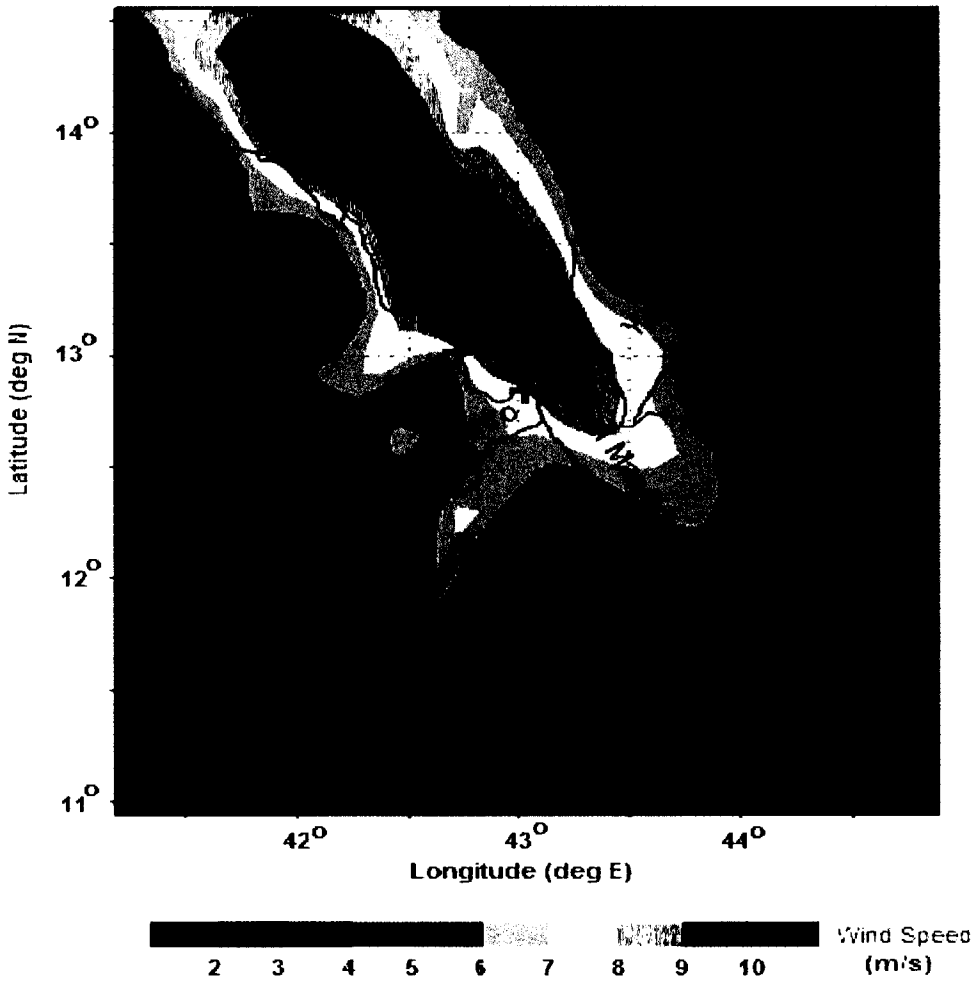


**Fig. 71.** Grid-2 10 m average wind speed (m $s^{-1}$) (average of the simulation period).

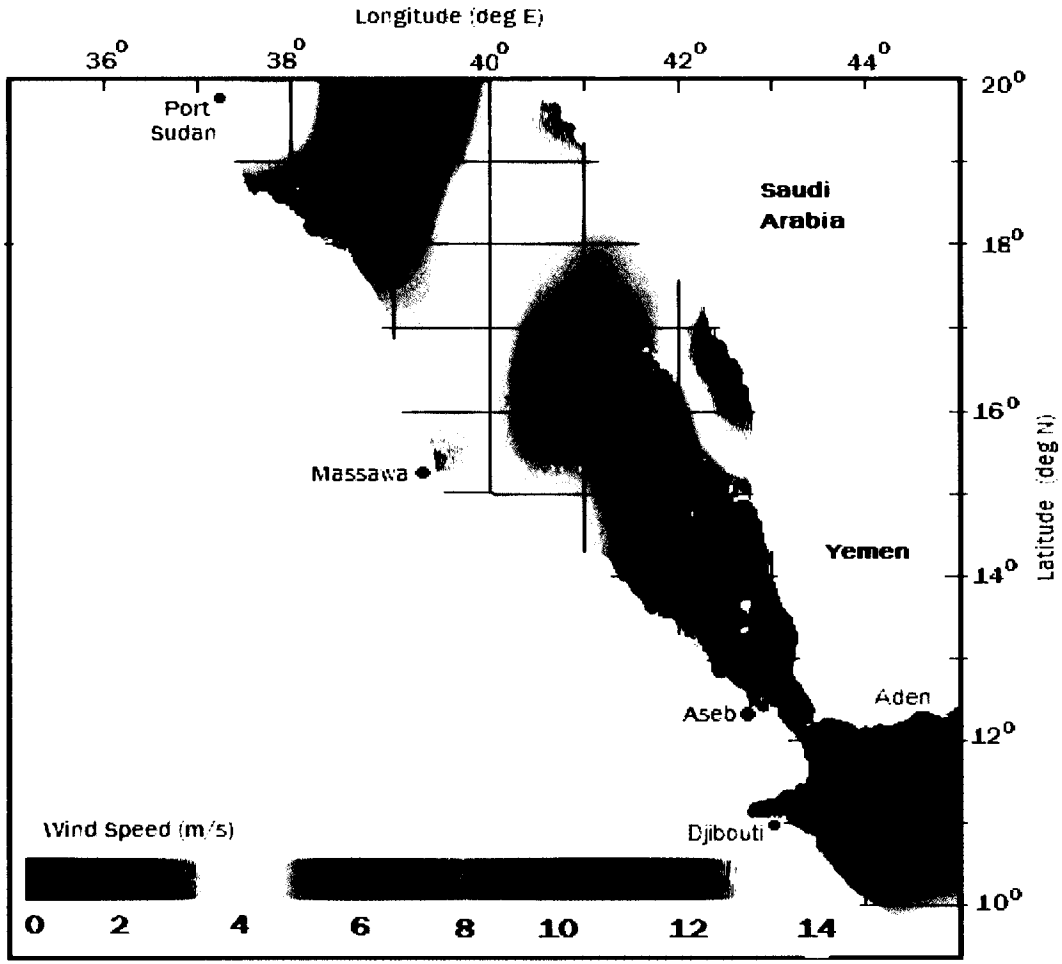


**Fig. 72.** Scaterometry-derived wind speed (m $s^{-1}$) map of the Red sea (for the month of February)

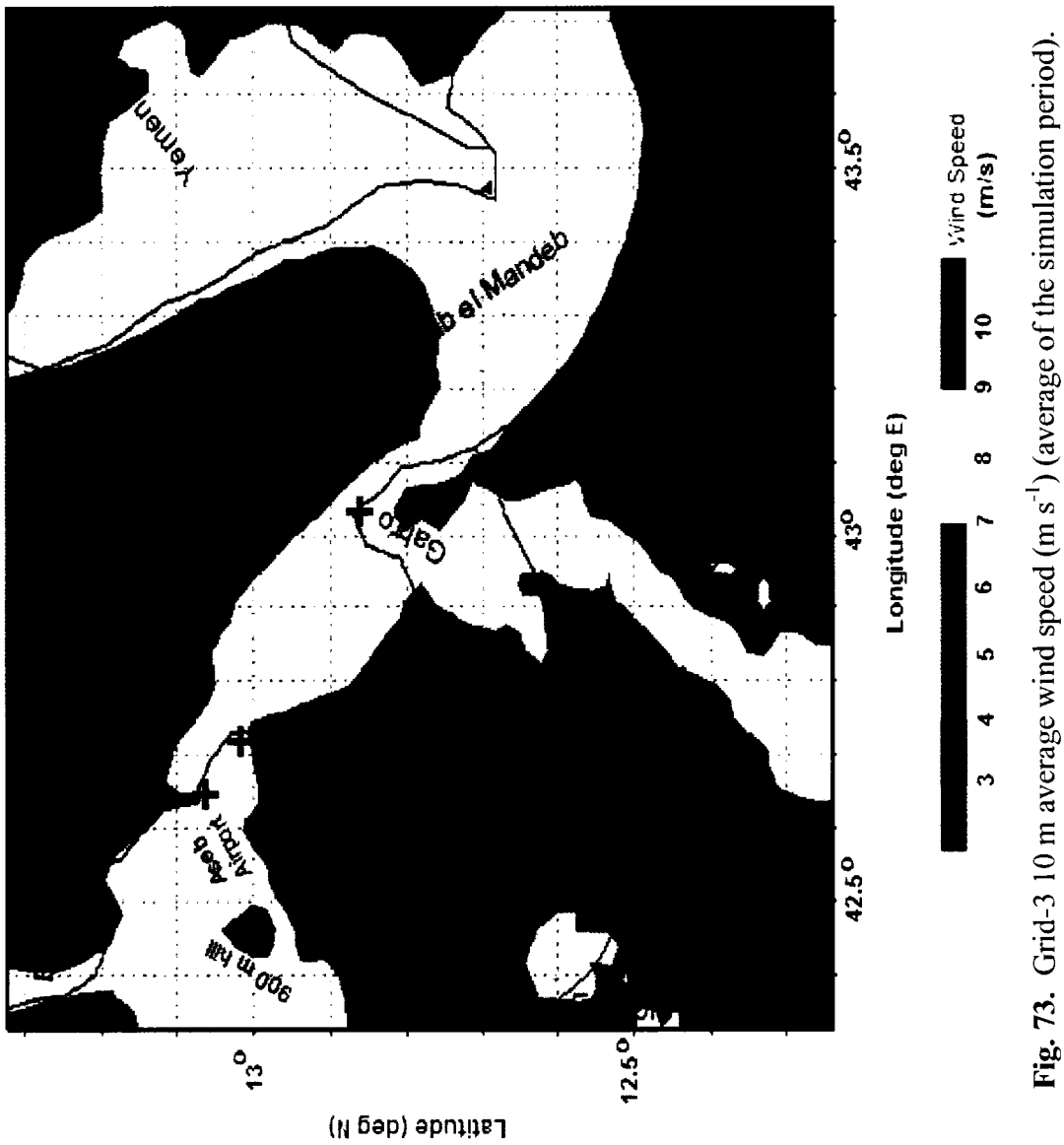


**Fig. 73.** Grid-3 10 m average wind speed (m $s^{-1}$) (average of the simulation period).

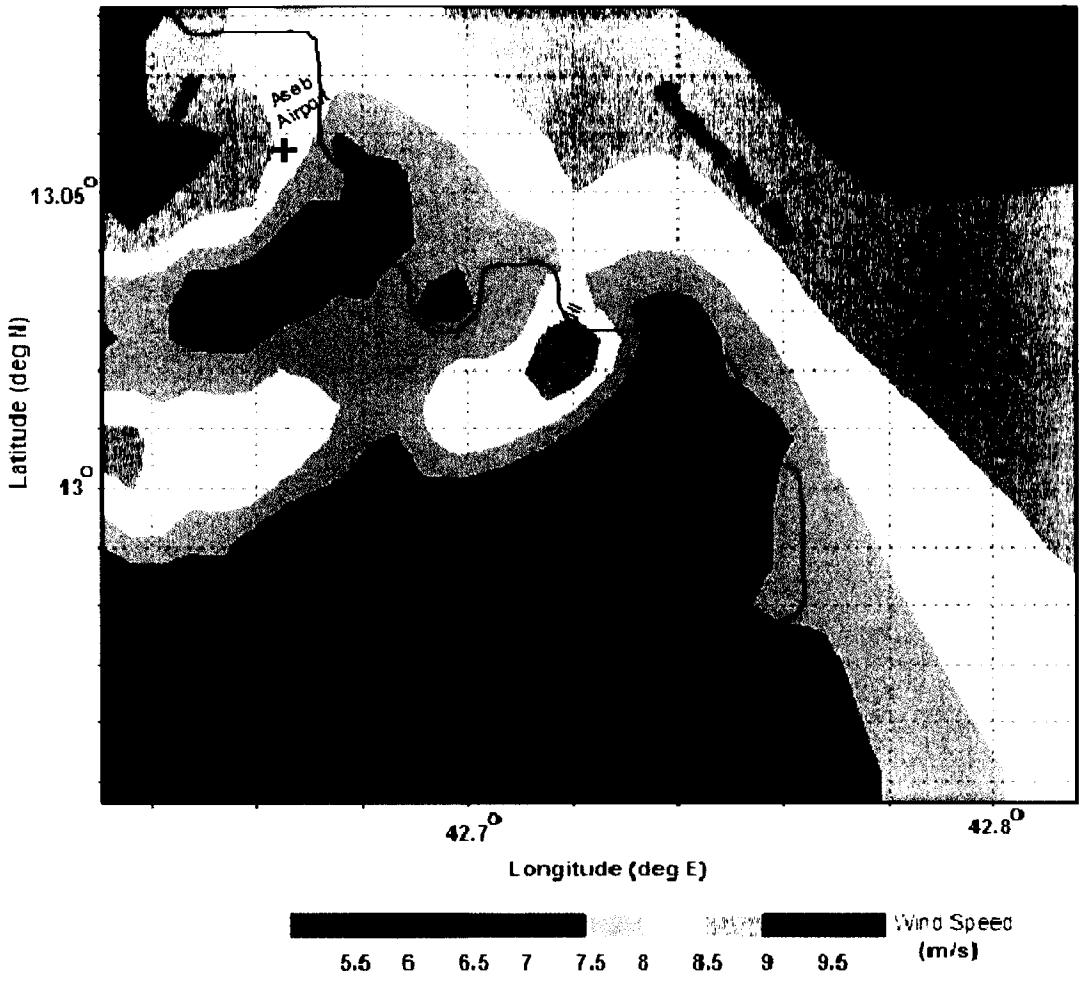


**Fig. 74.** Grid-4 10 m average wind speed (m $s^{-1}$) (average of the simulation period).

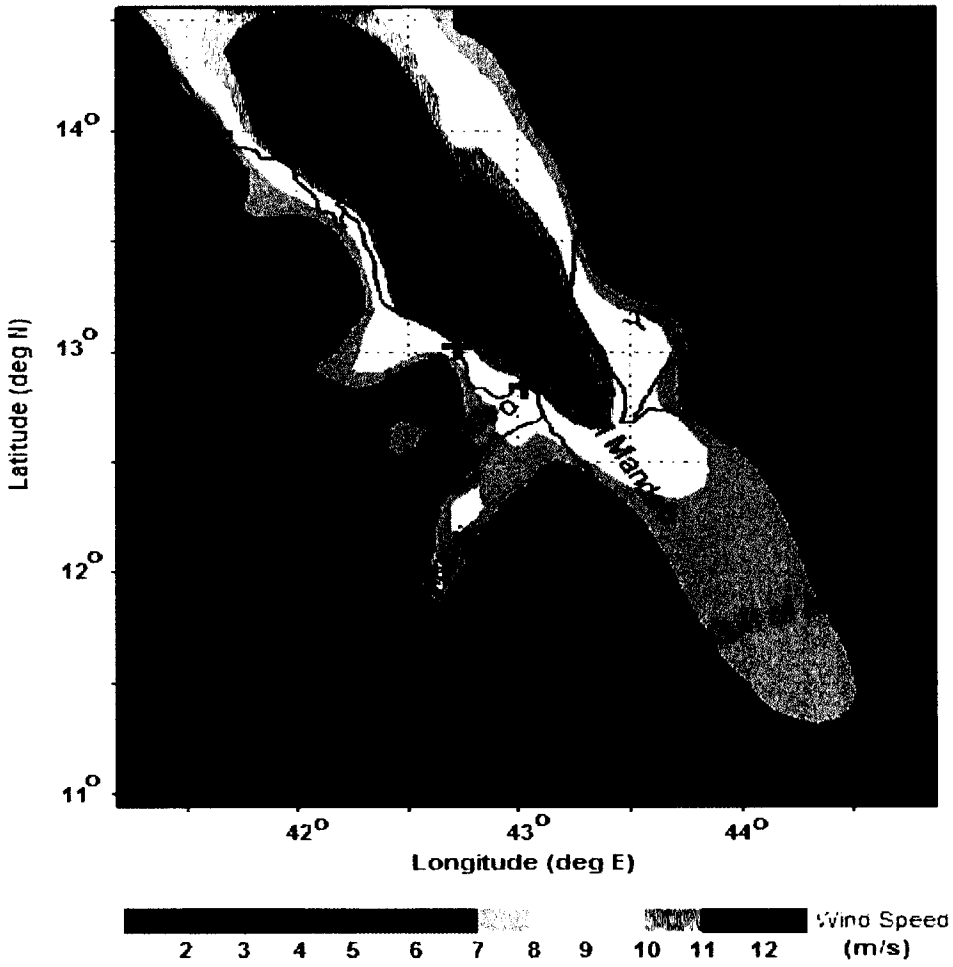


**Fig. 75.** Grid-2 20 m average wind speed (m $s^{-1}$) (average of the simulation period).

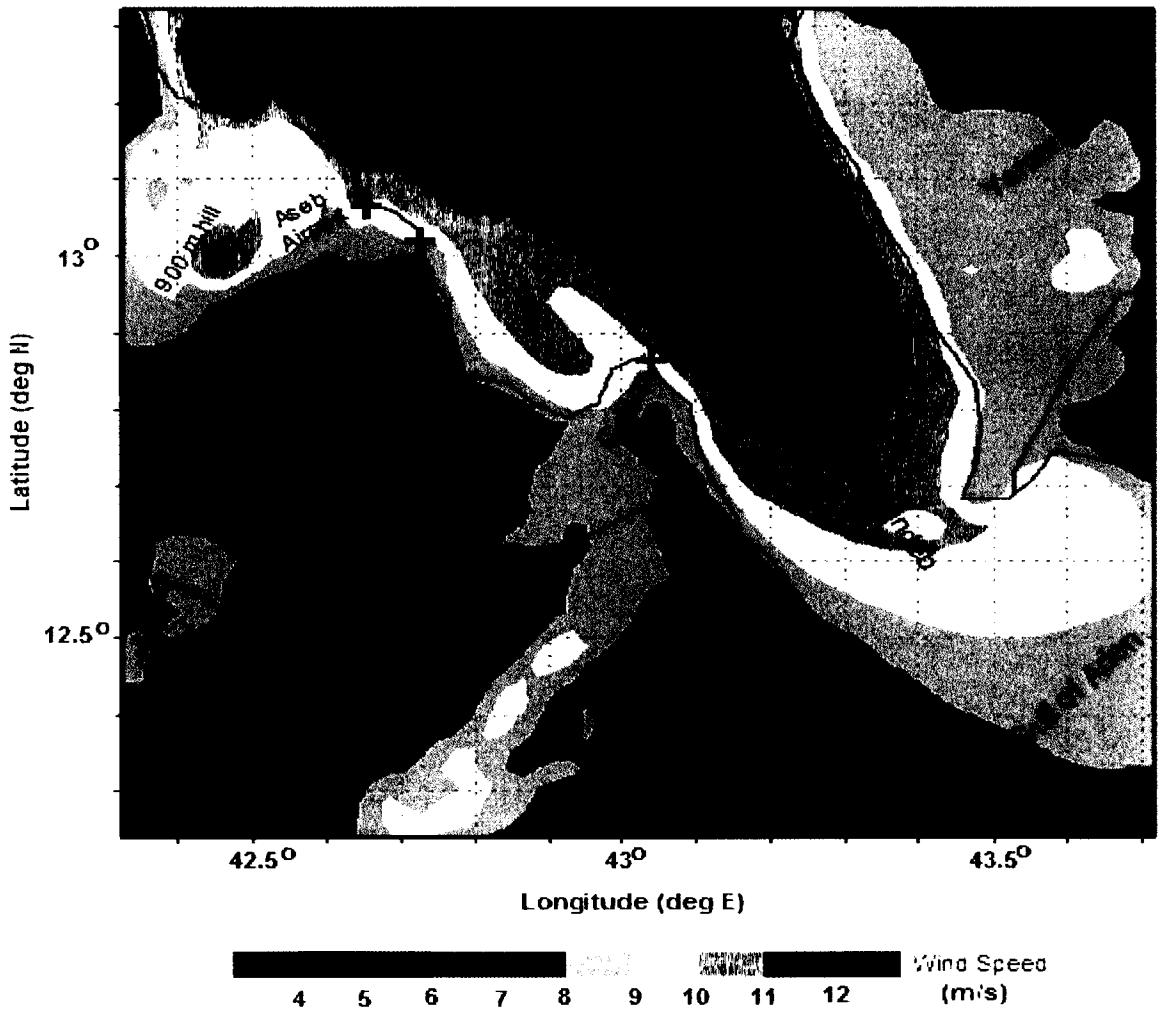


**Fig. 76.** Grid-3 20 m average wind speed (m $s^{-1}$) (average of the simulation period).

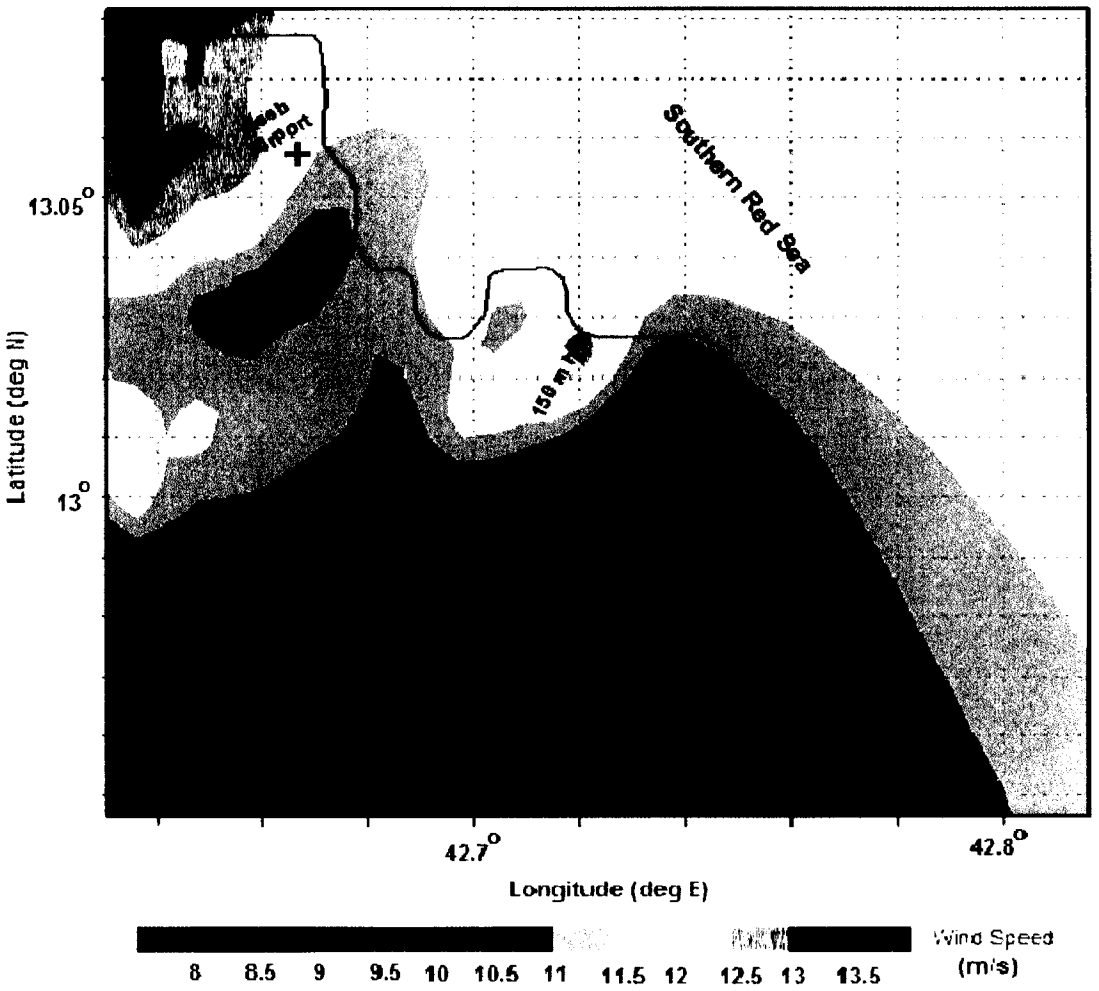


**Fig. 77.** Grid-4 20 m average wind speed (m $s^{-1}$) (average of the simulation period).

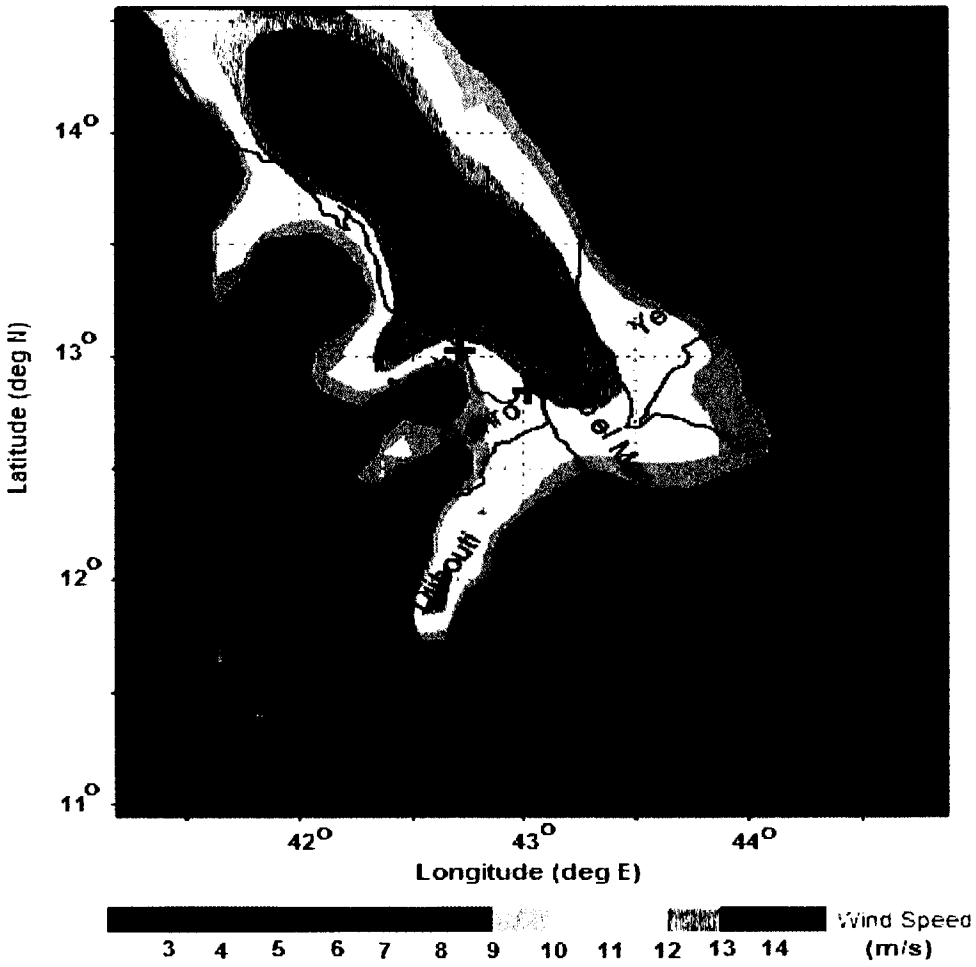


**Fig. 78.** Grid-2 60 m average wind speed (m $s^{-1}$) (average of the simulation period).

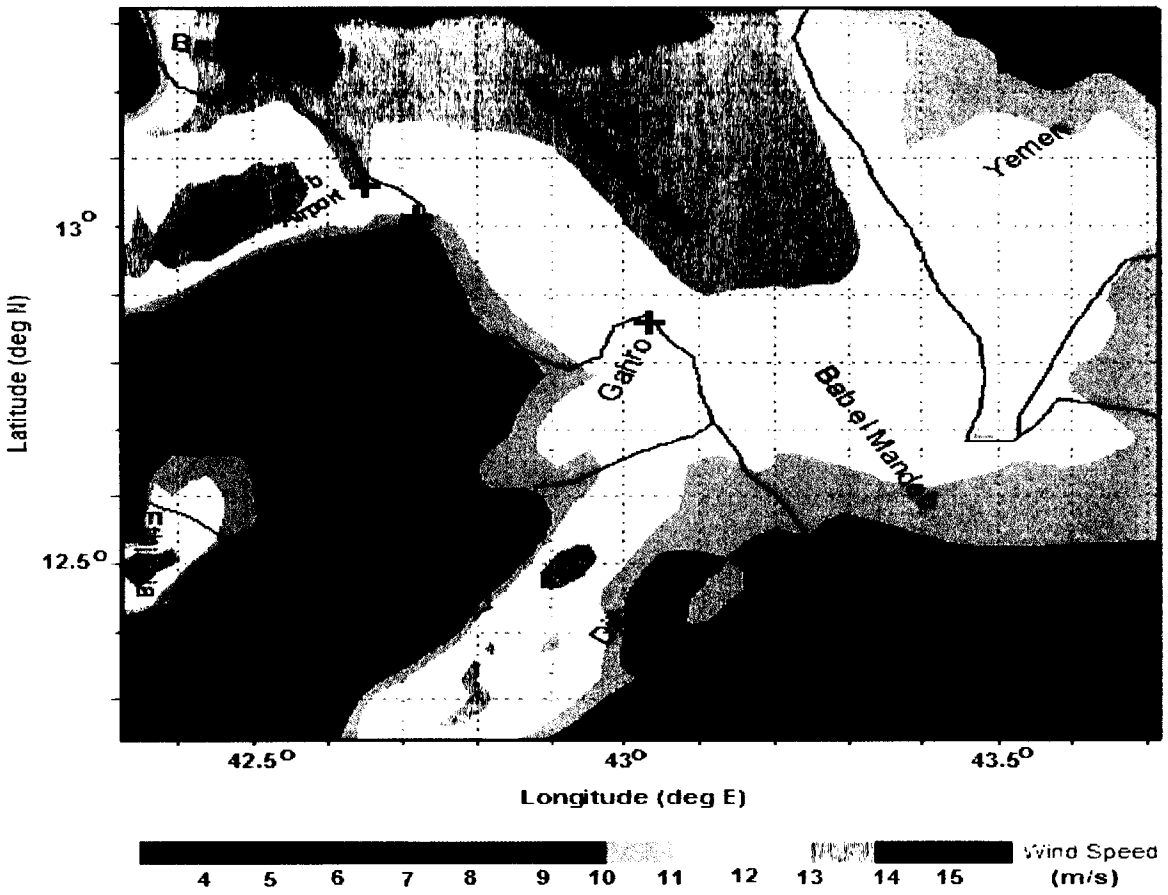


**Fig. 79.** Grid-3 60 m average wind speed (m $s^{-1}$) (average of the simulation period).

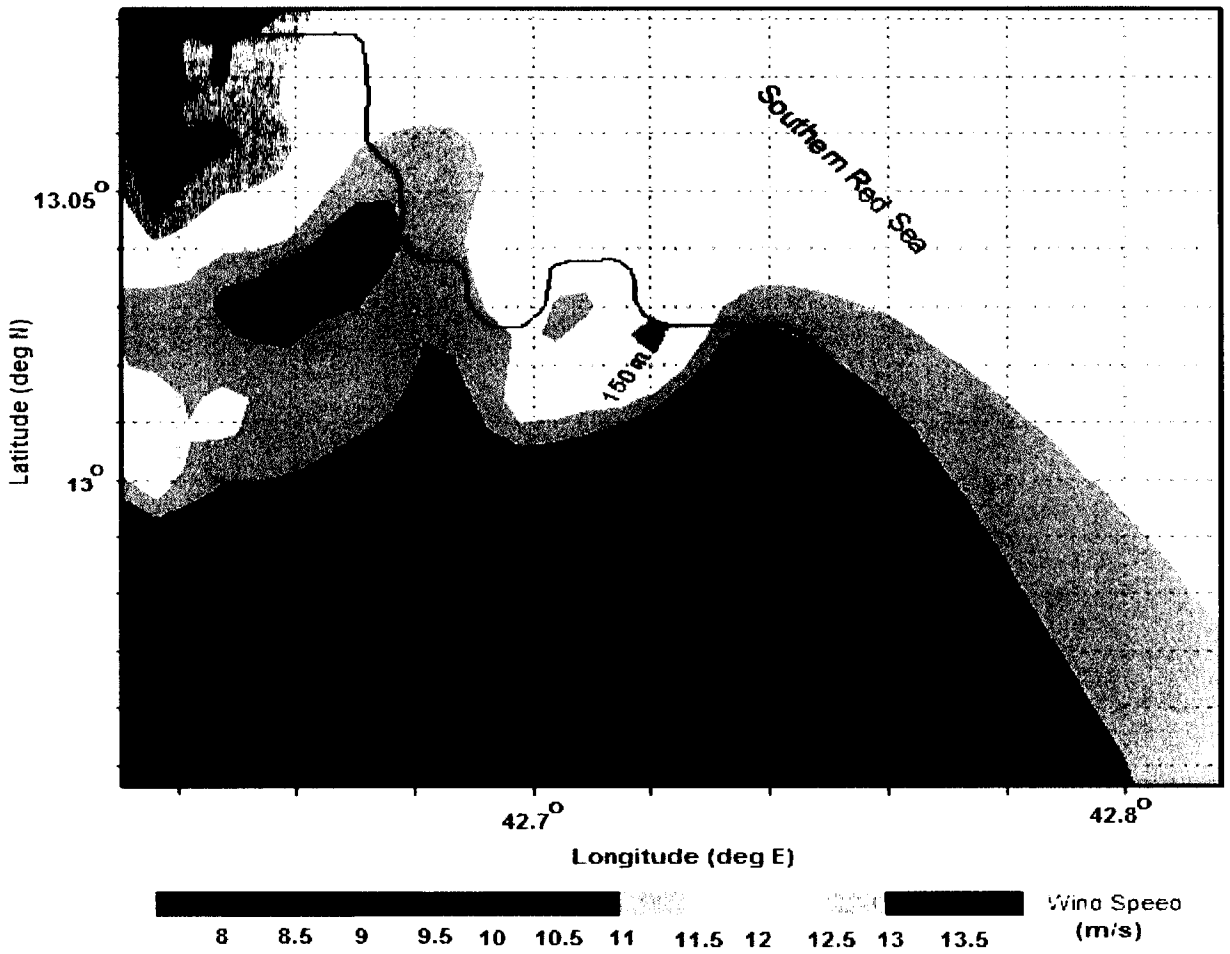


**Fig. 80.** Grid-4 60 m average wind speed (m $s^{-1}$) (average of the simulation period).

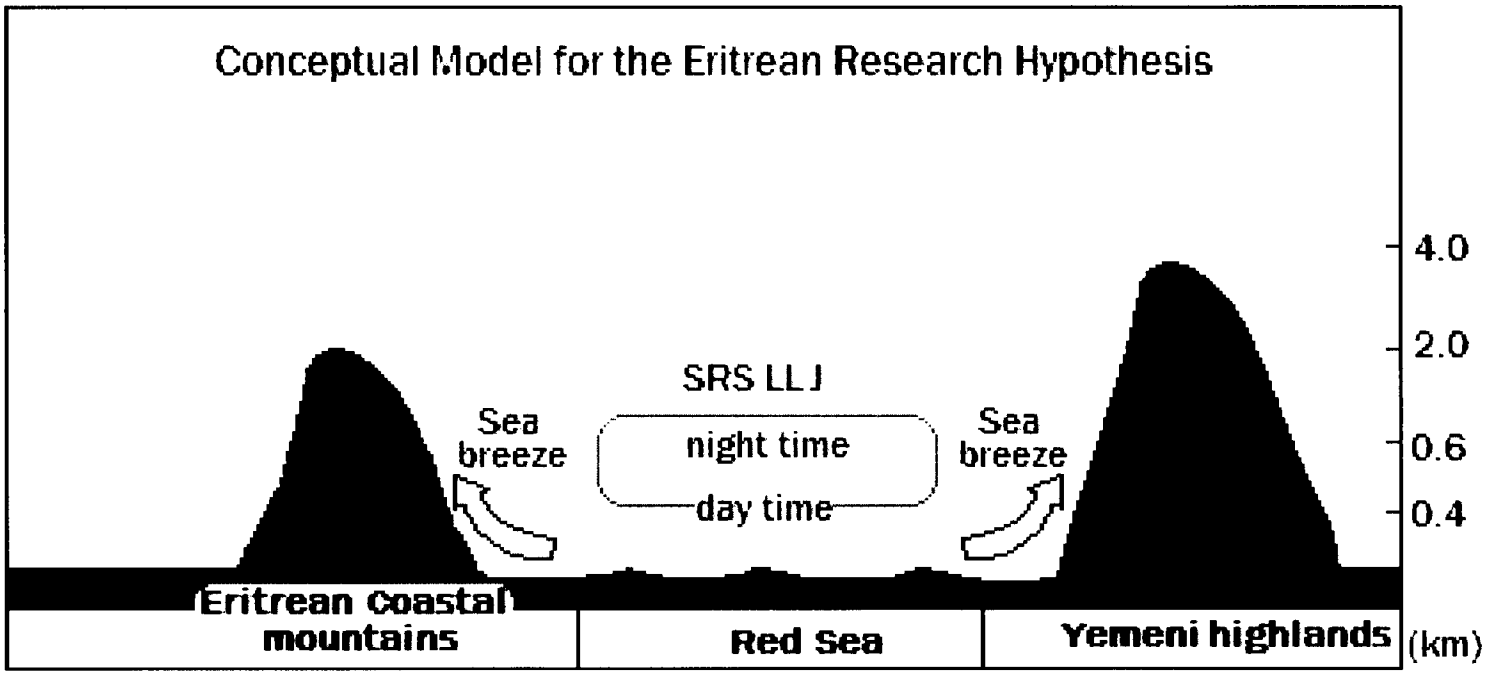


**Fig. 81.** Conceptual model for Eritrean Southern Red Sea research hypothesis.

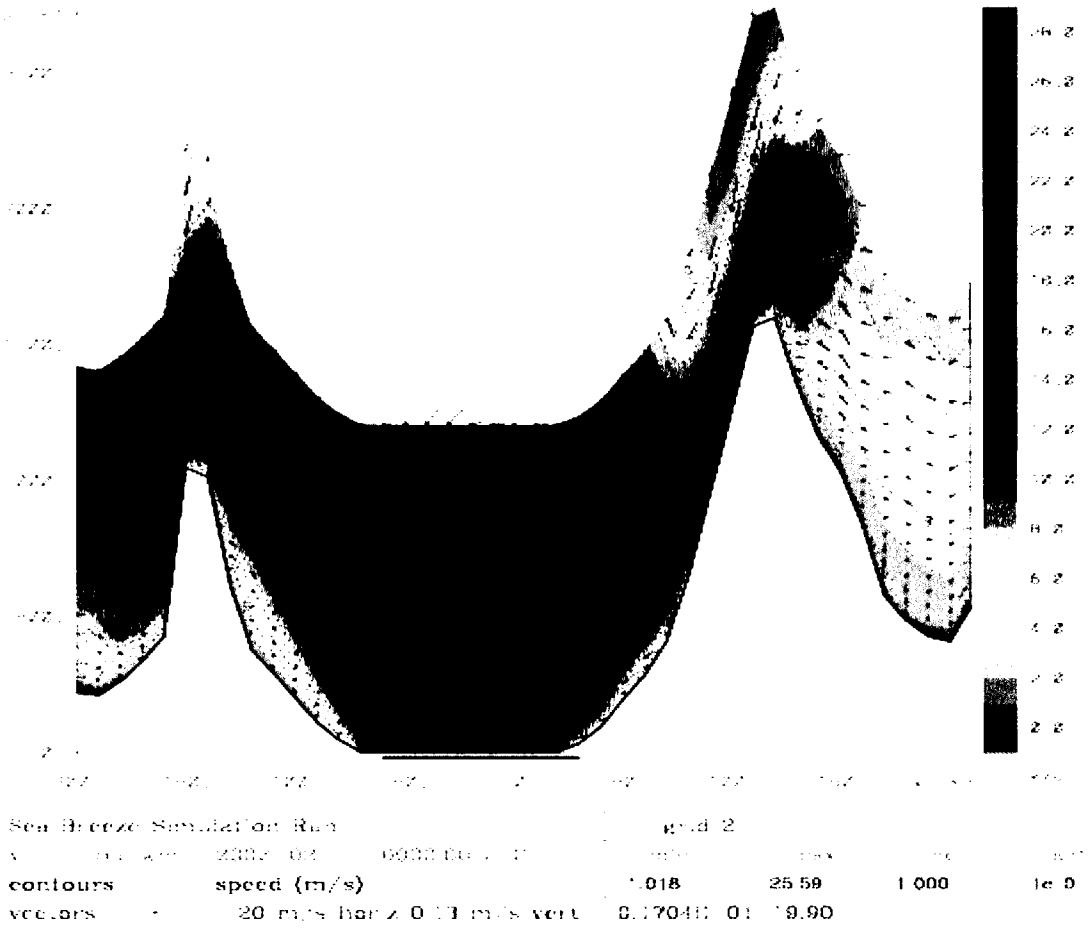


**Fig. 82.** Vertical cross section of the Red sea LLJ (0000 UTC February 11 2002).

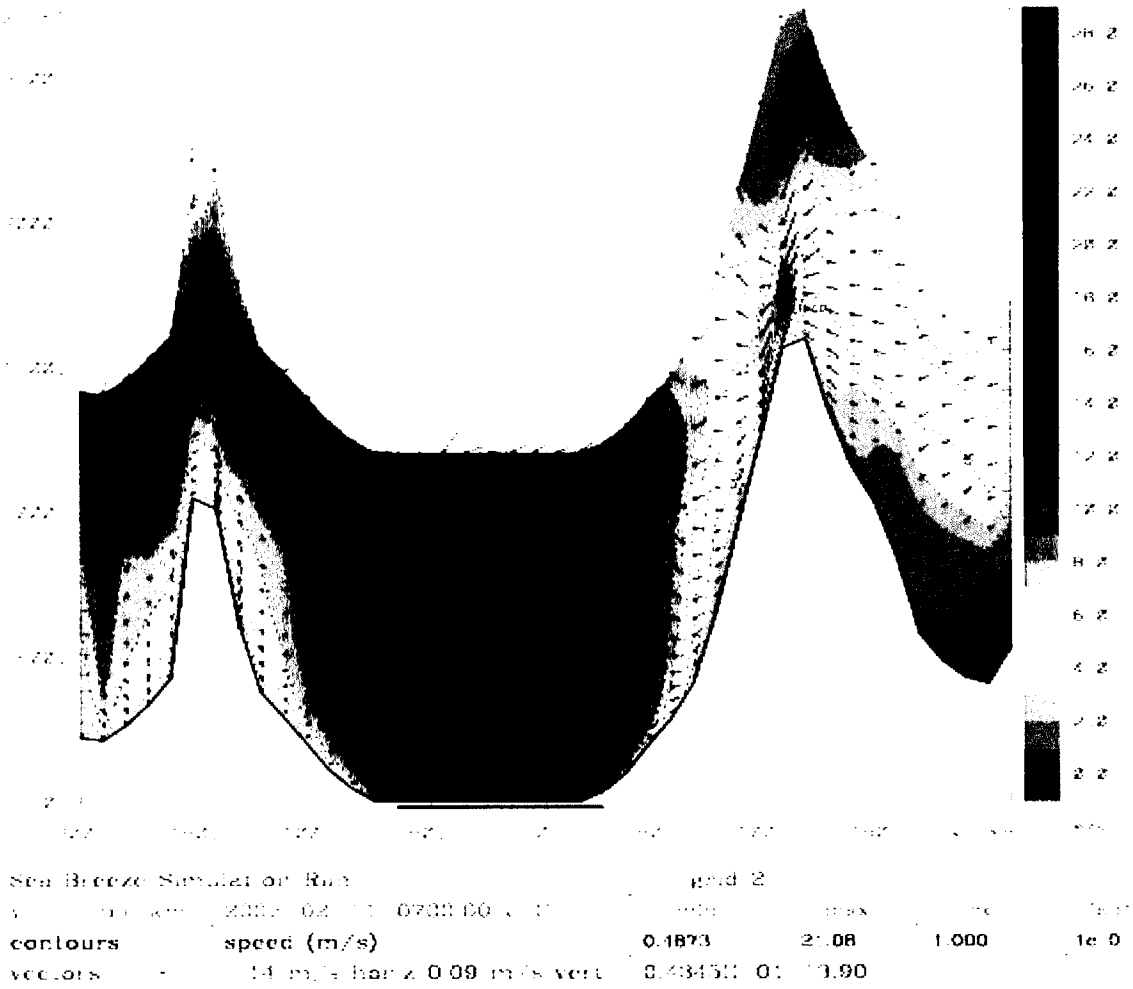


**Fig. 83.** Vertical cross section of the Red sea LLJ (0700 UTC February 11 2002).